Stellingen bij het proefschrift
"Concrete under impact tensile loading and lateral compression"
van
Jaap Weerheijm

1. Ten onrechte is aan beton een toename van de breukenergie toegekend bij een toename van de belastingsnelheid. Het onstaan van meervoudige breukvlakken is een vorm van constructierespons en dient niet als eigenschap aan het materiaal te worden toegekend.

2. De geprononceerde toename in sterkte, zoals voor diverse materialen bij hoge belastingsnelheden wordt waargenomen, moet toegeschreven worden aan het domineren van traagheidseffecten in de mechanische respons van het materiaal rond scheurtips en niet aan een verandering in bezwijkmechanisme.

3. De invloed van de belastingsnelheid op de treksterkte van beton neemt af naarmate de statische drukbelasting in laterale richting toeneemt.

4. De eenduidige belastingafdracht in de Split Hopkinson Bar-opstelling maakt deze bij uitstek geschikt voor het onderzoeken van dynamische materiaal-eigenschappen.

5. Herverdeling van spanningen spelen een belangrijke rol bij de respons van ongewapend betonnen proefstukken. Het niet-lineaire gedrag van beton voordat de maximale treksterkte wordt bereikt, dient daarom gemodelleerd te worden om een korrekte simulatie mogelijk te maken.

6. De dynamische materiaaleigenschappen van beton kunnen niet eenduidig worden vastgelegd in een numeriek materiaalmodel. Traagheidseffecten leiden tot mesh-afhankelijkheid.

7. De heterogene opbouw van beton waarborgt het mechanisme van "crack arrest" en draagt daarmee in belangrijke mate bij tot de sterkte van het materiaal.
   Het streven naar een homogene bevolkingsamenstelling leidt tot eenzijdigheid en verzwakt een samenleving.

8. De "consequence analysis" als toegepast in risicostudies voor de (petro) chemische industrie, moet worden betiteld als inconsequent omdat de uitwerking op de omgeving daar geen evenwichtig onderdeel van uitmaakt.

9. Om tot een goede quantificering van risico's te kunnen komen, dienen de ongevallen in de industrie onderzocht te worden door een onafhankelijk team van experts.

10. In onze egocentrisch gerichte maatschappij zijn wij eerder onverschillig dan tolerant.

11. De consumptiemaatschappij is het georganiseerde resultaat van onze hebzucht. De daarin geldende normen dienen dan ook kritisch beschouwd te worden.

12. Net als bij de dynamische respons van constructies worden de spanningen in een bedrijf tengevolge van een reorganisatie bepaald door de hogere eigenfrequenties, gevormd door de individuele werknemers. Discontinuïteiten naar tijd of plaats verhogen het spanningsniveau in hoge mate.

13. Het opkomen voor de dienstplicht is, ook bij het gewijzigd Defensiebeleid, een verdedigbare stellingname.

CONCRETE UNDER IMPACT TENSILE LOADING

AND LATERAL COMPRESSION

CONCRETE UNDER IMPACT TENSILE LOADING

AND LATERAL COMPRESSION

PROEFSCHRIFT

ter verkrijging van de graad van doctor
aan de Technische Universiteit Delft,
op gezag van de Rector Magnificus, prof. drs. P.A. Schenck,
in het openbaar te verdedigen ten overstaan van
een commissie aangewezen door
het College van Dekanen
op 3 november 1992
te 14.00 uur
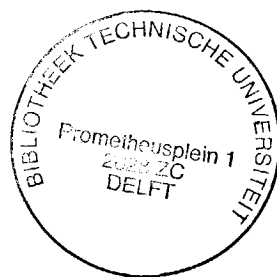
door

Jakob Weerheijm

geboren te Vlaardingen
civiel ingenieur

Dit proefschrift is goedgekeurd door de promotor

Prof.Dr.-Ing. H.W. Reinhardt

ACKNOWLEDGEMENT

TNO-Defensieonderzoek

PRINS MAURITS LABORATORIUM TNO

Prins Maurits LaboratoriumTNO
Lange Kleiweg 137
Postbus 45
2280 AA Rijswijk

telefoon : 015-842842
fax   : 015-843991

CONTENTS

1   INTRODUCTION

Concrete is commonly used in protective structures that are specially designed to resist impact and explosive loading. Under these extreme loadings, the response of structure and material differ considerably from static conditions. Because of this difference, extrapolation from static response and material strength might lead to unsafe designs.
In the structural response and ultimate resistance, the portion of the dynamic material behaviour appears to be of great importance. Consequently, knowledge on the rate effects and an adequate modelling of concrete behaviour is required for the design of protective structures and to quantify the protection level.

The loading conditions mentioned are common for military protective structures, and most empirical design rules originate from this field. However, potential hazards and risks in our community also demand that structures and structural elements be specially designed to resist occasional dynamic loading. Examples of potential hazards are: the transport of dangerous goods through tunnels, ships and/or vehicles colliding with bridge and viaduct pillars, LNG storage facilities, aircraft colliding with a nuclear reactor, and off-shore structures might be subjected to impact and explosion.
Although impact or explosion is a rare occurrence for civilian structures, it is critical for the design of structures because they both lead to extreme loading conditions and the acquisition of knowledge is necessary for economical design and reliable assessment of safety.

The need for special knowledge has been recognized, and over the last two decades, various research programmes were dedicated to the dynamic response of structures and concrete. The developments in the field of computer facilities and numerical codes exceeded the knowledge growth on material behaviour. This led to the current situation that force and stress distributions can be calculated in complex structures under complex dynamic loadings, but have to be combined with static material models. To utilize the possibilities of the advanced computer codes for dynamically loaded concrete structures, research on the dynamic material response and reliable models is necessary and demands more attention.

Hitherto, the material research was mainly focused on the dynamic, uniaxial strength and the rate effect has been quantified, while the fracture energy is mostly coupled to the dynamic strength. The significant rate effect on concrete strength for uniaxial load conditions is in accordance with the observed resistance of concrete structures to impact and explosive loading. Under these type of loading, high amplitude stress waves propagate through the structure and the material is exposed to multiaxial load conditions. When a linear elastic response is assumed, stress levels are calculated that exceed the static strength many times but, these stresses are also coupled to high loading rates. Apparently, the material resists the high stresses also under high rate multiaxial loading and the resistance of the structure increases. Because of the rate sensitivity of concrete, this feature has to be incorporated in dynamic material models

and integrated in numerical codes. However, for multiaxial loading conditions, the rate dependency is quantitatively unknown. The field of the material response under multiaxial, dynamic loading conditions has scarcely been entered experimentally or theoretically. To gain more insight into the influence of multiaxial load conditions on the dynamic response of concrete, a theoretical and experimental study was initiated for a combined static compression and dynamic tensile loading.

In the programme, the scope of biaxial dynamic loading conditions has been narrowed down to the combination of static lateral compression and axial impact tensile loading. This loading condition was chosen because, related to uniaxial loading, the complexity is increased by just one step, and individually, the response under both conditions is understood quite well. Under the combined load, the influence of internal stress distribution and damage on the dynamic response can be studied.
The study was mainly focused on strength, the failure envelope. The objective was to study the influence of lateral compression on the rate dependency of the residual impact strength. In the theoretical part, all loading rates were considered, with uniaxial impact loading as the reference. The experiments were dedicated to answer the question whether the shape of the failure envelope is affected by rate effects.

In addition to the strength, the deformation capacity and fracture energy are very important parameters for characterizing and describing the dynamic response. Because the response under uniaxial tensile load functioned as reference, uniaxial impact tests were necessary and could be used to examine the deformation capacity and fracture energy for a single failure zone.

To understand and be able to model the dynamic response of concrete, the extension of damage in the heterogeneous concrete material has to be considered. The influences of inertia effects on the damage extension form the key to the rate effects on concrete response. In Chapter 2 a review is given on the failure processes observed at macro-level under uniaxial and biaxial loading and related to the damage extension inside the material. The known rate effects on the uniaxial response and the scarce research on multiaxial loading are summarized. Various approaches to model concrete response are given in the literature and summarized in this chapter.
To model the dynamic response of concrete, and to be able to incorporate inertia effects into a model, strong simplifications, assumptions and a schematized presentation of the fracture process is necessary. This approach was followed in the model given in Chapter 3. The model describes the rate dependency of uniaxial tensile strength. The potential fracture plane in concrete was schematized to a fictitious fracture plane with equally distributed penny-shaped cracks. The extension of these cracks was described by using Linear Elastic Fracture Mechanics, resulting in a time dependent description of the fracture process. The model gives a good description of rate effect for all loading rates and also reflects the rate sensitivity for different concrete qualities. The next step was to examine the effect of changing initial conditions due to lateral compression. Chapter 4 describes the approach followed to predict the rate effect on the residual impact strength as a function of the lateral compression level. The

internal damage and stresses due to compression were translated to initial conditions for the fictitious fracture plane for tension or compression. Subsequently, the crack extension under impact tensile loading was described resulting in a prediction for the residual strength.

The following three chapters describe the experimental part of the study. The experiments were performed in a Split Hopkinson Bar apparatus which was combined with an hydraulic prestressing device. Chapter 5 describes the experimental set-up and the results of the evaluation programme. The interaction between the static and dynamic loading device was decisive for the applicability of the test set-up.

Chapter 6 presents the results of the uniaxial impact tests. The geometry of the specimen was prismatic and notches were applied to fix the location of the failure plane and ensure the occurrence of a single failure zone. Because of the uncommon geometry special attention was paid to the influence of the applied notches and to the structural response on the test results. The biaxial tests are the subject of Chapter 7. The analysis appeared to be complicated because of the interaction between both devices. Nevertheless the failure envelope at the applied loading rate of about 15 [GPa/s] could be determined. Finally, the results of the experiments and modelling are compared.

Chapter 8 concludes this thesis with a summary of the research programme and the conclusions.

2   LITERATURE SURVEY

This chapter gives a survey of concrete response features, failure mechanisms, rate effects and modelling approaches. The literature citations and the discussion given form the background for the modelling and the interpretation of the test results presented in this report.

2.1   Introduction

Research on concrete response under various types of loading has shown that the material behaviour reflects the heterogeneous composition. The heterogeneity leads to irregular internal stress distributions and initial local damage.
The failure process of concrete is based on the extension of the internal damage. The relation between load and deformation at the macro-level is determined by the relation between the load and internal crack or damage extension, see for instance the review of Mindess [65].
From this general statement it emerges that the base for understanding dynamic response and properties of concrete is the knowledge of crack extension under dynamic loading. The dynamic effects on the internal failure process have to be known and incorporated in dynamic material models. Including rate effects in the description of damage extension and modelling significantly increases the complexity and number of uncertainties.
In the current programme, it was decided to focus on the dominant features of the response based on the internal failure mechanism.
The research focused on the uniaxial dynamic tensile load combined with static lateral compression. These loading conditions are discussed in this chapter.

2.2   Failure process under uniaxial tension

The description of the damage extension at various scale levels is given in literature. In the current study the meso-level as defined by Wittmann [111] is used because it offers the opportunity to include heterogeneity in the damage extension as bond, matrix and aggregate fracture. Main features of concrete failure can be explained considering this scale level.

Considering the meso-level, the shape of the static load-deformation curve, see Figure 2.1, is coupled to the generalized failure process as follows.
The initial damage and stresses at 60% of the uniaxial strength, f_t, lead to crack growth and initiation of new micro-cracks at the bond faces, reflected as the onset of non-linearity in the response curve. Due to the heterogeneity of concrete the cracks are arrested and crack growth is stable.

Beyond the 0.8 f_t level, micro-cracks in the matrix start to grow, bridging the bond cracks, and macro-cracks are formed. The fracture process becomes unstable and the maximum load is reached. An equilibrium between the energy associated with the applied load and the dissipated energy in the fracture process is only possible by decreasing the load, leading to the softening branch of the curve.

In experiments, the softening branch can only be determined in a very stiff machine. The softening branch reflects the unstable equilibrium between the supplied and the absorbed energy [63, 20, 34]. Consequently, during testing one must be sure that the energy is absorbed in the considered fracture zone.

86009-2.1
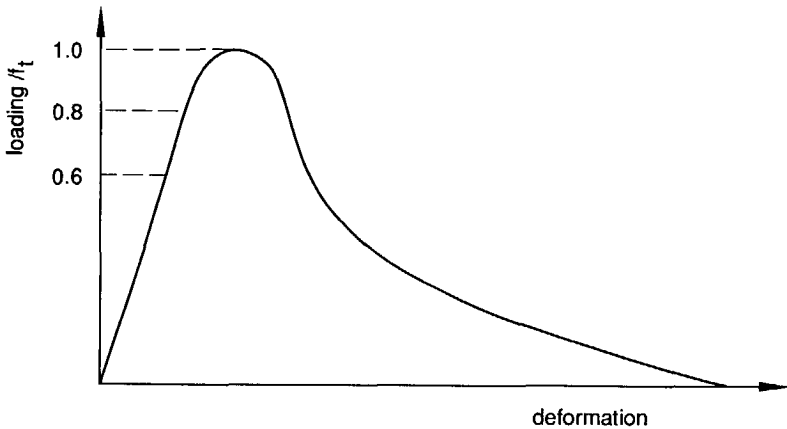
Figure 2.1 The load-deformation curve under uniaxial tensile loading.

The pre-peak fracture process is characterized by a moderate deviation from the initially linear response and a stable crack growth.

The unstable post-peak failure is not fixed to a single fracture plane. There is a process zone of micro-cracking ahead of the tip of the macro-crack [65, 33]. During the extension of the macro-cracks, the energy barriers delay the total rupture of the material. Consequently the heterogeneity affects the shape of the softening zone considerably. The mechanisms of crack arrest are given in [85, 124, 20].

Related to the post-peak fracturing process the energy absorption in the pre-peak process is small and mostly neglected for tensile loading. However, the strength is determined and governed by the pre-peak micro-fracture process. Therefore, rate effects on the strength must be caused by changes in pre-peak fracturing. This fact is used in modelling the rate effects on tensile strength, see Chapter 3.

2.3   Failure process under uniaxial compression

In the present study little attention is paid to the response under compression. Some general features are used in the modelling, and will be mentioned in this section.

Similar to the load-deformation curve under tension, the response curve under static compression is closely related to the mechanism of internal progressive micro-cracking. The limit of elasticity, i.e. the onset of micro-cracking, is given as 30% of the compressive strength, f_c. Between 0.3 and 0.5 f_c, the bond cracks start to extend in a stable way. Up to 80% of f_c, the bond cracks extend and some bridging occurs through the matrix for nearby aggregates. Beyond 0.8 f_c, the micro-cracking in the matrix becomes significant and the fracture process becomes unstable.

Under compression, tensile stresses and strains are induced in the material between the stiff aggregates, while cones with a three-dimensional compressive stress state are formed on the aggregates in the direction of the compressive loading. These stresses lead to fracture in planes oriented about 30° from the load direction. Final failure occurs due to sliding along some of these planes.

Stroeven [98] and more recently, Van Mier [63], described the fracture process in detail.
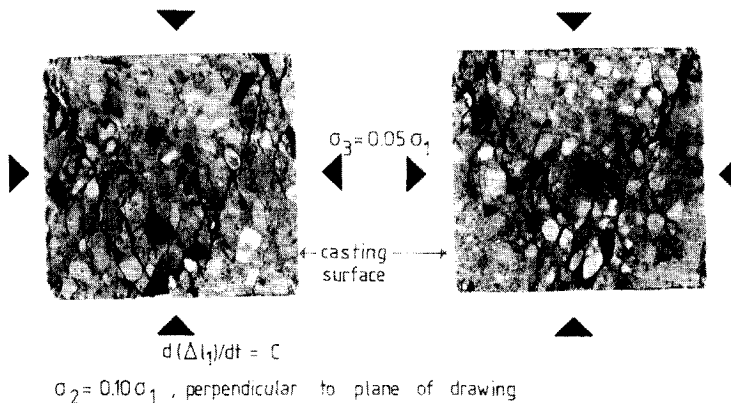
Figure 2.2   Observed shear failure planes under axial compression, σ_1, and low levels of lateral compression, σ_2 and σ_3 [63].

In comparison with the stress state under tension, the compressive loading leads to much more crack arrest, reflected in a much longer interval of stable crack growth and a more pronounced non-linear behaviour.

Under compression, the energy dissipation in the pre-peak fracture process does not occur in a single, localized zone but all through the material. Therefore, the deformation capacity under compressive loading is much larger than under tension. Finally shear bands develop and failure occurs along sliding planes.

The geometry of the final sliding planes and the characteristic load levels in the load-deformation curve will be used in the model, see Chapter 3.

2.4 Failure process under biaxial tension-compression

Thorough studies on the static biaxial loading conditions were performed by Kupfer in 1973 [55] and Nelissen in 1972 [70]. These research programmes resulted in reliable failure envelopes, stress-strain curves and description of the failure modes. Their results still function as references for recent modelling and experimental programmes [103]. More recent experimental programmes deal with triaxial loading conditions [62, 52, 29], post-peak response [63], focused on parameters for numerical material models [59] or loading path [84].

The failure process under tension-compression load can be related to either the tensile or the compressive failure mode. Figure 2.3 shows the observed failure modes by Nelissen dependent on the tension-compression ratio. Note that Nelissen characterized final failure along mutual perpendicular planes, while more recently Van Mier, who was able to perform deformation controlled tests in his research on the post peak behaviour [63], emphasized the shear failure along inclined planes.
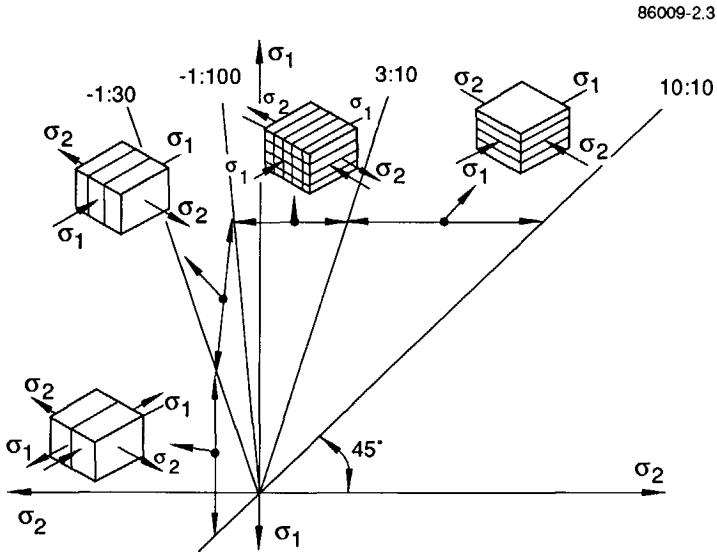
Figure 2.3   The observed failure modes by Nelissen [70].

8

Just like in uniaxial response, the process of crack extension determines the failure process and the failure mode. The compression causes micro-cracking all through the material which decreases the stiffness but increases the deformation capacity. The internal fracture process is clearly reflected in the stress-strain curves and the deformation capacity at ultimate load. Figure 2.4 shows Kupfer's results. The failure strain in the direction of the tensile loading increases in magnitude as the simultaneously acting tensile load decreases. The transition from tensile to compressive failure is accompanied by a pronounced increase of the failure strains perpendicular to the tensile load. Kupfer observed the transition at the compression-tension ratio of about -0.05, while Nelissen reported a ratio of -0.03 to -0.01.

The failure envelopes for the three concrete qualities tested by Kupfer shows that the transition depends also on the concrete quality, see Figure 2.5.
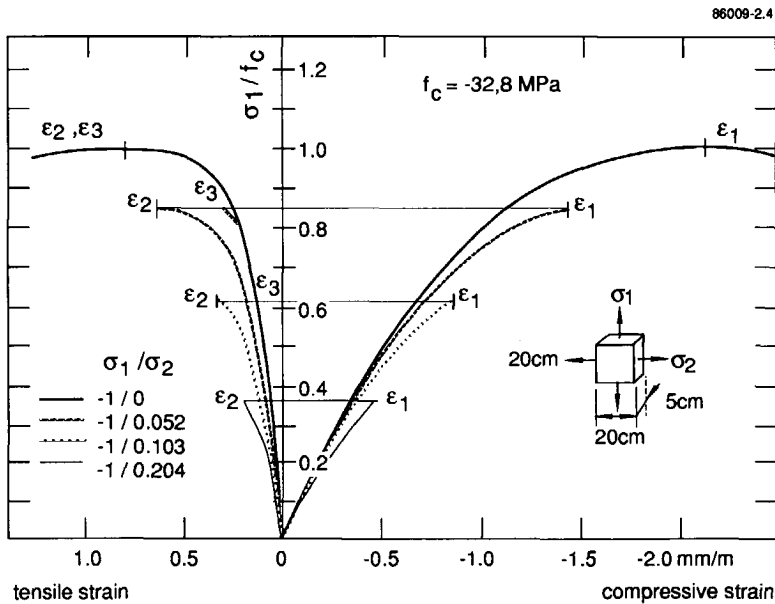
Figure 2.4   The stress-strain relationships of concrete under biaxial tension-compression [56].

The results reported so far refer to monotone and proportional load increase. In [59] Maekawa and Okamura presented results of, amongst other things, initial axial compressive loading and subsequent lateral tensile loading. The specimen size was the same as that applied by Kupfer. Figure 2.6 shows the loading paths and the stress-strain curves due to the tensile loading. Similar to the proportional loading results, a transition from tensile to compressive failure was observed. The transition in failure mode was coupled to the transition from isotropic to anisotropic response, which occurred at a compressive load of about 90% of f_c. From the various loading paths

tested, they concluded that under the compression-tension stress state a unique relation between the biaxial stresses and strains exists. The failure envelopes indicated by stresses and the one indicated by the strains are not affected by the loading path. These results are depicted in Figure 2.7, in which the results of Kupfer are also included.
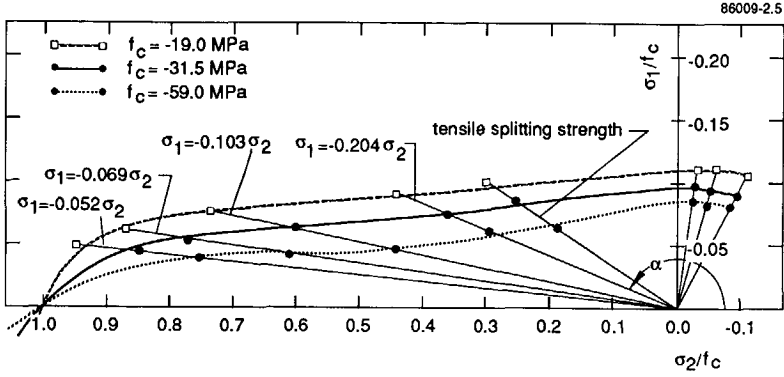
Figure 2.5   The failure envelopes under biaxial tension-compression [56].

(a)   (b)
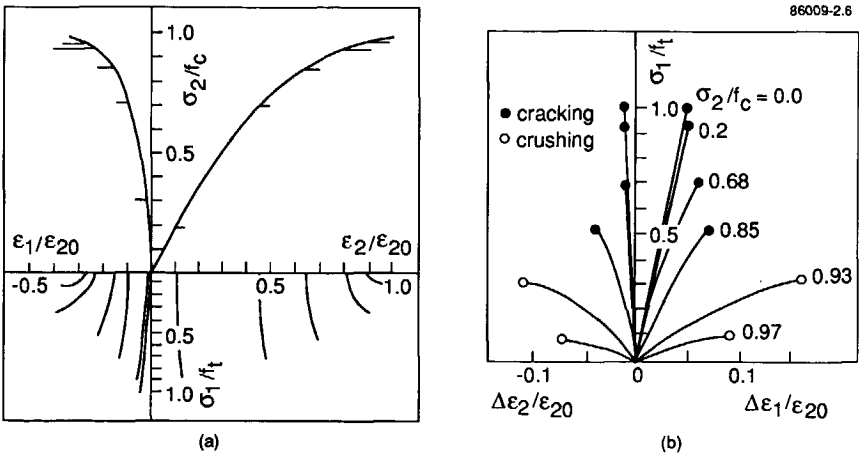
a)   The loading paths
b)   Principal tensile stress and incremental biaxial strains

Figure 2.6   Stress-strain curves under initial, axial compressive loading and subsequent lateral tensile loading [59].
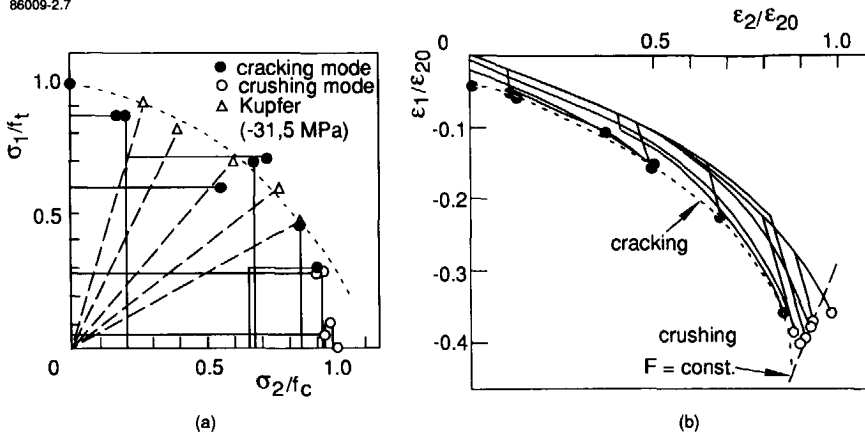
a) Stress paths and failure envelope
b) Strain paths and failure envelope

Figure 2.7 Failure envelopes for biaxial compression-tension [59].

In summary it can be concluded that, under static loading, the biaxial response is governed by the internal fracture process which can be related directly to either the uniaxial response under tension or compression. The loading path does not seem to affect the failure envelope.

A unique shape of the failure envelope is not reported in literature. The differences concern especially the strength data at low compression levels.

The scatter in data are directly related to the sensitivity to experimental technique, casting and loading directions, concrete quality and the accumulated scatter of the independent tension and compression response.

As mentioned before, the results of Kupfer and Nelissen form reliable references. Especially the extensive results of Kupfer will be used as a reference for this study because he studied concrete qualities with similar compressive strengths as tested in the current programme.

2.5   Modelling of failure process

From the description of the failure process of concrete in the previous sections, it emerges that modelling of the response of concrete requires that the deformation and applied load are related to the internal damage level.

Introduction and development of the finite element (FE) technique offered the possibilities of non-linear numerical analyses. The need for adequate models for the complex material response of concrete resulted in the development of many non-linear

and plastic material models closely related to the response of metals and the skills of the FE-programs. Using experimental data, the damage development can be coupled to a loading state, and subsequent yield surfaces can be defined and the parameters of the constitutive relations can be determined [82, 15, 105]. The observed pre-peak response can be described with these type of models. However, these models are not based on the failure mechanism, the fracture process. Furthermore the post-peak response, or the feature of volume increase under compression cannot be described with plastic models.

Another approach, without describing the failure mechanism itself, is presented by the continuous damage models. In these models the internal damage is presented and characterized by a scalar or a vector. When the mechanical properties and the failure process of a material are governed by the degree and extension of the internal damage, the theory deals with the correct parameters to describe the mechanical response of the material.
The theory has been used to describe the change in material properties under various types of loading, e.g. thermal and mechanical, for isotropic [53] as well as anisotropic materials [88].
Løland [58] applied the theory for concrete under tension and derived a one-dimensional stress-strain relation, see also [53] and [61]. The damage level was given by a scalar ω. Considering a critical cross-section, the resistance to an external load was given by the intact material in the failure zone and its Young's modulus. In this approach, the changing stiffness at macroscopic view is governed by ω. Just like in the plastic and non-linear models, Løland described the parameter ω as a function of the strain, and fitted the function to test results.

Note that the continuous damage theory is able to describe the softening behaviour of concrete, because it deals with the dominant parameter: internal damage.
The main disadvantage is that the theory does not describe the real mechanism of damage extension.

The alternatives for including the mechanism are to describe the failure process in detail using powerful computers or focus on a single aspect, e.g. the strength.
The former approach is followed by Mihashi, Wittmann and Zaitsev, for example, who used statistics, fracture mechanics features and the Monte Carlo technique to combine the random material composition and crack extension in the description of the mechanical material response [109, 121, 122]. The alternative is the application of the fracture mechanics approach to describe the extension of decisive cracks.
Fracture mechanics offers the basic tools, i.e. the strength criterion for crack growth initiation and the energy criterion dealing with the energy supply and energy dissipation during crack growth.

For a complex, heterogeneous material like concrete, the application is not simple and led to a great deal of controversy on the applicability of fracture mechanics. In [65] Mindess gave an overview on the application of fracture mechanics on concrete. It goes

beyond the scope of this chapter to summarize the extensive literature that is available on this subject. Just two approaches are mentioned here.

The first one concerns the most simple and straightforward approach of Linear Elastic Fracture Mechanics (LEFM). It deals with the stress criterion and the energy criterion as Griffith formulated in 1920. Because of the assumed linear elastic response of the material around the crack tip, LEFM offers the opportunity to deal with complex loading conditions and crack geometries. The drawback to the relatively simple solutions is the restrained description of the real material behaviour. Using the LEFM parameters of K_{Ic} and G_{Ic}, the critical stress intensity factor and the critical energy release rate respectively, implicitly refer to the instability of a single crack in a homogeneous, isotropic material. The initiation of crack growth is coupled to the instability of the global system. Caution is required for systems or materials where the source of energy release rate is not coupled to the considered single crack [91]. In concrete the local bond and matrix fracture occurs prior to the global instability of the composite material. Therefore, the application LEFM for concrete to describe the failure process is not obvious. Also, application to the pre-peak fracture process under tension should be considered carefully.

When the true material behaviour is not linear elastic, the LEFM approach can only be used when the differences are known and translated to adjusted parameters in the simple model. For example, to include plastic deformation, Dugdale [22] replaced the real crack size for the "effective crack size". A similar approach is followed by Shah and co-workers [39, 40] to incorporate the zone of micro-fracture ahead of the macro-cracks in concrete.

The advantages of the simple, original or modified LEFM solutions should always be related to the concessions in material description and the objectives of the modelling.

A widely accepted alternative, that reflects the specific material behaviour of concrete, is the Fictitious Crack Model (FCM) of Hillerborg and co-workers [33, 67, 75]. The model is related to the plastic models in fracture mechanics which assume a constant yield stress acting in the plastic zone. In the FCM, the resistance of the process zone ahead of the macro-crack is given in a stress-crack width relation representing the softening behaviour of concrete. The dissipated energy, with increasing crack width, is given by the area under the stress-crack opening curve, see Figure 2.8.

Hillerborg and co-workers used FCM to study the degree of approximation due to the application of LEFM [33, 67, 75]. From their study it emerged that LEFM could only be applied in the case where the characteristic dimension of the structure, d, is larger than a tenfold of the characteristic length of the material, l_{ch}. The length, l_{ch} is defined by the tensile strength, Young's modulus and fracture energy, G_f [33].

$$l_{ch} = \frac{E.G_f}{f_t^2}$$

86009-2.8
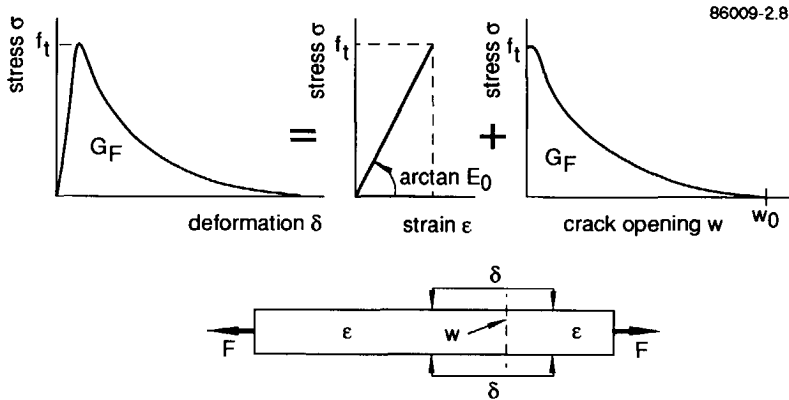
Figure 2.8   The stress-deformation relation separated into a stress-strain and stress-crack opening relation, according the fictitious crack model of Hillerborg [34].

The G_f value is based on the entire failure process and for concrete gives l_{ch}-values of 200-400 mm. When the fracture energy increases even further due to the enlargement of the fracture zone or a more ductile response without a strength increase, the criterion excludes the application of LEFM. For instance, the l_{ch}-value of steel fibre reinforced concrete ranges from 2-20 metres. On the other hand, to characterize the pre-peak fracture process only, the critical dimensions reduce to about 10% of these values.

In this survey, no further attention is paid to the fracture mechanical models or their implementation in numerical codes. Suffice to say that the actual developments and advances in numerical techniques and computer codes enable the application of models like the FCM and do not constrain to LEFM calculations. For recent developments, the work of Rots and De Borst [83, 9] are referred to.
Further attention will be given to the literature on concrete response under impact tensile load and modelling. The given rough sketch for concrete behaviour under static loading and the approaches for a theoretical description serves only as a reference.

2.6   Rate effects on concrete response

The research on rate effects has been focused on the uniaxial loading conditions so far. Extensive reviews on the results have been published, [16, 76, 44, 99, 41]. The experimental work on strength and Young's modulus show a similar feature. Strength and modulus increase with increasing loading rate, while beyond a certain threshold the rate effect becomes more pronounced and a significant increase is observed, especially in strength. Figures 2.9 and 2.10 show the well-known results for

14
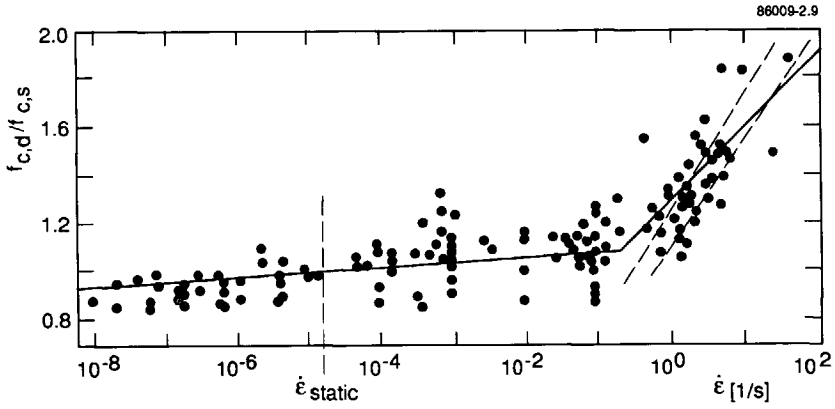
Figure 2.9   The compressive strength as a function of the strain rate [8].
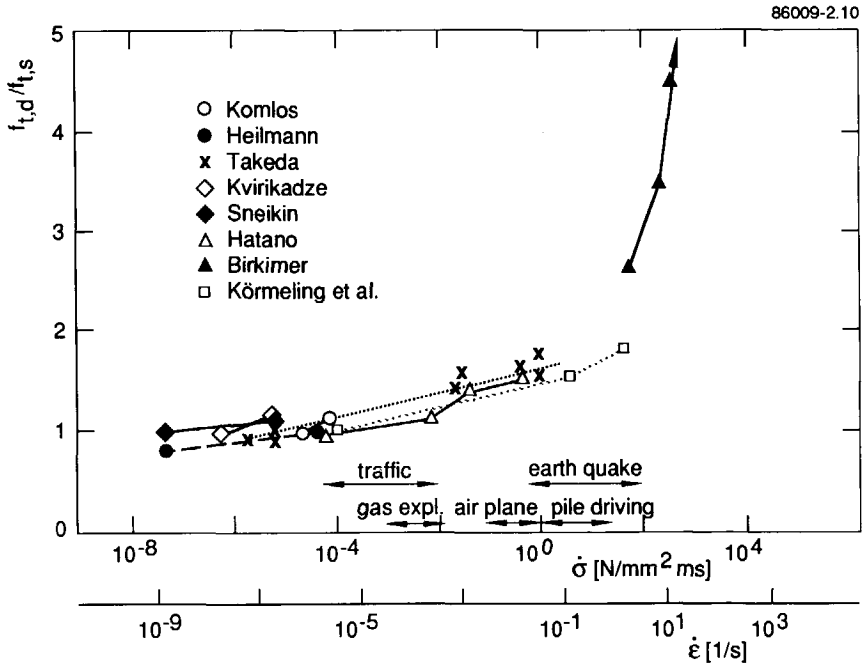
Figure 2.10   The tensile strength as a function of the loading/strain rate [76, 48].

compression [8] and tension [76], respectively. Figure 2.11 [19] shows the dependency of Young's modulus. From these figures it not only emerges that the rate effect on tensile strength is most pronounced, but also that the data of observed Young's moduli hardly justify a conclusion of a steep increase at high loading rates. In the CEB Synthesis Report [16], the moderate increase in Young's modulus is recommended for all loading rates.
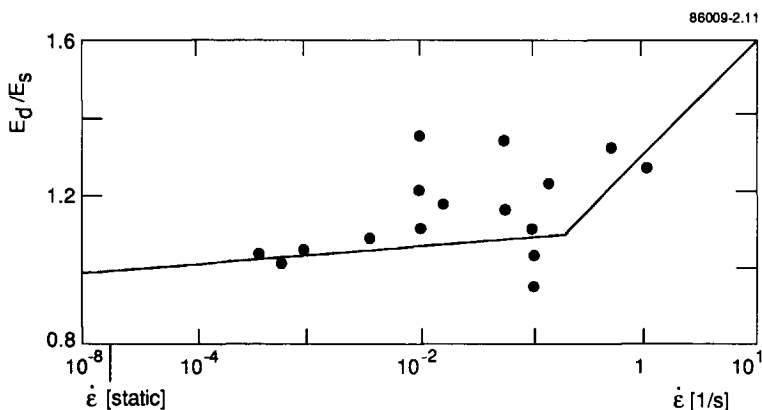
Figure 2.11   Young's modulus as a function of the strain rate [19].

The rate effect is not limited to concrete, it is observed in most materials. The change from the moderate to the steep strength increase, however, occurs at different loading rates, e.g. for ceramics at strain rates of about 10^4 [1/s] [57].

2.7   Modelling of dynamic response

The (moderate) rate dependency of material strength is basically explained by the rate theory [54]. For concrete, the theory was applied by Mihashi & Wittmann [63] and, more recently, Körmeling [48]. The result is a power function with one unknown parameter.

$$\frac{f_d}{f_s} = \left(\frac{\dot{\sigma}}{\dot{\sigma}_0}\right)^\beta \qquad\qquad (2.1)$$

The data in the range of moderate strength increase leads to β values for tension and compression. Published values are, for example,

tension   : $\beta = (10 + 0.50 \, f_{cm})^{-1}$ [16]
                 $\beta = 0.042$ for $f_{cm} = 51$ [MPa]   [124]

compression : $\beta = (5 + 0.75 \ f_{cm})^{-1}$ [16]

                       $\beta = 0.037$ for $f_{cm} = 37$ [MPa]   [63]

with f_{cm} the static cube strength [MPa]

Note that a changing mechanism is not covered by the rate theory, fitting test data for the moderate as well as the steep strength increase compels two β-values.

At Delft University, Zielinski [14] followed a more phenomenological approach to explain the mechanism for the moderate strength increase under tensile loading. He attributed the increase to the changing energy demand to form the fracture plane. He observed a changing geometry of the fracture plane. With increasing loading rate, bond fracture was reduced while the amount of aggregate fracture increased. Furthermore, multiple fracture was observed at high loading rates. These observations and the test data were combined in the model Zielinski proposed [124]. Figure 2.12 shows the various contributions schematically.
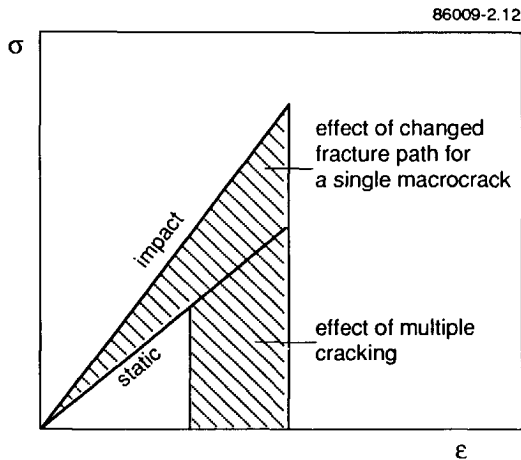
Figure 2.12 Schematic representation of effect of fracture mechanisms on stress strain relationship [124].

Concerning the steep increase at high loading rates, Kipp et al. [46, 47, 31] considered the situation that the fracture process under tension is governed by inertia effects. They used the initial stress distribution around a single crack due to transient tensile load. This distribution is known from LEFM and leads, with the assumption of a constant critical stress intensity factor, to a critical load level, σ_c, as a function of the loading rate. The result for high loading rates is equivalent to equation (2.1),

$$\sigma_c = C \cdot \left(\frac{\dot{\sigma}}{\dot{\sigma}_0} \right)^{1/3}$$

The reference value $\dot{\sigma}_0 = 2$ [GPa/s] leads to a good correspondence with the Birkimer data, see Figure 2.10.

These results indicate that the observed change in rate dependency is caused by a change in dominant mechanism. At low loading rates, the energy barriers of the material dominate the fracture process and the rate dependency, while at high loading rates inertia effects seem to be dominant.

Shah and co-workers developed a two-parameter model for Mode I fracture, which covers the moderate and steep strength increase. Their model [42, 40, 43] is based on LEFM and adjusted, effective crack size, see section 2.5. The influence of the loading rate was included by means of a rate dependent $CTOD_c$, i.e. critical Crack Tip Opening Displacement. In their experiments they observed that the pre-peak crack growth can be substantial for static loading but it decreases with increasing loading rate. Consequently the introduced $CTOD_c$ parameter decreased with increasing loading rate. The $CTOD_c$ was related to static conditions using an exponential expression with two unknown parameters. The benefits of this work are that the influences of scale effects, specimen geometry and loading condition are eliminated [42]. Furthermore, the model can deal with the results of the changing mechanism, see Figure 2.13. Unfortunately, the model does not explain the mechanisms behind the rate dependency.
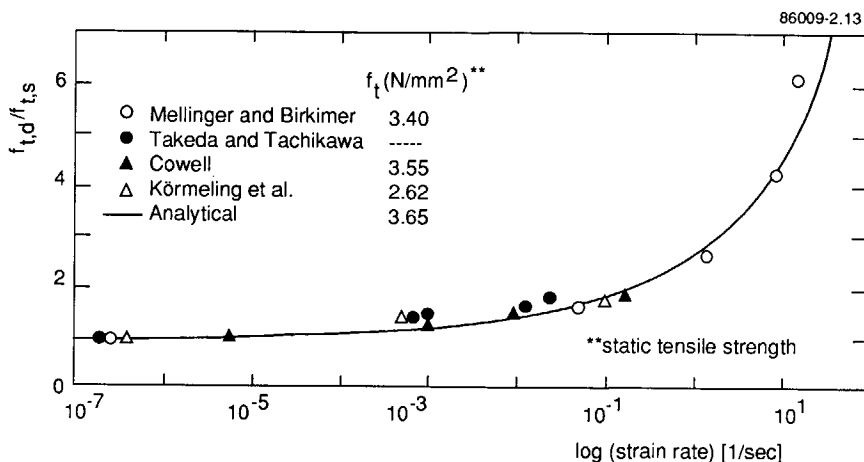
Figure 2.13 Strain rate effect on tensile strength of concrete [42].

In section 2.5 it was already mentioned that the damage theory should be a proper approach for describing the failure process in concrete because the process itself and the mechanical response is governed by the extension of damage in the heterogeneous material.

Shah et al. applied the damage theory to deal with rate effects [44]. The expression for the normal stress in the failure zone may be written (see section 2.5):

$$\sigma = (1-A\,\varepsilon)\,E\,\varepsilon \qquad\qquad (2.2)$$

in which the accumulated damage is given by the product of a constant A and the strain ε, which will be denoted with the scalar ω. Shah proposed a strain rate dependent damage model by introducing a differential equation governing the damage evolution.

$$C\,\ddot{\omega} + \dot{\omega} - A\,\dot{\varepsilon} = 0 \qquad\qquad (2.3)$$

The first term represents the inertia resistance to damage extension. The term vanishes for low strain rates and the expression reduces to equation (2.2). On the other hand, for high strain rates, equation (2.3) leads to a relation between the dynamic strength and the strain rate of the form

$$\sigma_d = C\,\dot{\varepsilon}^{\,1/2}$$

which is similar to the result of Kipp and Grady. For lower strain rates, the parameters introduced have to be derived from test results. More information about this approach is given in [44]. Figure 2.14 shows a comparison between calculations and test results for uniaxial compression.
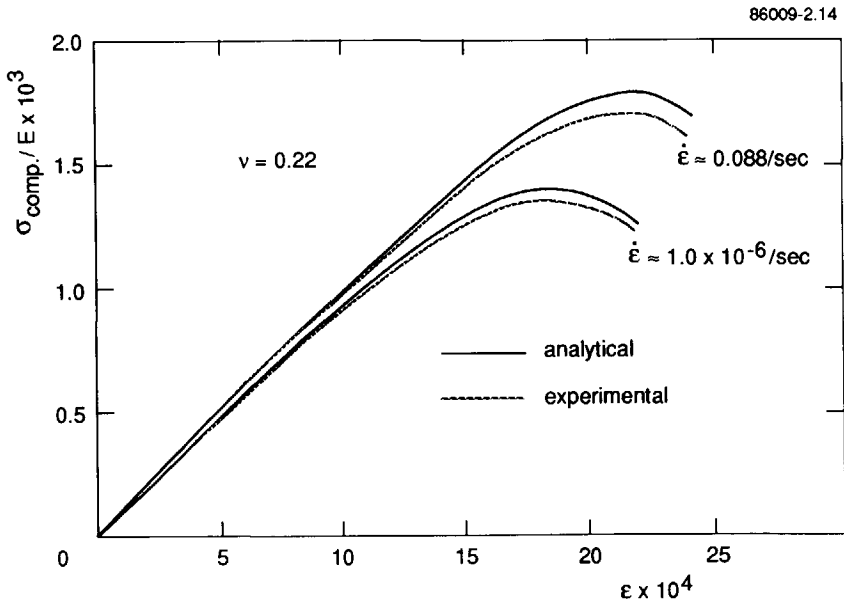
Figure 2.14   Analytical and experimental stress-strain curves in uniaxial compression [100].

Considering the features of concrete response under static loading and the work on rate effects, it is clear that the main parameters are time and degree of damage. Understanding the influence of loading rate on damage extension must be the key to the mechanism of the rate effects in concrete response. The rate theory and damage theory are two options to model the observed rate dependency. A third option is given by fracture mechanics, considering the fracture process and crack extension in the real or schematized concrete material. This approach results in the so called "crack rate models".

To validate these type of models, studies on the crack extension and crack tip velocities are necessary, but these are difficult to perform and very scarce. Reported studies on crack velocities mostly concern the extension of macro-cracks during the softening process, e.g. the work of Curbach and Eibl [17]. Table 2.7.1 gives an overview of observed maximum crack tip velocities [18].

Considering the maximum strength, the pre-peak fracture process and the velocities during the process of micro-cracking should be studied. Only Shah and co-workers focused on the pre-peak fracture process and observed maximum crack rates of about 100 [m/s], reported in [42], which is only a few per cent of the Rayleigh wave velocity.

Table 2.7.1   Maximum crack tip velocities observed under various loading conditions, [18].

Research	maximum velocity [m/s]
Bhargava & Rhenström	180
Mindess et al.	75 - 115
Shah & John	80 (pre-peak)
Muria Vila & Hamelin	800 - 1200 (at $\dot{\varepsilon} \approx 10$ [1/s])
Curbach	500

Referring to dynamic crack growth models for a linear elastic material, see Chapter 3 the work of Freund and Broberg, these low crack tip velocities hardly influence the stress distribution around the crack tip, and the stress intensity factor is not affected. This implies that the rate effect on strength cannot be explained satisfactorily by these crack growth models in combinations with the observed velocities in concrete.

In Germany, Curbach and Eibl [17] followed the roots of dynamic crack growth models and denoted the steep strength increase to a limited crack extension rate. Curbach performed measurements on (macro) crack tip velocities, see Table 2.7.1, and used finite element calculations to determine the stress distribution around a crack tip as a function of the loading rate. He calculated a changing stress distribution, and a decreasing stress intensity at increasing loading rate. It should be noted that Curbach

did not relate his observations to the theoretical limit of the Rayleigh wave velocity, but concluded from the changing stress distribution and the observed maximum crack tip velocity that both phenomena are responsible for the observed strength increase.

In 1984 [113, 72] the author proposed a highly simplified model based on damage extension and fracture mechanics, which showed the same feature as given by Curbach. The model covered the whole range of loading rates and indicated the changing mechanism at high loading rates. Due to the simplifications, the model was not appropriate to study the mechanism itself. Chapter 3 of the current report describes a modification of this model.

2.8   Deformation capacity under dynamic loading

Contrary to strength data, rate effect on deformation capacity is still controversial. The common opinion is that the deformation capacity increases due to rate effects. Figure 2.14 showed some results for compressive loading. The observed differences under tensile loading are illustrated in Figure 2.15, giving load-deformation curves determined by Körmeling from his impact tensile tests with a Split Hopkinson Bar apparatus. Oh performed bending tests at various loading rates and reported a rate effect on the fracture energy according the strength rate sensitivity [72].
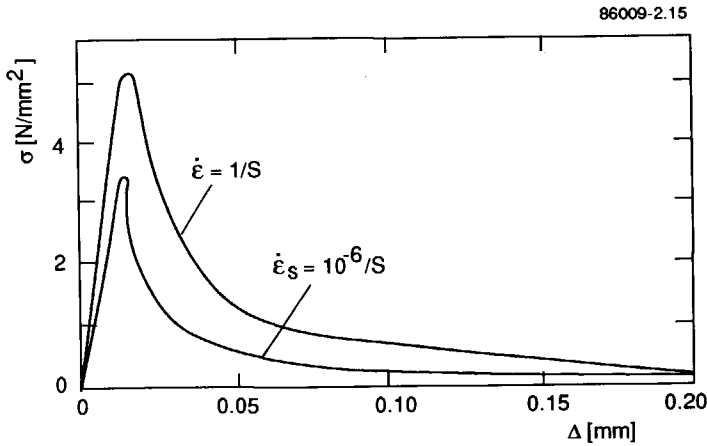
Figure 2.15   Rate effect on load-deformation curve for tension [50].

The controversy emerges when it is realized that the observed material response might be influenced by the structural response of the test set-up and the specimen. The question has to be answered whether the observed difference in deformation capacity and fracture energy should be attributed to the material response or the structural

response. For instance, the observed multiple cracking in uniaxial impact tensile tests changes the width of the failure zone and has a considerable influence on the deformation data. But, what is the influence of the specimen height, and are the multiple fracture zones not just the result of inertia effects in the structure? Hitherto these questions were not treated or even raised in literature. Because the separation of material and structural response in "material testing" may have a significant influence on material modelling, especially for the application in numerical codes, this aspect is emphasized in the currently reported study, see Chapters 5 and 6.

2.9   Rate effect under biaxial loading

The research on rate effects under biaxial loading is limited to just two relevant research programmes, i.e the work of Takeda in 1974 [102] and Zielinski in 1985 [125 and 126]. The latter may be considered as the preceding programme of the current study. In these programmes, the loading condition consisted of static, lateral loading and axial impact tensile loading.
The research of Mlakar et al. [66] and Gran [32] have been discussed in [116], here they are briefly mentioned. Mlakar studied the dynamic tensile-compressive loading using hollow cylinder specimens subjected to axial compression and internal pressure loads. They concluded that the strength increased with increasing loading rates while the deformation at failure was not influenced. The maximum loading rate was 100 [MPa/s] in this study.
Gran studied the axial-symmetric loading condition of laterally compressed concrete under axial dynamic tensile loading. He developed a test set-up in which the deformation of the specimen was measured while the strength was calculated using Young's modulus for static loading. A consistent set of strength data has not been obtained so far.

Takeda performed his tests on cylinders. First the static lateral compressive loading was applied, then the specimens were subjected either to dynamic axial compression or tensile loading. Three rates of loading were applied

-      $\dot{\varepsilon} = 10^{-6}$ [1/s], static condition (S)
-      $\dot{\varepsilon} = 10^{-2}$ [1/s], intermediate condition (III)
-      $\dot{\varepsilon} = 1$ [1/s], impact condition (I)

A description of the loading apparatus and test procedure is not available, only some test results and the final conclusions are reported in literature. Figure 2.16 shows the published results for compression and tension. The numbers denote the level of lateral compression. It emerges that the residual strength increases with increasing compression level and strain rate. The stress-strain curves for tension show that the test procedure led to initial axial compressive stresses which obscure the material response. However, the observed strength and deformation increase significantly at high strain rates.

22

Takeda presented his final test results as a failure envelope, given in Figure 2.17. He concluded that the rate effect on the residual compressive or tensile strength is consistent for concrete at various compression levels. It should be noted that the scatter in the results was considerable. Furthermore, for static loading the shape of the failure envelope in the tension-compression region seems not to be accordance with other experimental data, e.g. Kupfer, see section 2.4. Possibly the results are affected significantly by the experimental set-up. The difficulties and complexity of the biaxial dynamic tests also emerged from the experiments performed by Zielinski and the current study, see Chapters 5 and 7.
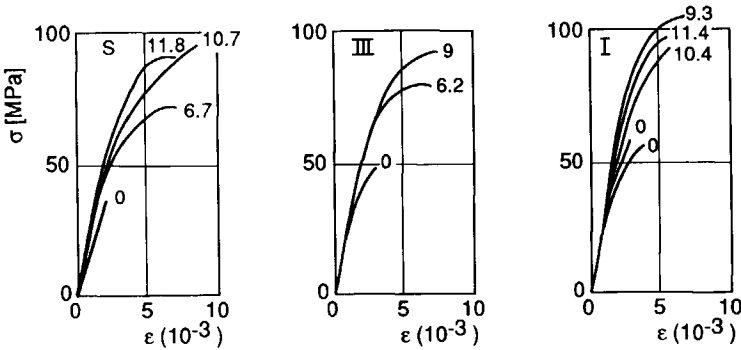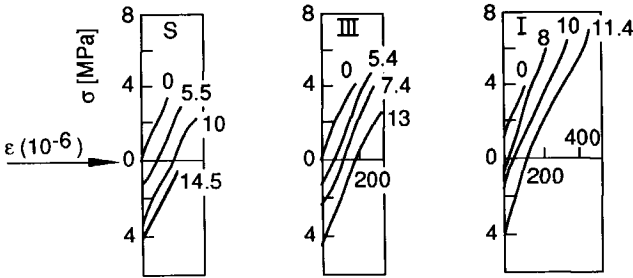
a. compression

b. tension

a) Compression

b) Tension

Figure 2.16 Stress-strain curves under static lateral compression and dynamic axial compressive (a) and tensile (b) loading, [102].

Zielinski used a modified Split-Hopkinson bar set-up. A hydraulic prestressing device was added to apply lateral compression in one direction. The geometry of the specimens was prismatic and notches were applied to predetermine the location of failure zone. The test procedure and results are described in [125, 126, 117] and some comments are given in Chapter 5.

Zielinski performed static and dynamic tests on a high and a low quality concrete. The strength data are plotted in Figure 2.18 in which the drawn envelopes correspond to the Griffith criterion. Zielinski came to the same conclusion as Takeda, i.e. the rate effect on the residual impact strength is not affected by the level of static, lateral compression. Consequently, the failure envelopes have a similar shape under static and dynamic loading.

If the conclusions of Takeda and Zielinski are correct, the rate effect is known and easy to handle for the loading condition mentioned. The mechanism behind this result, however, is unknown and also the considerable scatter in data does neither justify nor dispute the conclusion.
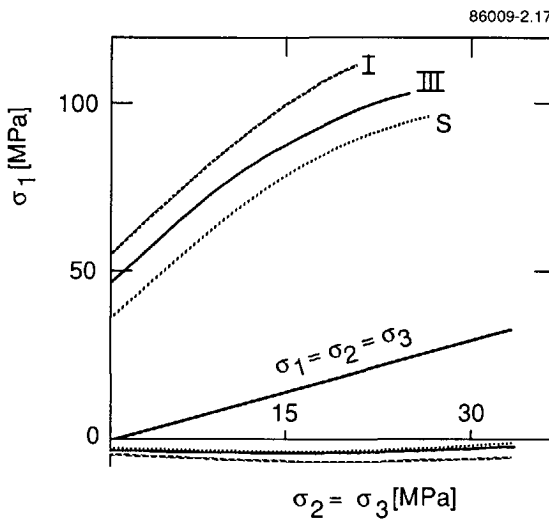
Figure 2.17   The failure envelopes, Takeda [102]

Considering the induced internal stresses and damage due to the lateral compression, some scenes can be composed to get an idea about the failure mechanism and validity of the observed rate effect. When the failure process is simplified and schematized, the applied energy in the tensile loading can be absorbed in two extreme ways. First, a single failure plane is formed and all the applied energy is used to create this failure

plane. Due to the lateral compression and the associated damage, the energy demand will depend on the compression level. Referring to the mechanism for the rate effect under uniaxial tensile loading, the approach of the single failure plane will not result in a unique formulation of the rate effect. The rate effect will decrease with increasing compression level.

The second option is that the applied energy is initially distributed among multiple cracks all through the material and, at a later stage, the final shear or failure planes are formed. With increasing loading rate the multiple crack extension will last longer, resulting in an increasing energy demand with increasing loading rate. The geometry of the failure plane(s) will depend on the compression level as it does in the first option. In this situation, however, the rate dependency of the failure envelope cannot be predicted.

When both options are considered, it is possible, but unlikely, that the rate effect is independent of the compression level.
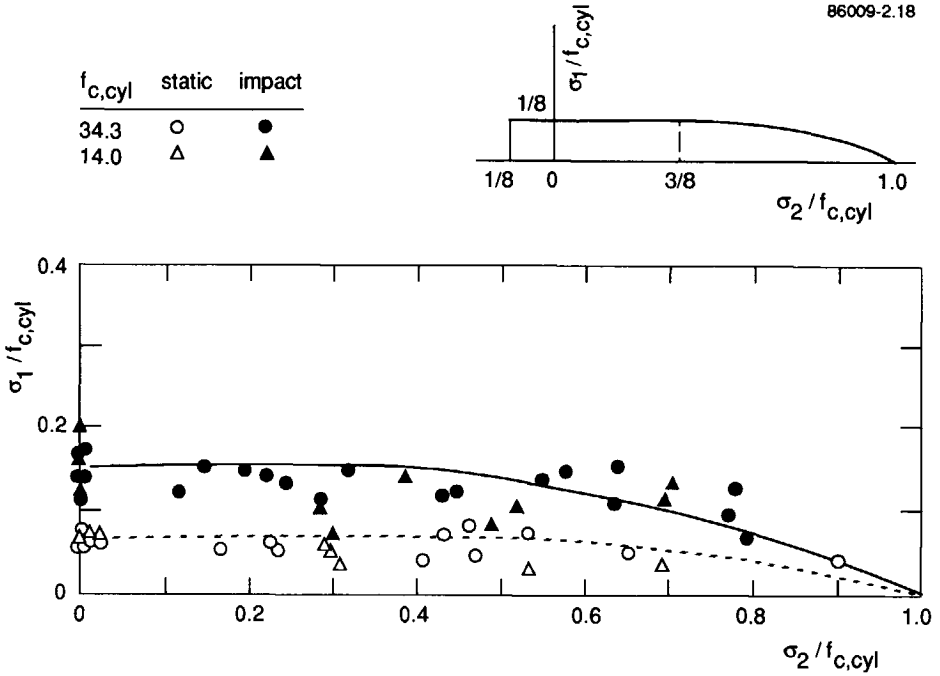
Figure 2.18   Strength data and failure envelopes, Zielinski [125].

Considering the few experimental programmes it is not surprising that hardly any modelling of the response under multi-axial dynamic loading condition has been performed. In this framework, it is important to mention the work of Suaris and Shah who extended the application of the damage theory to multi-axial dynamic loading

[100, 44]. The damage scalar ω in equation (2.7.2) is replaced by a damage vector, whose direction depends on the loading condition. Application of this theory on the condition of proportional tensile-compressive loading, and using the Kupfer data, the static and dynamic failure envelopes are obtained as given in Figure 2.19. Coupling of the rate effect to the specific failure mode will lead, also for static prestressing, to the conclusion of a non-unique rate effect. Note, that the effect of multiple crack growth was not included in the damage model.
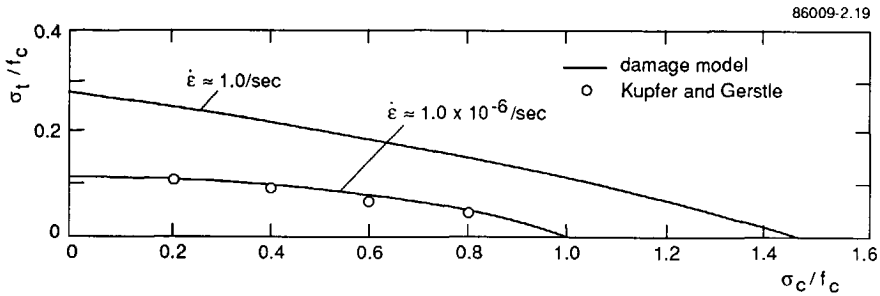
Figure 2.19 The static and dynamic failure envelope resulting from the damage theory, [100].

In Chapter 4, a model is presented for the biaxial loading condition of static lateral compression and axial impact loading. The model deals with the induced damage and internal stresses due to the preloading, and the damage extension during the impact load. In Chapters 4 and 7 further attention will be paid to the aspects of the shape of the failure envelope and the possible influence of multiple crack initiation.

3 MODEL FOR UNIAXIAL TENSILE STRENGTH

Based on the fact that the behaviour of concrete is governed by the extension of the present internal damage, a model was developed to describe the rate effect on the fracture process. First the potential fracture plane in concrete was schematized to a fictitious fracture plane with equally distributed penny-shaped cracks. The extension of these cracks was described by using LEFM, resulting in a time and loading rate dependent description of the fracture process. The objective of the model is to characterize the prepeak fracture process and describe the rate dependency of tensile strength.

3.1 Fictitious fracture plane

To characterize the geometry of a fracture plane under uniaxial tension, the approach of Walraven [108] and Zielinski [124] was followed. The aggregate particles were schematized to randomly distributed spheres. No cast direction was considered. The amount of aggregate is given by the ratio of aggregate and concrete volume and denoted by p_a.

The potential fracture plane is formed by a section through the material. It is composed of fracture surfaces due to bond A_b, matrix A_m and aggregate A_a failure. To distinguish the development of aggregate or bond fracture, the critical angle φ_c was introduced, see [124 and 114] and Figure 3.1. Aggregate fracture was assumed to occur only when the section plane intersects the particle for φ values smaller than φ_c.

86009-3.1
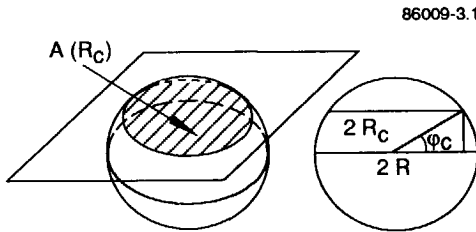
Figure 3.1   Section through sphere with radius R and angle of incident φ_c.

The area of the tortuous fracture plane, A_{fr}, can be determined with the parameters p_a and φ_c [114].

$$A_{fr} = A_m + A_a + A_b \tag{3.1}$$

with

$$A_m = (1-p_a) \cdot A$$

$$A_a = \xi_c \cdot p_a \cdot A$$

$$A_b = 2 \ln \frac{2}{1+\xi_c} \cdot p_a \cdot A$$

$$\xi_c = \sin\varphi_c$$

In these expressions, A is the projected area of the fracture plane. Due to bond fracture along the sphere caps, the fracture plane has a tortuous shape and the ratio A_{fr}/A may be significantly larger than one.

To characterize the failure process in the real fracture plane, a fictitious fracture plane was introduced. The internal damage which is decisive for the initiation of crack growth was schematized as penny-shaped cracks with radii a_b. These flaws were equally distributed at a centre to centre distance of $2b$. Figure 3.2 shows the planes of fracture in concrete and model. Around these initial cracks, a zone of bond fracture and a zone of matrix and aggregate fracture were drawn. The zones are determined by the (crack) radii a_b, a_{m+a}, and b. These zones represent the corresponding components in the real fracture surface.
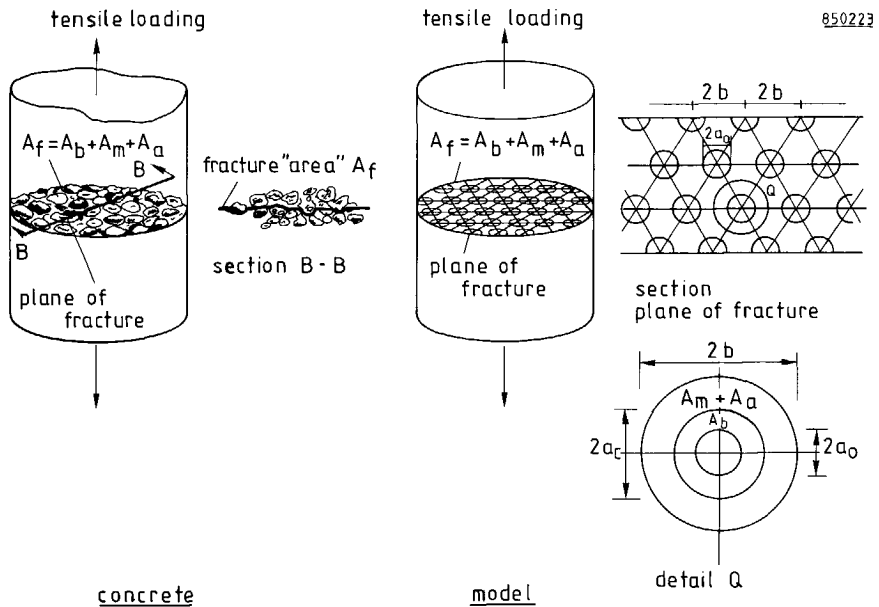
Figure 3.2   Fracture planes in concrete and model under tensile loading.

Referring to Chapter 2, the relation between the failure process in the real material and the schematized material is as follows.
Up to the elastic threshold of $f_{t,b}$, no crack extension occurs in concrete or model. At this threshold the critical state is reached for the present internal damage and bond failure is initiated. In the model this was presented by the stress and energy criterion for the penny-shaped cracks with radii a_b. It was assumed that up to the level of $f_{t,m+a}$, the bond failure is established. At this load level the critical state of matrix and aggregate fracture is reached. The literature does not clearly distinguish between

aggregate and matrix fracture. Therefore, these stages were coupled and the critical crack radius at $f_{t,m+a}$ is given by a_{m+a}. With increasing load the cracks grow and reach their maximal value b at maximum load level f_t.

The decision to characterize the pre-peak fracture process of micro-cracking by the extension of penny-shaped cracks in a fictitious fracture plane, requires some additional comment.
Referring to Chapter 2, heterogeneity, local damage and internal peak stresses result in micro-cracking before the maximum strength is reached. Micro-cracking will not be limited to a single plane but a fracture zone is formed. At maximum strength and during the softening process the micro-cracks coalesce, bridging occurs and at that stage the final fracture plane is formed by macro-cracks. The base, however, for the final fracture plane, failure process and energy dissipation is the pre-peak fracture process. Therefore, the observed geometry of the final fracture plane was used in the model, and the energy needed to form the various components was considered to be a proper parameter to characterize the energy dissipation in the pre-peak fracture process.
With this approach, no absolute quantitative representation of the pre-peak fracture process can be given, but it is expected to be able to reflect changing concrete properties and rate effects on strength.

To quantify the geometry and the parameters of the fictitious fracture plane, the initial damage had to be determined and characterized, the energy requirements for crack propagation in material and model had to be related, and the thresholds in load levels were applied as strength criteria for crack growth. These steps are described in [114 and 119] and summarized in the next sections.

3.1.1   Initial concrete damage

In concrete, the initial decisive damage is somehow related to the aggregate particles on which the fracture process starts as bond failure. Simplifying the composition of concrete to spheres embedded in a homogeneous mortar [108, 124, 114] and adopting the approach of Zaitsev [110], the initial damage was characterized as follows.

Each spherical inclusion, or aggregate, has one pre-existing defect at the bond surface. Isotropy was assumed and the orientation of the defects is random. It should be noted that these assumptions are important for the biaxial model, see Chapter 4. Furthermore, it was assumed that the largest particles have the largest defects which are decisive for the initial damage. To define the size of these particles the aggregate grading can be used when available. If not, the Fuller distribution is adopted and the chance of the particle diameter being smaller than a value D, is given by:

$$p_d = \sqrt{\frac{D}{D_{max}}} \tag{3.2}$$

in which D_{max} = the maximum aggregate diameter.

The chance, $1-p_d$, for the decisive initial damage is denoted by p_c. Consequently, the mean size of the considered particles is given by:

$$D = (1 - \frac{p_c}{2})^2 \cdot D_{max} \tag{3.3}$$

To determine the intermediate distance d of the particles with diameter D, the most dense package configuration, i.e. the faced centered cubic package, was assumed. The considered geometry is depicted in Figure 3.3.
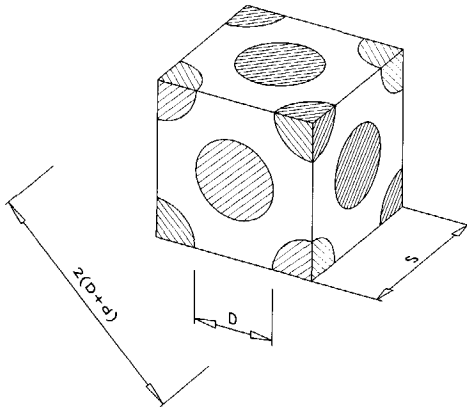
Figure 3.3   The considered package, faced centred with intermediate distance d.

Using the aggregate ratio p_a in the assumed package, the volume ratio of the decisive particles is given by the product:

$$p_c \cdot p_a = \frac{\pi}{3\sqrt{2}} \cdot \frac{D^3}{(D + d)^3} \tag{3.4}$$

With this relation, the intermediate distance, d, is known.

Due to the presentation of the real, tortuous fracture plane in a two-dimensional fictitious plane, the intermediate distance between the initially present flaws was enlarged by the factor $\sqrt{(A_{fl}/A)}$.

3.1.2 Fictitious fracture plane for uniaxial tension

In the fictitious fracture plane, the penny-shaped cracks are surrounded by a linear-elastic material, divided in zones with different specific surface energies. Using the strength criterion from the LEFM theory, the critical load levels of $f_{t,b}$ and f_{m+a} and the initial damage characterization given in the former section, the size parameters of the plane are given by, see [114]:

$$a_b = \frac{\pi}{4} \cdot \frac{2\gamma_b\, E_m}{1-\upsilon_m^2} \cdot \frac{1}{f_{t,b}^2} \cdot \frac{1}{f^2\left(\frac{a_b}{b}\right)} \tag{3.5}$$

$$a_{m+a} = \frac{\pi}{4} \cdot \frac{2\gamma_{m+a}\, E_m}{1-\upsilon_m^2} \cdot \frac{1}{f_{t,m+a}^2} \cdot \frac{1}{f^2\left(\frac{a_{m+a}}{b}\right)} \tag{3.6}$$

$$b = a_b + \frac{1}{2} \cdot \sqrt{\frac{A_{fr}}{A}} \cdot (D + d) \tag{3.7}$$

In these formulae

E_m = Young's modulus of matrix
υ_m = Poisson's ratio of matrix
γ = specific surface energy
$f(a/b)$ = geometrical function to take the finite dimensions into account, see section 3.2.6

Apart from the known static material properties, the specific surface energies, the critical angle φ_c and the reference surface area A are unknown. This number was reduced to three by relating the fracture surfaces of the real fracture plane to the circular zones in the fictitious plane.

In Annex 1 the equations are listed to determine the geometry of the fictitious fracture plane. The procedure to calculate the geometry was implemented in a numerical program.

It is suggested to use the following input parameters: f_t, E_m, υ_m, p_a, p_c, D_{max}, γ_b, γ_m, γ_a, and for $f_{t,b}$ and $f_{t,m+a}$, the values 0.6 and 0.8 f_t, respectively.

The specific surface energies can only be estimated. The literature surveys of Ziegeldorf [123], Swamy [101], Zielinski [124] and, more recently, Hordijk [35] show a considerable scatter in numbers on fracture mechanical parameters. The parameters are derived from flexural tests on notched beams, splitting tests or from direct tensile tests and presented as K_{Ic} and G_{Ic} values, or as a G_f value when the energy is measured or calculated up to failure.

Referring to the introduced simplifications to cover the real material response by a LEFM approach, the variety of material components and the influence of specimen size and test method, the scatter in data is inevitable and has to be accepted.
A range for the values is given in Table 3.1. Note, the parameters are not always presented as a set in literature.

Table 3.1 K_{Ic} and γ-values [124, 123, 101, 2, 13, 28]

	K_{Ic} [MN/m$^{3/2}$]		$G_{Ic} = 2.\gamma$ [J/m^2]	
	average	range	average	range
Mortar	0.55	0.15 - 1.3	17.5	4 - 40
Bond interface	0.3	0.1 - 0.8	(0.4 - 1) G_{Ic}**	
Aggregate	2.8	2.0 - 3.5	100*	65 - 300
Concrete	0.85	0.55 - 1.2	16.0	11 - 21

*   Quartsite [28]
**   Data is scarce; range given in [124] expressed in G_{Ic} (mortar)

The main disadvantage of the introduced scheme is the necessity to estimate input parameters. The number can be reduced to one, when a single zone around the initial flaws is considered and the mean specific surface energy of the fracture plane in concrete is used. However, the more detailed approach offers the opportunity to study the effect of changes in composition and material properties on the geometry of the fictitious fracture plane and with that, on the prediction of rate dependency, which is the aim of the model.
Furthermore, the detailed approach can be directly linked to the representation of the failure planes under compression.

3.1.3   Fictitious fracture plane for uniaxial compression

The internal fracture process under uniaxial compression was modelled analogously to the schematization of the fracture process under uniaxial tension. The analogous approaches for tension and compression enabled us to cope with the biaxial condition of lateral compression and subsequent axial tensile loading, which is the final loading condition considered in this study.
In Chapter 2, the failure process under uniaxial compression was summarized. To characterize the pre-peak fracture process for compression, the development of bond and mortar fracture had to be represented in the fictitious fracture plane. Because under compression, fracture occurs all through the material, it is better to speak about a fictitious fracture plane. In such a plane, crack growth is representative for damage

extension and energy absorption in the real material. To represent the pre-peak fracture process, a section was considered parallel to the compressive load and consequently, perpendicular to the average direction of the induced internal tensile stresses. With this choice, a fictitious fracture plane for compression was also oriented perpendicular to the subsequent tensile load in the biaxial loading condition to be considered.
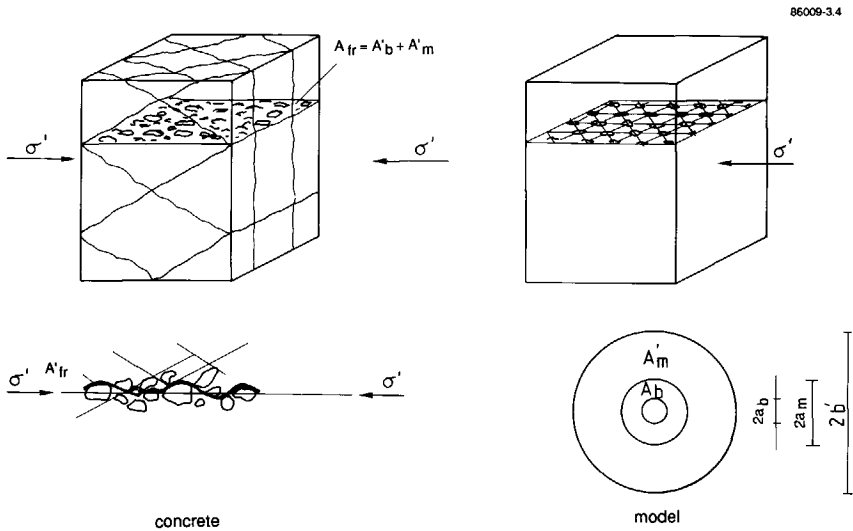
Figure 3.4   Fracture plane in concrete and model under compressive load.

Similar to the procedure for tensile loading, the geometry of the considered fictitious fracture plane followed from relating the geometry of the tortuous fracture plane in concrete to the scheme of co-centrical zones around equally distributed initial flaws. The schematization is depicted in Figure 3.4, while the procedure to determine geometry of the fictitious fracture plane was described in [114] and [119]. A summary is given below.

The aggregate particles were assumed to be spheres randomly distributed. Under this assumption, the pre-peak fracture process consists of bond fracture along sphere caps and mortar fracture along the surface of the compression cones on the aggregates, see Figure 3.5. To determine the geometry of the tortuous fracture plane it was assumed that

- no aggregate fracture occurred and

- the critical angle to distinguish bond and matrix fracture was constant and equalied 60°, [98] and [63].
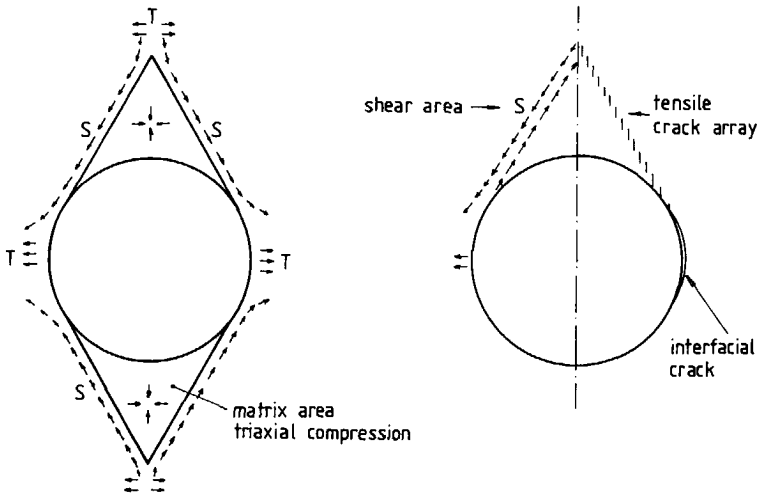
Figure 3.5 Cross-section of sphere and compressive cone, with S and T referring to shear and tensile stresses, respectively.

The area of the fracture surface was denoted as A_{fr}' and equals the sum of the bond and matrix components A_b' and A_m', respectively, see Figure 3.4. Contrary to the situation under tensile loading, the area A_{fr}' of the tortuous fracture plane could be related directly to its projection area A. The random distribution of the aggregates and both assumptions given above, allow the explicit determination of the components A_b' and A_m'. The components only depend on the aggregate content and are given by, see [114 and 119]

$$A_b' = 0.139 \, p_a \, A \qquad (3.8a)$$

$$A_m' = (1.367 - 0.183 \, p_a) \, A \qquad (3.8b)$$

The next step in the modelling procedure was to determine the radii a_b', a_m', and b' of the initial flaws and the zones of bond and mortar fracture, respectively. Dealing with the same material as under tensile loading, implicated that the initial flaw size a_b was known, while the ratio A_{fr}'/A and the expressions given above resulted in a unique expression for the radius b'.

To determine radius a_m', the areas of bond and matrix fracture in concrete, given in expressions (3.8), and the geometry of the co-centrical zones in the fictitious fracture plane were related. The energy dissipation per unit area has to be the same for concrete and model. This condition resulted in an expression for a_m'. The radii a_m' and b' are given by

$$a_m' = \sqrt{\frac{0.139 \, p_a \, A}{\pi} + a_b} \qquad (3.9)$$

$$b' = a_b + \frac{1}{2}\sqrt{\frac{A_{fr}'}{A}} \cdot (D + d) \tag{3.10}$$

Transcription to a fictitious fracture plane, similar to the procedure under tension, means that the internal stresses have to be related to an equivalent tensile loading perpendicular to the plane. In the description of the biaxial model, this aspect will be discussed in more detail. Here, it suffices to introduce two thresholds of induced tensile stresses. The first threshold is the equivalent tensile loading for initiation of bond fracture and the second is the one for the initiation of matrix fracture.

$$\sigma_{eq,b} = \delta_b \cdot f_{c,b} \tag{3.11a}$$

$$\sigma_{eq,m} = \delta_m \cdot f_{c,m} \tag{3.11b}$$

with $f_{c,b}$ and $f_{c,m}$ the critical load levels for bond and matrix failure.

The values of δ_b and δ_m follow from the strength criteria of LEFM for the onset of the corresponding fracture processes in the fictitious fracture plane. Application of these criteria resulted in the following relations between the crack radii a_b and a_m' and the critical load levels of the equivalent tensile loads $\sigma_{eq,b}$ and $\sigma_{eq,m}$, see [114 and 119].

$$a_b = \frac{\pi}{4} \cdot \frac{2\gamma_b \, E_m}{1 - v_m^2} \cdot \frac{1}{(\delta_b \cdot f_{c,b})^2} \cdot \frac{1}{f^2(\frac{a_b}{b})} \tag{3.12}$$

$$a_m' = \frac{\pi}{4} \cdot \frac{2\gamma_m \, E_m}{1 - v_m^2} \cdot \frac{1}{(\delta_m \cdot f_{c,m})^2} \cdot \frac{1}{f^2(\frac{a_m'}{b'})} \tag{3.13}$$

From the approach described, it follows that a representative failure plane under compressive loading can be translated to a fictitious fracture plane similarly to the procedure for uniaxial tensile fracture. No additional, unknown parameters had to be introduced.

By following a similar approach for tension and compression, the static material parameters and response characteristics could be related to both fictitious fracture planes which increased the consistency of the model.

3.1.4 Evaluation of fictitious fracture plane

The scheme of the fictitious fracture planes under tension and compression can be established with the procedure given in the former sections. The evaluation of the procedure [119] revealed that changing concrete properties and composition were reflected in the geometry of the fictitious fracture planes satisfactorily.

Some general features of the model are:
- the ratio a_b/b is representative for the degree of initial damage. It increases with decreasing concrete quality;
- the scale size, represented by the area A, is dominated by the aggregate skeleton;
- the system is stable; changing a certain parameter is, partly, compensated by the response of other parameters.

Most of the input parameters for the calculation of the fictitious fracture planes are mutually dependent. In [119] empirical relations were used to incorporate this interdependency. Here however, the effect of composition and material properties on the various energy terms will be illustrated by varying the parameters independently.

Table 3.2 Parameters for tested, high quality concrete (Mix A)

Input from static tests				Input data estimated			
$f_{t,s}$	=	2.98	[MPa]	$\star$	E_a	= 60	[GPa]
$f_{c,s}$	=	35.2	[MPa]	$\star\star$	υ_m	= 0.2	
E	=	33.9	[GPa]		γ_a	= 50	[J/m^2]
p_a	=	0.77			γ_m	= 10	[J/m^2]
p_c	=	0.05			γ_b	= 5	[J/m^2]
D_{max}	=	8	[mm]				

Geometry of fracture plane							
a_b	=	1.91	[cm]	a_{m+a} = 2.57	[cm]	b = 2.98	[cm]
A_{fr}	=	1.65 10^{-3}	[m^2]	A = 1.49 10^{-3}	[m^2]		

Calculated fracture energies				
U_b	(ref) / A	=	6.3	[J/m^2]
U_m	(ref) / A	=	4.6	[J/m^2]
U_a	(ref) / A	=	25.7	[J/m^2]
U_{tot}	(ref) / A	=	36.5	[J/m^2]

$\star$ E_m follows from E_a, E and the aggregate contents
$\star\star$ The exact value of υ_m has a minor influence on the result.

The high quality concrete, experimentally tested, was taken as a reference. Subsequently, D_{max}, p_a and the ratio γ_b/γ_m were altered. The reference values are listed in Table 3.2 while the results are depicted in the Figures 3.6-3.8.

The increase of the aggregate content is coupled to an overall energy increase. Changing the aggregate contents is reflected in the fictitious fracture plane as a gradual transition from mortar to bond and aggregate fracture.

The calculated result also shows a predicted change from bond to aggregate fracture with increasing p_a. The larger aggregate ratio decreases the intermediate distance of the initial defects and reduces the fraction of mortar fracture. The system responds to this relative energy loss by means of the transition to aggregate fracture.

Note that in the scheme for the low-quality concrete (Mix B), with a high aggregate content but also a lower strength and fracture energy, the bond fracture is larger than for the high quality concrete (Mix A).

From experiments it is known that the fracture energy grows with increasing aggregate diameter [35]. This feature is reflected in Figure 3.7 which also shows a transition from bond to aggregate fracture. Because all the other parameters were kept constant, the decreasing aggregate number forced this change in geometry.

Figure 3.8 shows the changes in the energy terms when the ratio γ_b/γ_m increases. The results are predictable, increasing the energy demand for bond fracture favours the aggregate fracture and results in an overall increase of the fracture energy.

As a complementary illustration, the scheme for the low quality concrete is listed in Table 3.3.
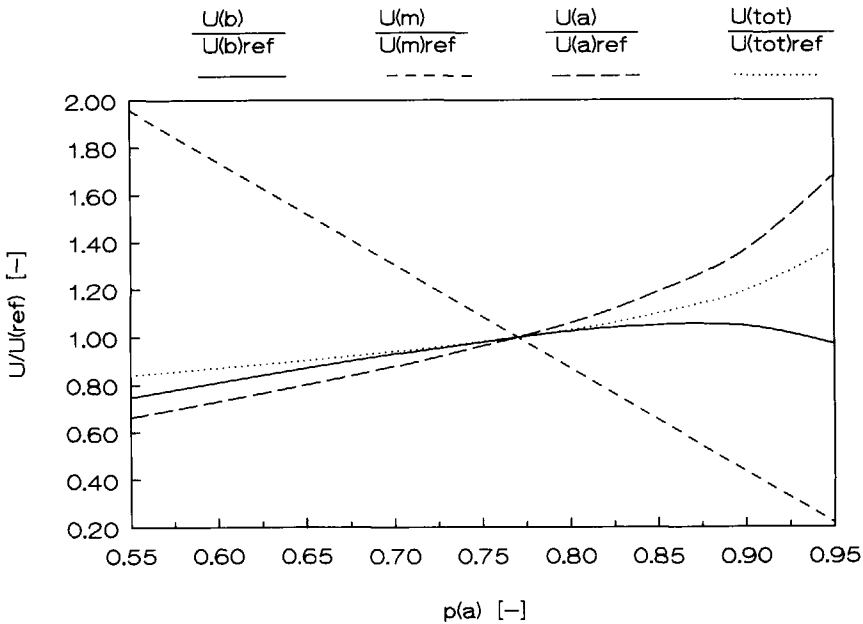
Figure 3.6   The fracture energies versus aggregate contents, p_a.
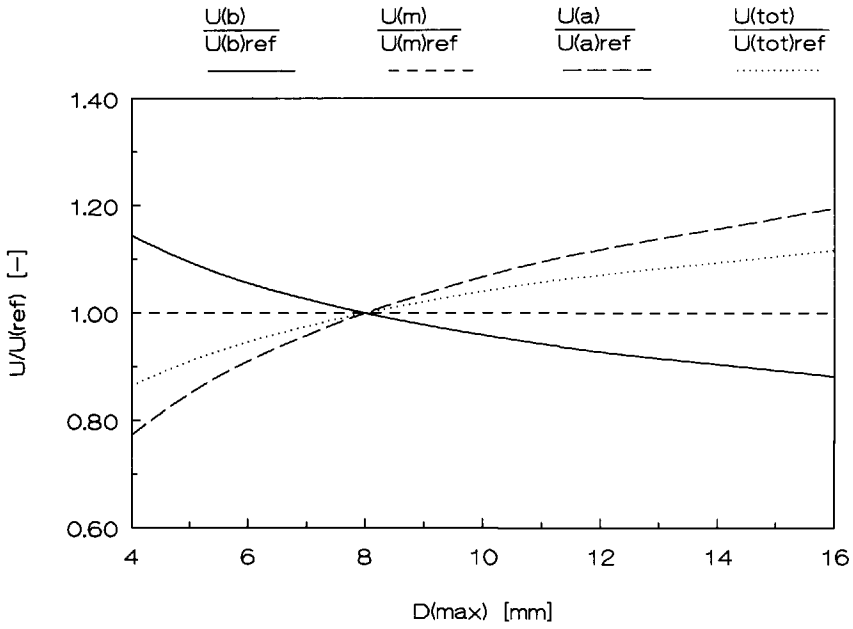
Figure 3.7   The fracture energies versus maximum aggregate size, D_{max}.
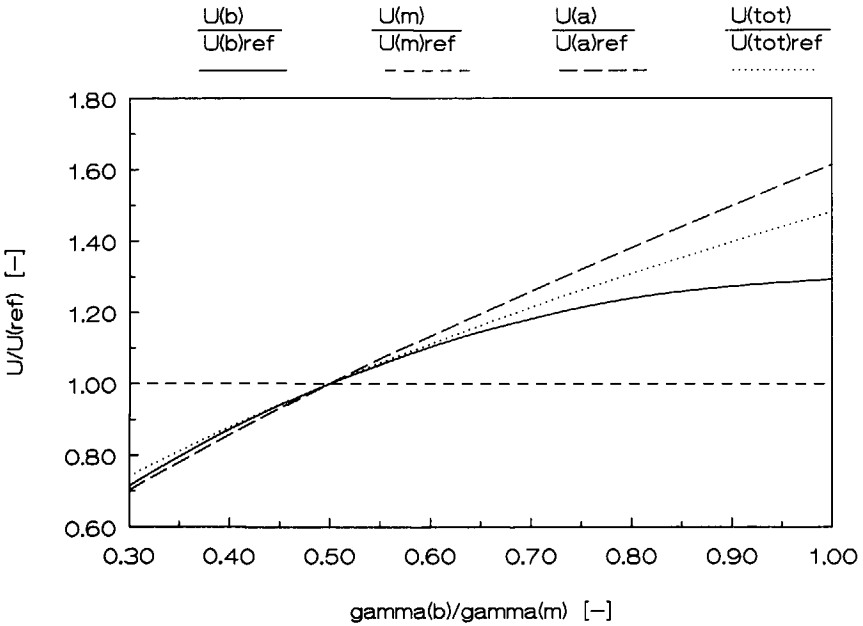
Figure 3.8   The fracture energies versus γ_b / γ_m

Table 3.3   Parameters for tested, low quality concrete (Mix B)

Input from static tests				Input data estimated			
$f_{t,s}$	=	1.63	[MPa]	E_a	=	60	[GPa]
$f_{c,s}$	=	19.4	[MPa]	υ_m	=	0.2	
E	=	30.9	[GPa]	γ_a	=	50	[J/m^2]
p_a	=	0.86		γ_m	=	5,6	[J/m^2]
p_c	=	0.10		γ_b	=	2,8	[J/m^2]
D_{max}	=	8	[mm]				

Geometry of fracture plane

a_b	=	1.77	[cm]	a_{m+a}	=	2.44	[cm]	b	=	2.59	[cm]
A_{fr}	=	1.12 10^{-3}	[m^2]	A	=	0.91 10^{-3}	[m^2]				

Calculated fracture energies

U_b (ref) / A	=	5.5	[J/m^2]
U_m (ref) / A	=	1.6	[J/m^2]
U_a (ref) / A	=	11.9	[J/m^2]
U_{tot} (ref) / A	=	19.0	[J/m^2]

3.2   Crack extension

The objective was to determine the crack extension in the fictitious fracture plane as a function of time and loading rate. This was realised by using LEFM as a tool.
In literature, no solutions have been reported for similar crack geometries, as given in the fictitious plane, under dynamic Mode I loading. However, some aspects of the currently considered geometry and loading condition have been investigated and published in literature.

3.2.1   Balance of energies

To derive relations for crack growth, the energy balance for the zone around the crack tip had to be considered. After the strength criterion is fulfilled the fracture is governed by the balance between the supplied energy, the stored energy and the dissipated energy. In the most general case, the thermodynamic equilibrium of the energy terms is given by:

$$\frac{dW}{dt} = \frac{dE_v}{dt} + \frac{dE_k}{dt} + \frac{dE_d}{dt}$$

(3.14)

in which W is the work done by the external loads, E_v is the recoverable component of the stored energy, E_k is the kinetic energy, E_d is the sum of the irreversible energy such as the fracture energy and t is time.

The various energy terms can be determined when the stress, displacement and velocity fields around the crack tip, as well as the boundary of the zone, are known. Based on the results of previous investigators on related problems, the energy balance for the cracks in the fictitious fracture plane could be solved. A step by step approach was followed. First, extension of a single crack under static loading was considered. Subsequent dynamic loading, influence of inertia effects on stress and displacement fields and finite geometry of the fictitious fracture plane were considered and introduced. This approach was described extensively in [118], a summary is given in the following sections.

3.2.2   Elliptical crack in Mode I

The roots of the currently developed crack model were formed by the work of N.F.Mott. Following the Griffith approach, Mott [68] was the first one who took the kinetic energy into account for crack growth. He considered a centrally located elliptical through crack in an infinitely large plate. The loading condition was Mode I. Mott used the static solutions for the stress and displacement fields. Furthermore, he assumed that the crack propagation velocity was independent of the crack size, i.e. $\delta \dot{a}/\delta a = 0$. With these assumptions, a simple expression was obtained for the crack tip velocity under a constant load. Expressing the load level in the critical crack size a_c, Mott derived the following expression.

$$\dot{a} = \sqrt{\frac{2\pi}{k}} \cdot \sqrt{\frac{E}{\rho}} \cdot \sqrt{\left(1 - \frac{a_c}{a}\right)} \qquad\qquad (3.15)$$

This result has been widely discussed in literature, e.g. Kanninen and Popelar [45]. The terminal velocity was expressed in the longitudinal wave velocity C_p and the unknown constant k. Mott introduced this constant to relate the characteristic length of the problem to the crack size. A lower limit approach by Roberts and Wells [81] led to $\sqrt{(2\pi/k)} = 0.38$. In 1972, an exact solution of the limit crack velocity was published by Freund [24] and appeared to equal the Rayleigh wave velocity ($C_r = 0.54$-0.64 C_p).

Mott's result was improved by Berry [6] and also by Dulany. By assuming the load to be somewhat larger than the critical load p_{cr}, the integrated energy balance could be solved without the assumption of $\delta \dot{a}/\delta a = 0$. In the limit case of a load equal to the critical load, the crack tip velocity is given by:

$$\dot{a} = \sqrt{\frac{2\pi}{k}} \cdot \sqrt{\frac{E}{\rho}} \cdot \left(1 - \frac{a_c}{a}\right) \qquad\qquad (3.16)$$

Note the absence of the square root on the crack size dependent term. Therefore, Berry's result shows a more moderate crack extension than the result given by Mott. With the simple quadratic equations for the crack tip velocity, as given above, a description can be derived for the crack extension process.

To model crack extension of the penny-shaped cracks in the fictitious fracture plane, a similar approach was followed, based on the integrated balance of energies. The main differences of the model finally developed with the approach of Mott and/or Berry are:

- the uniaxial tensile load was a function of time; a constant loading rate was considered;

- the energy exchange occurred at the surface of the considered area around the crack tip. Consequently, the solution for a static load at infinity or fixed grips could not be used anymore;

- the load p, crack size a and crack tip velocity à were all functions of time and mutually dependent parameters;

- the inertia effects on the stress and displacement fields were included;

- the finite geometry was taken into account.

First the result for a single crack and constant tensile load will be given under the assumption of static stress and displacement fields.

3.2.3   Penny-shaped crack in Mode I

In this section, a single penny-shaped crack will be considered. The geometry is depicted in Figure 3.9. Inertia effects on the stress and displacement fields are still ignored at this stage.

For a penny-shaped crack, with radius a, the stress distribution, displacement field and the energy balance can be described for the planes of symmetry perpendicular to the crack plane. In Figure 3.10 such a plane is depicted with the section of the volume in which the energy exchange occurs. The local parameters are given in cylindrical polar coordinates.

Beforehand, the exact boundary of the region, A(t), was not known. The magnitude of S was unknown but S might also be a function of θ. It appeared that all the energy terms could be calculated in case radius S was independent of θ, while the magnitude of S could be determined afterwards. It was decided to fulfil this condition and not to introduce a new unknown coefficient to characterize the dependency on θ.
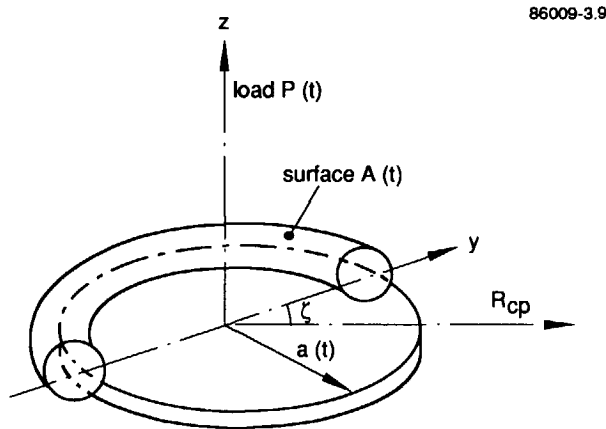
Figure 3.9   The penny-shaped crack and the considered volume around the crack tip.
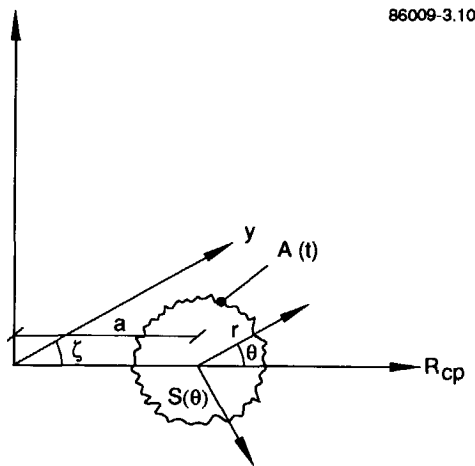
Figure 3.10   Section of torus and a plane of symmetry ($z = 0$) and definition of
local parameters in cylindrical polar coordinates.

The distance S is proportional to the characteristic length of the problem, denoted by
K. Initially, K is determined by the expression: $K = C_p \cdot (t-t_o)$, in which $t - t_o$ is the
time since crack growth initiation. The material outside this radius K cannot be aware
of crack growth. When K equals the radius of the crack, then the crack radius, a, is
considered as the characteristic length.

The energy terms were determined for this region using the static field solutions for the stress and the displacement fields under plane strain conditions.

The general form of the field equations is a Taylor series. In the model, the first term approximation was used.
The first term for the stress field is given by

$$\underline{\sigma} = \frac{2}{\pi} p(t) \sqrt{\left(\frac{a}{2r}\right)} \, \underline{l}_\sigma(\theta)$$

(3.17)

$$\underline{\sigma} = \begin{pmatrix} \sigma_r \\ \sigma_z \\ \sigma_{rz} \\ \sigma_\zeta \end{pmatrix}$$

in which the vector $\underline{l}_\sigma(\theta)$ characterizes the stress field around the crack tip.

Under plane strain condition, the displacement field is independent of ζ, with $u_\zeta = 0$, while the non-zero components u_r and u_z are functions of r and z only. The first term of the series is:

$$\underline{u} = \frac{4}{\pi}(1 + \upsilon) \frac{p(t)}{E} \sqrt{\frac{ar}{2}} \, \underline{l}_u(\theta)$$

(3.18)

$$\underline{u} = \begin{pmatrix} u_r \\ u_z \\ u_\zeta \end{pmatrix}$$

with $\underline{l}_u(\theta)$ the vector to describe the displacement field.

Note, that by using the first term of the series, the introduced error was not of the same order as in the stress field. Due to the integration the error in the displacement field is of the order $O(r/a)$ higher.

The velocity field was derived from the displacement field, as determined from the stress distribution under static loading. Assuming that this distribution was not affected by a time-dependent loading, the velocity field followed from the differential of the displacement field.

$$\underline{\dot{u}} = \frac{\delta \underline{u}}{\delta p} \cdot \dot{p} + \frac{\delta \underline{u}}{\delta a} \cdot \dot{a}$$

$$\underline{\dot{u}} = \frac{2(1 + \upsilon)}{\pi E} \cdot \underline{l}_u(\theta) \left\{ \dot{p} \sqrt{2\,ar} + p\,\dot{a} \sqrt{\frac{r}{2a}} \right\}$$

(3.19)

Using these relations, the various terms of the integrated energy balance could be calculated [118]. The balance is given by

$$E_v - W + E_k + E_d = E_o$$

(3.20)

in which E_0 is the energy content of the considered material volume at time t_0 at which time crack growth is initiated. The time t_0 was set to be zero.

The potential or deformation energy is given by

$$E_v(t) = \int_V \int_\varepsilon \sigma_{ij} \, d\varepsilon_{ij} \, dV \tag{3.21}$$

$$E_v(t) = \frac{(1 + v)}{E} \cdot CV_t \cdot p^2 \cdot a \tag{3.22}$$

with $\quad CV_t = (5aS + S^2) - 2v(4aS + S^2)$ which is the result of the volume integral.

In the considered situation, the external work W on the volume V was performed by surface forces only. Therefore, the expression for W is

$$W(t) = \int_A \int_u T_i \cdot du_i \cdot dA \tag{3.23}$$

in which T_i denotes the vector of the surface forces and u_i the displacement at the surface.

When the divergence theorem of Gauss was used and the surface integral was converted to a volume integral, substitution of the various terms led to the same result for static loading as given by (3.21). Direct calculation of (3.23) with the first term approximation of the Taylor series for the stress and displacement fields at the torus surface, however, led to slightly different results. Because the surface integral is most sensitive for the first term approximation, the result of the conversion was used in the model.

$$W(t) = \frac{2(1 + v)}{E} \cdot CV_t \int_t \left(p \, \dot{p} \, a + \frac{p^2 \dot{a}}{2} \right) d\tau \tag{3.24}$$

The kinetic energy follows from the integral

$$E_k(t) = \frac{1}{2}\rho \int_V (\dot{\underline{u}})^2 \, dV \tag{3.25}$$

$$E_k(t) = \frac{(1 + v)^2}{E^2} \cdot \rho \cdot CT_t \cdot \left(\dot{p}^2 a + p \, \dot{p} \, \dot{a} + \frac{p^2 \dot{a}^2}{4a} \right) \tag{3.26}$$

with $\quad CT_t = \left(\frac{38}{3} - 32v + \frac{64}{3} v^2 \right) a S^3 - (3 - 4v) S^4$

During the fracture process, new crack surfaces will be formed dissipating the specific surface energy γ.

$$E_d = 2\gamma \cdot \pi \, a^2(t) \tag{3.27}$$

In this expression, γ may be a function of the crack radius and/or the crack tip velocity.

Using the Griffith criterion [11, 23], the specific surface energy can be expressed in the load level p_0 at which the crack with radius a_b just becomes critical, and the strength and energy criteria are fulfilled.

$$2\gamma = \frac{4}{\pi E} \cdot \left(1 - v^2\right) a_b \cdot p_0^2 \tag{3.28}$$

The description of the extension of a crack, with initial radius a_b, under an increasing load $p(t)$, and crack initiation at $t = t_0$ followed from the substitution of the energy terms in the balance:

$$E_v(t) - W(t) + E_k(t) + E_d(t) = E_0$$

which resulted in the following equation

$$\frac{(1+v)}{E} \cdot CV_t \cdot p^2 a - \frac{(1+v)}{E} \cdot CV_t \left\{ p_0^2 a + p^2 a_b \right\} - \frac{2(1+v)}{E} \cdot CV_t \int_{t_0}^{t} \left(p \dot{p} a + \frac{p^2 \dot{a}}{2} \right) d\tau +$$

$$+ \frac{(1+v)^2}{E^2} \cdot \rho \cdot CT_t \left\{ \dot{p}^2 a + p \dot{p} \dot{a} + \frac{p^2 \dot{a}^2}{4 a} \right\} + \frac{4(1-v^2)}{E} \cdot a_b p_0^2 \cdot a^2 = E_0 \tag{3.29}$$

$$E_0 = \frac{(1+v)}{E} \left\{ -CV_0 \, p_0^2 \, a_b + \frac{(1+v)}{E} \rho \, CT_0 \, \dot{p}_0^2 \, a_b \right\} + 2\gamma \pi a_b^2 \tag{3.30}$$

Three aspects were not included or determined in the balance so far, i.e.

- the geometry of the fictitious fracture plane;

- the inertia effects on stress and displacement fields;

- the size of the considered zone.

These aspects will be discussed in the following sections, but first the obtained result will be applied to describe crack extension under static loading which enables a comparison with the solutions given in literature.

3.2.4 Balance of energies for static loading

For static loading, the balance reduces to a quadratic equation which can be solved analytically. According to the Berry's result, one parameter is unknown, i.e. the size of the considered zone, S. This size is proportional to the characteristic length.

$$S \quad = \quad \lambda \cdot K \tag{3.31}$$

The factor λ, however, can be determined using the exact solutions given in literature for the Griffith criterion in static Mode I, setting the characteristic length equal to the crack radius a.

Sneddon [97] reported the available energy, $W - E_v$, due to the existence of a penny-shaped crack. Using the derived expression for the energy terms (3.21 and 3.24), the constant λ can be expressed in terms of Poisson's ratio.

$$(5\lambda + \lambda^2) - 2\upsilon(4\lambda + \lambda^2) = \frac{8}{3} (1-\upsilon) \tag{3.32}$$

Substitution in the energy balance resulted [114] in the expression:

$$\dot{a}^2 \quad = \quad C_p^2 \, \frac{(1 - 2\upsilon)}{CCT} \cdot \frac{16}{3} \cdot \left\{ 2 - 3 \left(\frac{a_b}{a}\right) + \left(\frac{a_b}{a}\right)^3 \right\} \tag{3.33}$$

$$\text{with} \quad CCT \quad = \quad \left(\frac{38}{3} - 32\upsilon + \frac{64}{3} \upsilon^2 \right) \lambda^3 - (3 - 4\upsilon) \, \lambda^4$$

The result is depicted for υ is 0.25 ($\lambda = 0.529$) in Figure 3.11. It shows that during the crack propagation, a stationary equilibrium is reached between the released and dissipated energy. The terminal velocity equals about four times the theoretical limit of the Rayleigh wave velocity.

The application of this approach for an elliptical through-crack in an infinitely large plate led to the same result as reported by Berry.
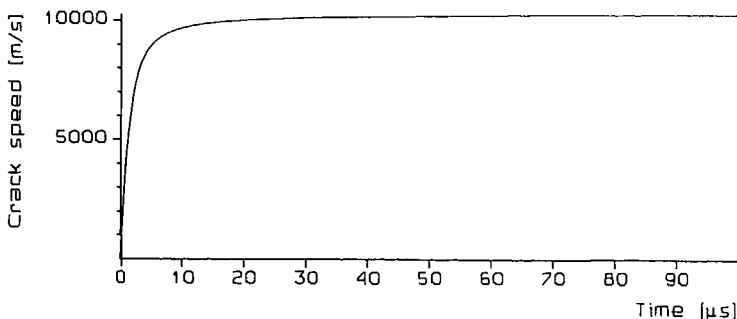
Figure 3.11   Crack tip velocity versus time for $\upsilon = 0.25$

Note that at crack initiation the size of the zone, that should be considered, rapidly grows and so too does the characteristic length. In case the characteristic length differs from the crack radius and varies in time, no analytical solution can be obtained. In [114] the aspect of the characteristic length at crack growth initiation was discussed using the program developed to solve the energy balance numerically. It appeared that ignoring this initial dependence of the characteristic length results in an underestimate of the initial crack acceleration. In most cases however, the introduced error in the description of the fracture process is negligible.

3.2.5   Influence of loading rate in quasi-static approach

It is interesting to examine the crack extension under dynamic loading before the inertia effects on stress and displacement fields are included in the balance. Figure 3.12 shows the result for various, constant loading rates. It emerges that for increasing loading rates, the maximum as well as the terminal velocity decrease. Apparently, the energy supply of the external work, which is transmitted to the considered region
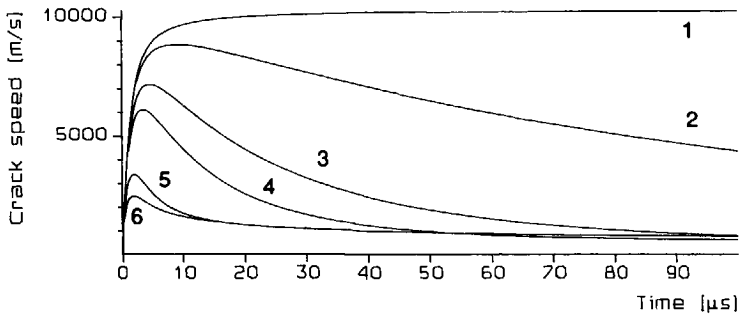
Figure 3.12   Influence of loading rate, $\dot{p}$, on crack growth in quasi-static approach. Lines 1-6 represent $\dot{p} = 10^{-2}$, 10^{+4}, 5.10^{+4}, 10^{+5}, 5.10^{+5}, 10^{+6} [MPa/s].

around the crack tip, becomes less effective for the fracture process. This corresponds with a decrease of the stress intensity factor at higher loading rates. Or in other words, the stress distribution around the crack tip becomes more moderate and consequently the crack driving force decreases.

The various energy terms in the balance have been compared. From this comparison, it emerged that the kinetic energy term, related to the other terms, becomes more dominant with increasing loading rate.

3.2.6　　Influence of finite size

The stress intensity factor is influenced by the finite size of the considered specimen and by crack geometry. According to the author's knowledge, no solution is available to characterize this influence as a function of crack diameter and intermediate crack distance for the geometry present in the fictitious fracture plane. The solutions for collinear cracks in an infinite plate are well known and given by Isida [38] and Irwin [37]. In [112], the solutions were compared and approximated for the fictitious plane by the function f(a/b).

$$f\left(\frac{a}{b}\right) = 1 + 0.5\left(\frac{a}{b}\right)^2 + 0.21\left(\frac{a}{b}\right)^4 + 1.74\left(\frac{a}{b}\right)^6 \tag{3.34}$$

Comparison of the function proposed by Irwin with the work of Nozaki, et al. [71] for a single penny-shaped crack in a cylinder with finite radius, showed a similar dependence on the ratio of the crack size and the cylinder diameter. It was decided to adjust the stress intensity factor in the fictitious plane with the function f(a/b):

$$K_I\left(\frac{a}{b}\right) = f\left(\frac{a}{b}\right) \cdot K_I$$

In [114], the influence of the finite geometry on the stress and displacement fields was determined which resulted in the following, adjusted expressions for the energy terms:

$$W(t) = 2\frac{(1+\upsilon)}{E} \cdot CV_t \int_t \left(p\,\dot{p}\,a\,f^2 + \frac{1}{2}p^2\,\dot{a}\,(f^2 + f.g)\right)d\tau \tag{3.35}$$

$$E_v(t) = \frac{(1+\upsilon)}{E} \cdot CV_t \cdot p^2\,f^2\,a \tag{3.36}$$

$$E_k(t) = \frac{(1+\upsilon)^2}{E^2} \cdot \rho \cdot CT_t \left\{ a\,\dot{p}^2\,f^2 + p\,\dot{p}\,\dot{a}\,(f^2 + f.g) + \frac{p^2}{4a} \cdot \dot{a}^2\,(f+g)^2 \right\} \tag{3.37}$$

The function $g\left(\dfrac{a}{b}\right) = 2 \cdot a \cdot \dfrac{d}{da}\left\{f\left(\dfrac{a}{b}\right)\right\}$

Following the Griffith approach, the adjusted energy terms resulted in an expression for the specific surface energy in terms of the geometry and load level as given in (3.38), see also (3.28).

$$2 \cdot \gamma = \frac{(1+\upsilon)}{E} \cdot \frac{CV_o\,P_o^2}{2\pi\,a_b} \cdot \left(2\,h_o + f_o^2 + f_o \cdot g_o\right) \tag{3.38}$$

In this expression, h(a/b) equals:

$$h\left(\frac{a}{b}\right) = \frac{1}{a} \int_a (f^2 + f \cdot g) \, da$$

To illustrate the influence of the geometry on the crack extension process, the calculation of the former section was repeated for ratios of initial crack radius a_b and the maximum crack radius b, of 0.6 and 0.4. The results are depicted in Figure 3.13.

Comparison of the results of Figures 3.12 and 3.13 shows that for decreasing intermediate distance, the influence of the loading rate on the crack extension decreases. Apparently, the stress distribution and amplitude are dominated by the finite dimensions, so the influence of dynamics decreases. The same conclusions emerged from Nozaki's work, see section 3.2.7.

a. Initial ratio $a_b/b = 0.6$
b. Initial ratio $a_b/b = 0.4$
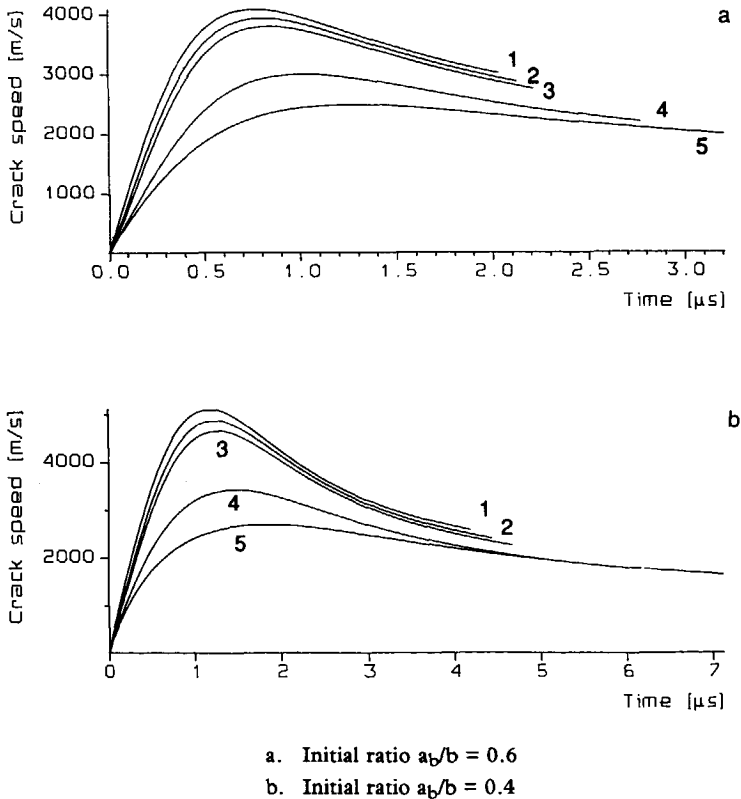
Figure 3.13 Influence of loading rate, $\dot{p}$, on crack growth in bounded geometry, with $\gamma = 1$ [N/m]. Lines 1-5 represent $\dot{p} = 10^{-2}$, 5.10^{+4}, 10^{+5}, 5.10^{+5}, 10^{+6} [MPa/s] respectively.

As an illustration of the coupled dependency of the energy terms in the balance, Figure 3.14 shows the result of the calculation for $a_b/b = 0.4$, similar to Figure 3.13b, but with a ten-fold specific surface energy, γ.
It appears that the fracture energy term also remains important for high loading rates and, consequently, the rate effect on crack extension decreases. In advance of the application to concrete, it can be concluded that the rate sensitivity will increase for decreasing fracture energy and thus decreasing material quality.
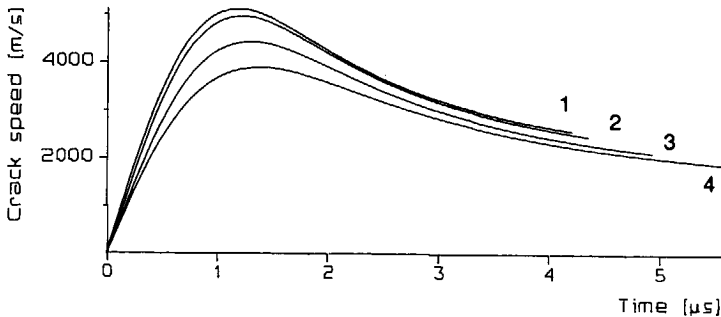
Figure 3.14   Influence of loading rate, $\dot{p}$, on crack growth in bounded geometry, $\gamma = 10$ [N/m], for the quasi-static approach. Lines 1-4 represent $\dot{p} = 10^{-2}$, 10^{+5}, 5.10^{+5}, 10^{+6} [MPa/s] respectively.

3.2.7   Incorporation of inertia effects.

To derive the various energy terms for dynamic loading, or at high crack tip velocities, the equations of motion should be used instead of the described quasi-static approach. As the application of the equations of motion complicates the solution of the energy balance significantly, it was decided to use results from literature and approximate the influence of inertia on the equilibrium of forces.

In 1972 Freund published his study [24, 25, 26 and 27] on dynamic effects around the tip of a semi infinite, plane crack in an unbounded medium loaded by a longitudinal tensile wave. The main result was that the dynamic stress intensity factor, K_{Id}, could be derived by multiplying the static factor, K_{Is} by a function which only depends on the crack tip velocity, $k(\dot{a})$. This function equals one for $\dot{a}$ equals zero and decreases to zero for crack extension at the limiting velocity of the Rayleigh wave (C_r). Comparable functions were derived for crack extension at constant velocity by Broberg [10] and Baker [5]. Achenbach [1] and Atkinson & Shelby [4] proved that other geometries also have C_r or the shear wave velocity as the limiting velocity for crack extension. See also the work of Tsai [106], who derived the exact stress distribution around a penny-shaped crack.

This result can be explained as follows. For any crack geometry, K_I will decrease with increasing crack tip velocity because inertia components become more important. A lower K_I value diminishes the energy flux into the fracture zone and consequently a lower crack tip velocity is established. Any crack geometry must have a terminal velocity of crack extension with a stable equilibrium between the energy flux into the fracture zone and the energy release rate. When the velocity reaches C_r, K_I must be zero because at this velocity the material around the newly formed crack surfaces cannot respond to the actual crack size and the equilibrium is established by inertia forces.

From these results it was concluded that the static field equations are applicable when the stress intensity factor is adjusted using a function $k(\dot{a})$ as derived by Freund.
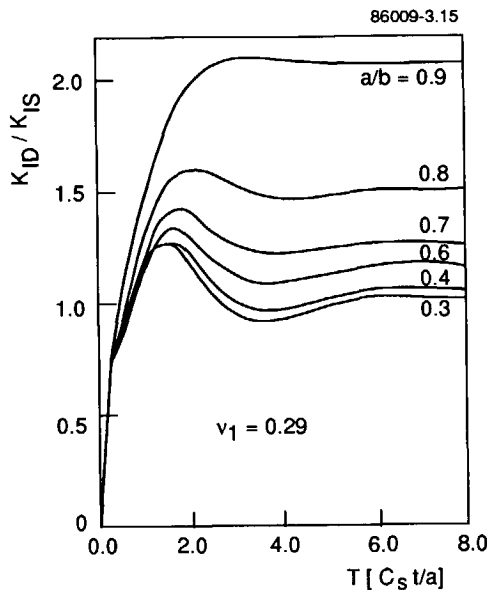
Figure 3.15 Dynamic stress intensity factor versus time for various crack and cylinder ratios [71].

Another aspect that had to be considered was the effect of finite dimensions under dynamic loading. Literature presents solutions for stress waves impinging on stationary cracks, e.g. [90 and 71]. The aspects of finite crack size and geometrical boundaries, present in the fictitious fracture plane, were studied by Nozaki [71]. Some results are depicted in Figure 3.15.

When single or multiple cracks are loaded by an impinging (step)load, a process of rarefaction and refraction occurs before a stationary situation is reached. The elapsed time interval depends on crack size, boundary distance and the shear, or Rayleigh wave

velocity. Figure 3.15 shows that, for all geometries, the stationary situation was reached at about the same time. The strength of the foregoing oscillation decreased for decreasing cylinder radius. The terminal stress intensity factor corresponds with the static solution for finite geometries as given in 3.2.6. Therefore, application of the static field equations for impinging stress waves yields temporary errors. The magnitude of the introduced error diminishes with decreasing intermediate distance and increasing fracture time.

The objective of the model is to characterize the crack extension and energy dissipation in the pre-peak fracture process as simply as possible rather than to give an exact description. Based on this objective and the crack extension features mentioned above, it was decided to apply the static field equations of LEFM. The temporary mismatch introduced owing to this, is disregarded. The static fields are adjusted by a function k(ȧ), similar to the function derived by Freund and Broberg, to take the inertia effects into account.

The applied function is

$$k(\dot{a}) = \frac{\left(1 - \dfrac{\dot{a}}{C_r}\right)}{\sqrt{1 - \left(\dfrac{\dot{a}}{C_p}\right)}} \tag{3.39}$$

Using this method, relatively simple expressions for the various energy terms were obtained and the dependency of the rate sensitivity on the various model parameters could be examined.
The applicability of the adjusted static stress fields also emerged from Mall and Kobayashi's research on the dynamic fracture of notched bend specimen [60].

3.2.8   Influence of loading rate on crack propagation

In Figure 3.12, the effect of the loading rate on crack extension was depicted, following the quasi-static approach. Adjustment using the function k(ȧ) led to the features given in Figure 3.16.

It emerges that the terminal velocity at low loading rates for a single crack equals C_r, as it should be, but that the terminal velocity decreases with increasing loading rate. On the other hand, the initial acceleration of the crack tip increases with increasing loading rate. The latter feature was not observed in the quasi-static approach, but is reasonable considering the potential energy available for crack growth. Concerning the feature of the decreasing terminal velocity, there is no essential difference. The analysis of the energy terms showed that the kinetic and deformation energy, normalized by the external work, increased significantly with increasing loading rate. As was mentioned

for the static approach, the rate of energy supply becomes too high to be absorbed in the fracture process. An equilibrium is established in which a major part of the supplied energy is stored in kinetic and deformation energy. This should mean that the stress intensity factor diminishes at higher loading rates due to the contribution of inertia to the equilibrium of forces. This is the same result as Curbach obtained from his FE calculations on a notched specimen [17].
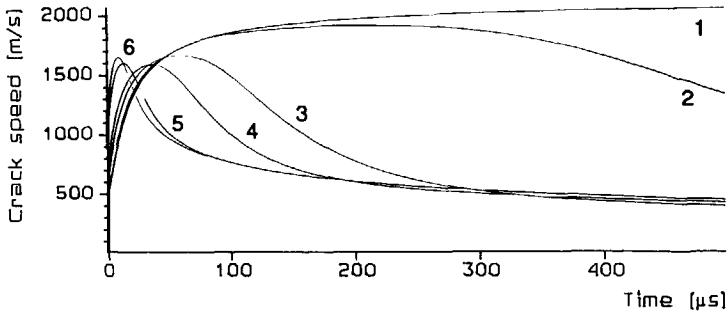
Figure 3.16 Influence of loading rate, $\dot{p}$, on crack growth; $\gamma = 1$ [N/m]; $C_r = 2050$ [m/s]. Lines 1-6 represent $\dot{p} = 10^{-2}$, 10^{+4}, 5.10^{+4}, 10^{+5}, 5.10^{+5}, 10^{+6} [MPa/s] respectively.

It is concluded that the degree of stress singularity at the crack tip decreases with increasing loading rate, resulting in a lower crack extension rate.
Beside the results of Curbach, the work of Chen [14] supports the features given by the model. Chen presented a damage model to describe the dynamic fracture process in concrete. The damage rate calculated, which is directly related to the crack tip velocity, showed a decreasing terminal value at increasing strain rate. Also the time scale of fracture corresponded with the scale of the currently described model.

In the quasi-static approach it was observed that the influence of the loading rate on crack propagation decreases when the specific surface energy or the a_b/b ratio increases. The same feature was observed in the modified approach, see [118].

In conclusion: the approach presented in the model currently described, gives a prediction of crack growth which reflects the influence of crack geometry and rate dependency of the fracture process. Because of the lack of comparable results in literature, a final statement about the accuracy of the quantitative results cannot be made.
The model will be used to predict the rate dependency of concrete strength by relating the results at high loading rates with the results obtained at static loading conditions. The predicted dependency is expected to be quite accurate due to the relative use of the results.

3.2.9   Crack model in the fictitious fracture plane

The fictitious fracture plane was described in the sections of 3.1. To handle the crack extension in this plane, a program was developed to numerically solve the balance of energies. A description of the program is given in [118].

The fracture process in concrete is delayed by the presence of many energy barriers. Crack arrest is not modelled in the fictitious fracture plane, where only two energy barriers are present as two co-centrical zones around the initial cracks. Figure 3.17 shows the crack extension in the fictitious fracture plane and the influence of the energy barrier at the transition from bond to mortar fracture at four different loading rates for the high quality concrete. The parameters of the fictitious fracture plane were given in 3.1.4.
One of the disadvantages of the model is the need for data on the specific surface energies for bond, matrix and aggregate fracture. More data is available on the mean value present in K_{Ic}. Note that these data may be affected by the size of the specimen, width of the fracture zone and test method.
When, in the schematization a single region around the initial flaws is considered, with the mean value of the surface energies, for the high quality concrete crack extension occurs as depicted in Figure 3.18 for three loading rates.
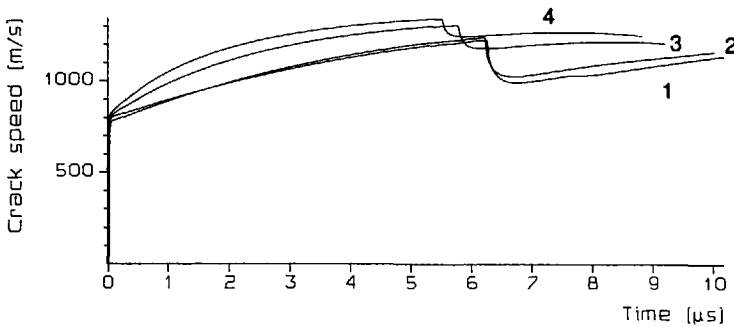
Figure 3.17   Crack extension for the tested A quality concrete, schematized with two zones. Lines 1-4 represent $\dot{p} = 10^3$, 5.10^4, 5.10^{+5} and 10^{+6} [MPa/s].

The results in Figure 3.17 show that the effect of the energy barrier on the fracture process decreases with increasing loading rate. The stored and available energy in the zone around the crack tip becomes sufficient to fulfil the extra energy demand almost immediately.

Comparison of the results in Figure 3.17 and 3.18 shows that the presence of an energy barrier delays the fracture process and the influence of loading rate is more

pronounced. For either the fictitious fracture plane with one or two zones, the modelled fracture process appears to be a function of time and loading rate.
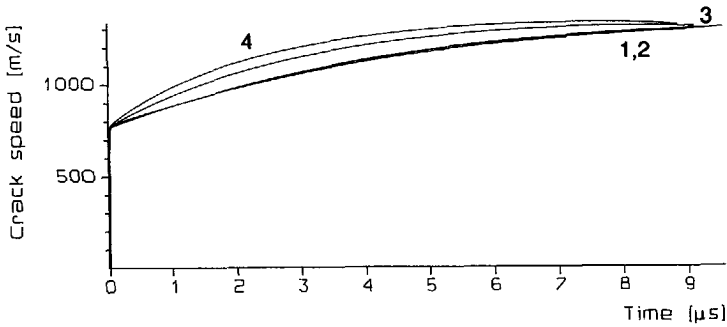
Figure 3.18 Crack extension for the tested A-quality concrete, schematized with a single zone.

In the model, the maximum strength is reached when the crack radii are extended to b. By modelling the real fracture process to crack extension in the fictitious plane, the processes of crack arrest and crack branching were not incorporated. Consequently, no absolute values for the average crack velocity in the real material can be obtained. The
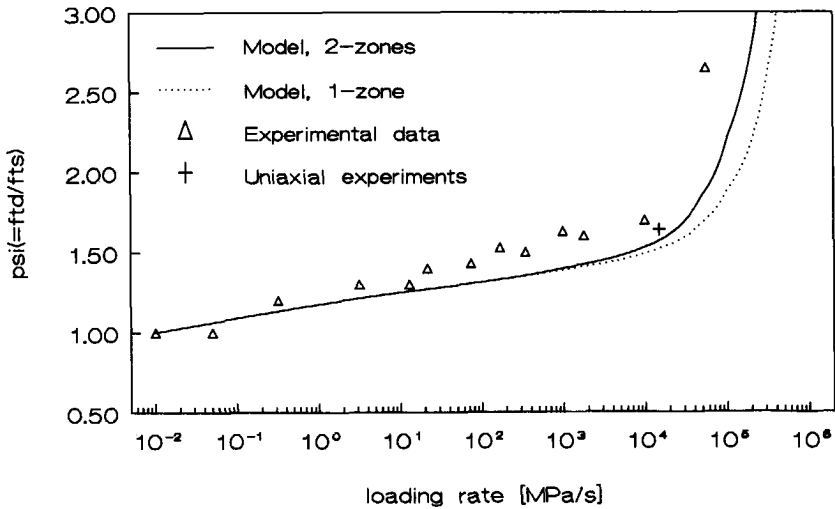
Figure 3.19 The rate effect for one and two fracture zones.

time-scale of the fracture process in the model differs from that of the real material. Nevertheless, the rate effect on the real fracture process can be studied by using the modelled fracture process under static loading as a reference. The time to failure at static load and the corresponding load level are taken as a reference for the strength.

In this approach, the rate effect is governed by the fracture process in the fictitious plane. Therefore the presence of energy barriers, the geometry of the plane and the values of the fracture energies, which all affect the duration of the modelled fracture process, influence the rate dependency of the strength directly.
To illustrate this aspect, the rate effect was calculated for the high quality concrete schematized with one and two zones. The crack extension as presented in Figures 3.17 and 3.18, results in the predicted rate effect on strength as given in Figure 3.19. In this figure, experimental data from literature and the uniaxial experiments of the current programme are also depicted.

3.2.10   Model predicted rate effect

In the former section, the rate effect on the strength was presented using the scheme of the fictitious fracture plane and the crack extension model. Figure 3.19 showed the capability of the model to predict the rate effect under uniaxial tension. In this section the regions of moderate and steep strength increase will be discussed in more detail.

Under the assumption of constant surface or fracture energy, application of the model on both concrete qualities tested results in plots depicted in Figure 3.20 and denoted with gam = c. As in Figure 3.19, some experimental data from literature are also given. The lines show that the model reflects the strength increase for high loading rates very well and also the more sensitive response for lower concrete quality.
From these results it must be concluded that the steep strength increase for high loading rates is not caused by an increase of the fracture energy due to a different fracture path or multiple cracking, but by a changing stress and energy distribution in the regions around the crack tip. Consequently, the moderate strength increase at lower loading rates must be attributed to the changing fracture energy demand, which had to be included in the model to cover the whole range of loading rates.

The moderate strength increase is observed for all kind of materials, and various phenomena may contribute to this feature. The rate theory, which gives a general base for time-dependent fracture, shows that the strength of a material will increase with increasing loading rate, see Krausz & Krausz [54]. For concrete, the rate theory was applied by Mihashi and Wittmann [63] and Körmeling [48]. In addition to this phenomenon, the different geometry of the fracture planes and multiple fracture are important for dynamic concrete response. Zielinski [124] studied these phenomena. He concluded that for increasing loading rates, the fracture plane tends from bond fracture to aggregate fracture (ξ_c increases) and that multiple fracture becomes more

and more important. Note that there is still controversy about the loading rate at which multiple fracture becomes significant.
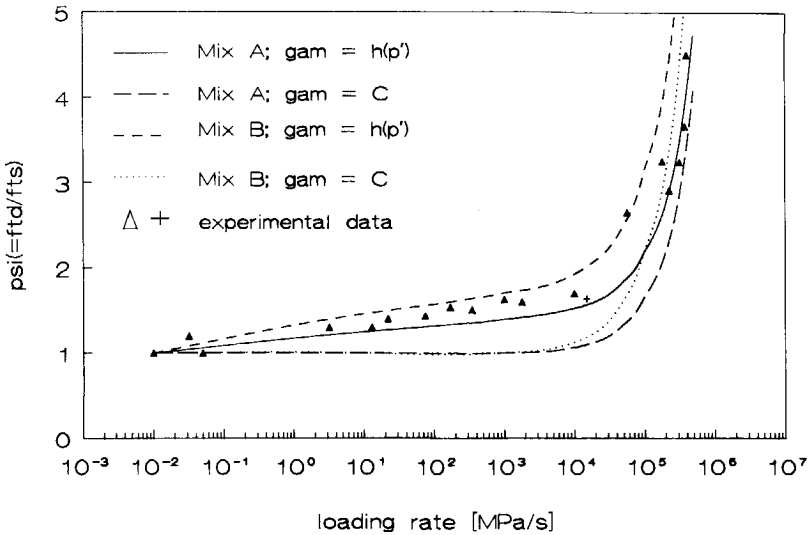
Figure 3.20   Predicted rate effect for the high and low quality concrete, with and without rate-dependent fracture energy.

The mechanism causing the moderate strength increase, or the changing fracture plane, is not a part of this study. It might be inertia effects changing the geometry of the fracture plane and causing multiple fracture, or the water contents in the pores might form the base for the mechanism, as Rossi concluded from his research [80].
Nevertheless, the observed change in geometry is represented as a changing energy demand in the model.

The rate dependency of the fracture energy was incorporated as follows:
Under static loading, the fracture plane was schematized under the condition of no aggregate fracture. At a loading rate of 1000 GPa/s, no bond cracking was assumed to occur, so the fracture plane was formed by aggregate and mortar fracture. In the intermediate range of loading rates, a logarithmic dependency was assumed between the two extreme fracture geometries.
From the results depicted in Figure 3.20, it emerges that this approach leads to the prediction of the dynamic strength that corresponds well with experimental data for all loading rates. The effect of the concrete's quality is also represented for the lower rates.

The observation on the changing mechanism at high loading rates has also consequences for the prediction of the rate effect on the fracture energy in the softening

process. Commonly the rate effect on G_f is coupled to the dynamic strength. When the dynamic strength increase is based on a changing energy demand in the pre-peak fracture process, it seems to be reasonable to assume a similar effect on the post-peak fracture process. However, at high loading rates, the strength increase is not coupled to a changing energy demand but to mechanical response. Therefore, it is not correct to couple rate effects on strength to G_f at high loading rates. At this stage no well-founded alternative can be given for the rate effect on G_f, because too little is known about the width of the fracture zone and the amount of micro-cracking under dynamic loading. Further attention will be paid to this subject in Chapter 6 when the uniaxial impact tests are discussed.

3.3   Concluding remarks on the uniaxial tensile model

The pre-peak fracture process under tensile loading can be described by means of crack extension in a fictitious fracture plane. The geometry of this plane emerges from material composition, material properties under static loading and the crack growth criteria from LEFM, as described in the first part of this chapter. Changes in material properties are reflected satisfactorily in the model.

The modelled fracture process under static loading conditions forms the reference to study the rate effect on tensile strength. Regarding the rate dependency in the model, it can be concluded that the moderate and steep increase of concrete tensile strength for low and high loading rates, respectively, are caused by two different phenomena.
For loading rates up to about 10 GPa/s, the strength increase is mainly caused by two effects. First it follows from rate theory and, secondly, the geometry of the fracture plane changes, aggregate fracture occurs. The extension mechanism of the existing damage does not change for these loading rates and the dependency can be expressed in a power function with one single coefficient.
The steep increase beyond 10 GPa/s is caused by a mechanical response of the material around the crack tips in which the inertia effects become dominant. The partition of the supplied energy over the various energy terms changes, K_{Id} decreases, causing a decreasing crack propagation velocity resulting in a strength increase.

Because the strength increase at high loading rates is not coupled to a changing fracture energy, it is not correct to predict the rate effect on the fracture energy in the softening process, G_f, by means of the dependency of tensile strength for these loading rates.

Finally, in spite of the assumptions and simplifications, the model describes the rate dependency of the uniaxial tensile strength well, for all loading rates, and also reflects the rate sensitivity for different concrete qualities. Apparently, the most important aspects of the material response of concrete under dynamic loading, before maximum strength, can be characterized by the extension of the existing damage in the fictitious fracture plane.

This implies that the model can be used to study the influence of material properties and composition on the rate dependency of the tensile strength, and also the effect of changing initial conditions due to static lateral compression.

4   MODEL FOR BIAXIAL LOADING

The uniaxial model illustrated that rate effect on strength is governed by the rate effect on damage extension which can be represented by crack extension in a fictitious fracture plane. In the biaxial loading condition of the research programme, the static, lateral compressive load changes the level of initial damage and internal stresses. Related to the uniaxial loading, the lateral compression just changes the initial conditions for the subsequent axial tensile load. Therefore, it was decided to examine the possibilities of extending the uniaxial model to describe the dynamic, residual tensile strength as a function of lateral static compression.
Because it was a first examination, a simple but nevertheless effective description of concrete features was used.

The idea was to translate initial damage level and internal stresses, which occur due to lateral compression, to an equivalent initial condition for axial tensile loading.
The validity of the transcription was judged by a comparison with the static failure envelope. The correspondence appeared to be reasonable and the crack extension model was applied to predict the rate effect on the residual tensile strength as a function of the level of lateral compression.

4.1   Modelling approach

To derive a relation between the damage development under tensile and compressive loading, the local internal stresses and damage had to be related. Because the major part of the compressive loading range is coupled to bond failure, 0.3 - 0.8 f_c, the attention was focused on describing the damage and local stress level at the aggregate-mortar interface.

Referring to the derivation of the schemes of the fictitious fracture planes, section 3.1.2 and 3.1.3, the following approach was developed.

- The damage development was thought to be initiated from initial defects on the aggregate-mortar interfaces.

- It was assumed that each aggregate has a single defect with random orientation.

External loading causes local stresses around the defect which depend on the specific orientation of that defect as well as on the loading condition.

- A relation had to be derived between the external loading and the local stresses at the location of the defect.

- In combination with a local failure criterion, the critical load for the defect emerges from the local stress distribution.

- After a defect is initiated, bond failure will occur as far as the internal stress state permits.

- When the critical load is known for each defect, a relation can be obtained between the percentage of activated defects and load levels for different loading conditions.

Using the uniaxial tensile loading condition as a reference, the initial damage level given by the number of activated cracks under compression can be related to an equivalent tensile condition.

To realize this approach, the first step was to derive the relation between load and activated defect. Two simple options emerge from literature to characterize a (heterogeneous) material with initial defects.

In the first option the heterogeneity is presented by randomly distributed cracks in a linear elastic, homogeneous matrix. Considering an isolated crack, application of LEFM gives the critical load level for uniaxial and biaxial loading conditions.
Griffith also applied his theory to compressive and multi-axial loading conditions. He derived the failure envelope [55, 73]:

$$\sigma_t = f_t \qquad \text{if} \qquad 3\,\sigma_t + \sigma_c \geq 0$$

$$(\sigma_t - \sigma_c)^2 + 8\,f_t(\sigma_t + \sigma_c) = 0 \qquad \text{if} \qquad 3\,\sigma_t + \sigma_c \leq 0 \tag{4.1}$$

and the critical orientation angle, φ_{cr}, related to the σ_c-axis:

$$\cos 2\,\varphi_{cr} = -\frac{1}{2}\,\frac{\sigma_t - \sigma_c}{\sigma_t + \sigma_c}$$

One obvious shortcoming of this result is the constant ratio of compressive and tensile strength, i.e. 8. However, this failure envelope qualitatively presents the same feature as the Mohr-Coulomb criterion with tension cut-off. Both types of failure envelopes are depicted in Figure 4.1.

To apply this Griffith approach to concrete and cope with the constraint of fixed strength ratio, various modifications were suggested in literature. Coefficients were introduced to adjust the effectiveness of the load directions to the heterogeneous material behaviour, see [30, 55].
The given failure envelope, however, only provides the critical load condition for the initiation of the most critical cracks. Macroscopic failure will only occur when these most vulnerable cracks are self-propagating and lead to final failure. When crack arrest occurs, other defects have to be activated before final failure takes place.
Paul [73] followed the Griffith approach and determined the sequence of crack initiation as a function of crack orientation, load level and load condition. Sih [89] introduced the "Strain energy density vector" to derive a criterion between the loading

and activated cracks. Both approaches result in successive failure loci which are coupled to a specific orientation of the initial cracks.
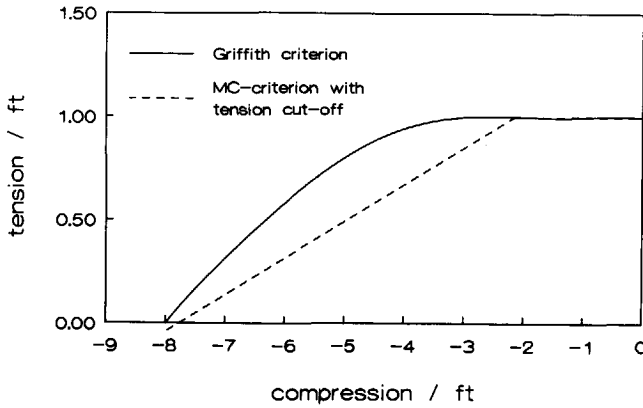
Figure 4.1   The Griffith and Mohr-Coulomb failure envelopes.

The coupling of these loci to the bond failure process in concrete have been examined. It appeared that the coupling demands the introduction of three coefficients at least, to relate the damage development in the homogeneous material to the damage extension in concrete. The limitations of this option especially emerged from the response under compression. The effect of the local stress distribution around the stiff aggregates had to be implemented artificially.

Considering this result, it was concluded that the coupling of damage development in concrete under tension and compression by means of randomly oriented cracks in a homogeneous material, results in a rather artificial presentation of the real material behaviour of concrete.

The second option bends to the presence of inclusions with a different stiffness than the matrix material.
The most simple approach is to consider a single circular, LE inclusion in an LE matrix material. Analytical solutions are available for the local stress distribution with and without bond defects [7, 69, 74 and 98]. These solutions offer the opportunity to study the influence of load condition and defect orientation on the local stresses, based on the different stiffness properties of mortar and aggregate.
The interaction effect between inclusions was reported in literature by Stroeven [98] amongst others, but was not quantified in the current programme.

This approach appeared to deal with the most dominant aspects of the failure mechanism and led to rather good results. The approach and the results of this option are given in next sections.

4.2   Induced internal stresses

Muskhelishvili [69] reports on the stress distribution around circular inclusions as a function of Young's modulus and Poisson's ratio. Expressed in the radial, tangential and shear stresses, the stress distribution at the interface is given respectively by:

$$\sigma_r = \sigma \{ 1 - \tau + [1 - 2\beta - 3\delta] \cos 2\alpha \}$$

$$\sigma_{tan} = \sigma \{ 1 + \tau - [1 - 3\delta] \cos 2\alpha \} \qquad\qquad (4.2)$$

$$\sigma_{rt} = \sigma \{ [1 + \beta + 3\delta] \sin 2\alpha \}$$

in which σ denotes the external load level and α the angle with the load direction. The coefficients β, τ and δ depend on the elastic material properties. Table 4.1 presents the figures for a composition of granite included in mortar, reported by Zielinski [124], and the high and low quality concrete of the current programme.

Table 4.1 The coefficients β, τ and δ for three compositions.

	Granite/Mortar	Mix A	Mix B
E_i/E *	2.6	4.4	7.7
υ_i/υ *	1.2	1.0	1.0
β	- 0.46	- 0.63	- 0.75
τ	- 0.32	- 0.41	- 0.48
δ	+ 0.23	+ 0.32	+ 0.37

*   subscript "$_i$" denotes the property of the inclusion.

The results of Muskhelishvili are widely used and discussed in literature. Here just two features of the stress distribution are mentioned, i.e. the stress level as well as the stress gradients along the surface increase with increasing difference in material properties. For the prediction of the bond failure development in both concrete mixes, this implies that in the low quality concrete, bond failure starts at a lower load level but is less sensitive for load increase.

Because of linearity, the stress distribution can be determined for all biaxial loading conditions. For the properties of the A quality concrete the stress distribution under a uniaxial and a biaxial loading condition is depicted in Figure 4.2.
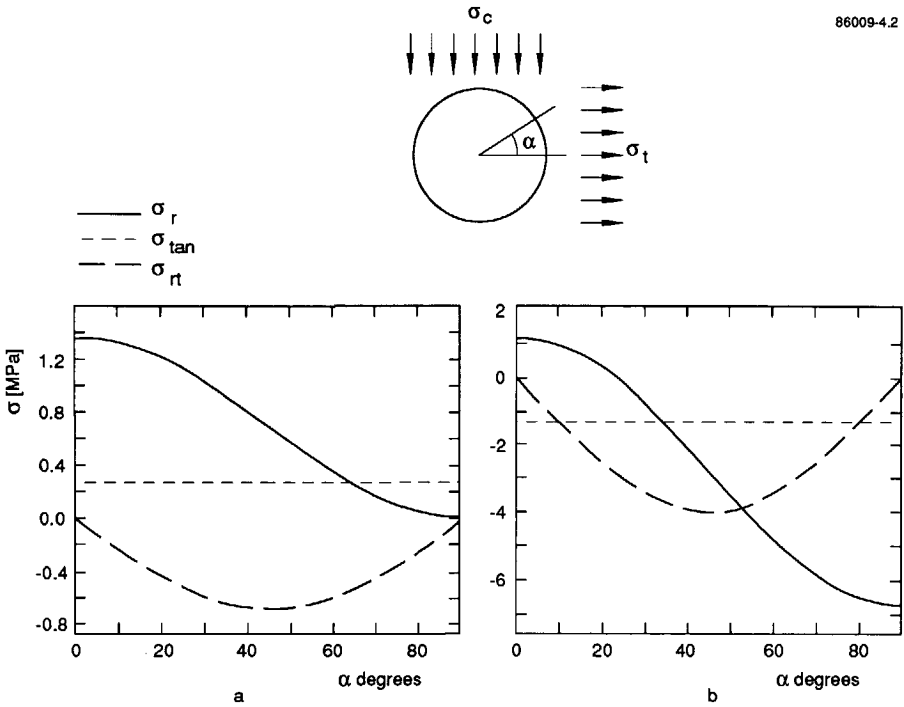
a) Loading: $\alpha = 0° + 1$ [MPa] $\alpha = 90°$ 0 [MPa]
b) Loading: $\alpha = 0° + 1$ [MPa] $\alpha = 90°$ -5 [MPa]

Figure 4.2   The stress distribution at the interface of a circular inclusion under uniaxial tension and biaxial, tensile-compressive loading. Elastic properties of high-quality concrete (Mix A).

As an extension of the work of Muskhelishvili [69], Perlman and Sih [74] studied the influence of partly debonded inclusions. They presented analytical solutions for the stress distribution. In Figure 4.3 some of their results are given. Considering small defects at the aggregate interface, the work of Perlman and Sih shows that these defects will have minor influence on the stress distribution. This result enabled us to use the stress distribution at perfect bond as the parameter to be coupled to a local failure criterion. This combination should give the wanted sequence in activated defects as mentioned in the outline of the model approach.
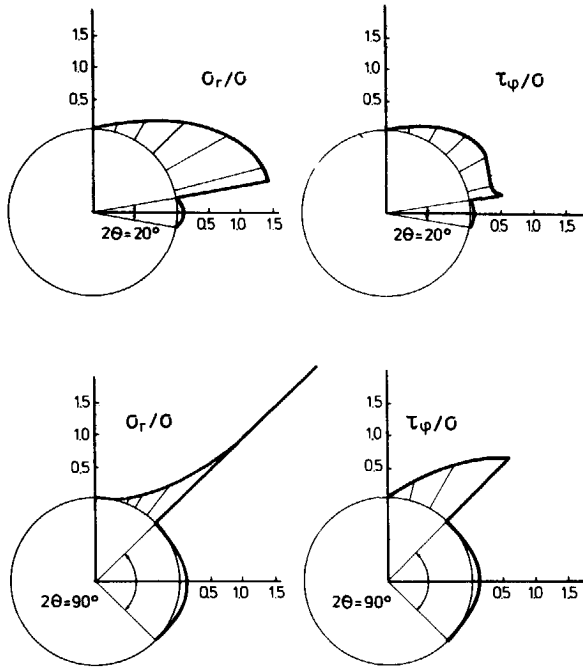
Figure 4.3   Stress distribution at interface of partly debonded inclusion with τ_φ the shear stress σ_{rt} [124].

4.3   Local failure criterion

The next step in the modelling process is the choice of a proper local failure criterion. Considering the positive radial and principal stresses at the interface under uniaxial tensile loading, the most obvious local failure criterion is the maximum tensile stress criterion, which is also used to describe the failure envelope of concrete under tension and low compressive loading. The stress distribution under compression shows mainly compressive radial and tangential stresses at the interface. The shear stresses result in a region of tensile principal stresses outside the compressive cones. Research has shown that the shear stresses govern the bond failure process [12, 98 and 104] and, therefore, should be present in the failure criterion. The Mohr-Coulomb criterion offers this feature and was proposed by Taylor and Broms [104] to describe the failure process at the interface.

Following the overall behaviour of concrete and the work on the local stresses and failure mode, the Mohr-Coulomb criterion with tension cutoff was adopted as the local failure criterion for model description.

The outline of the procedure to derive the local failure criterion was as follows.

-   Perfect bond was assumed and the stress distribution at the inclusion interface was determined for uniaxial tension and compression using equations (4.2).

-   Initiation of bond failure occurs at load levels f_{cb} and f_{tb}. At these levels Mohr's circles were calculated for each defect orientation. As a generalism the average levels were used, i.e. $f_{cb} = 0.3 f_c$ and $f_{tb} = 0.6 f_t$. In Figure 4.4, circles are depicted for some defect orientations α, and a strength ratio $f_c/f_t = -8$.

-   The criterion for local bond failure follows from the tangent to the most critical Mohr's circles, presenting the decisive defect orientation for uniaxial tension and compression.

This procedure is illustrated in Figure 4.4. for a ratio $f_c/f_t = -8$. Note that stresses beyond the maximum local tensile stress, corresponding to the tensile loading f_{tb}, are excluded by the tension cut-off criterion.
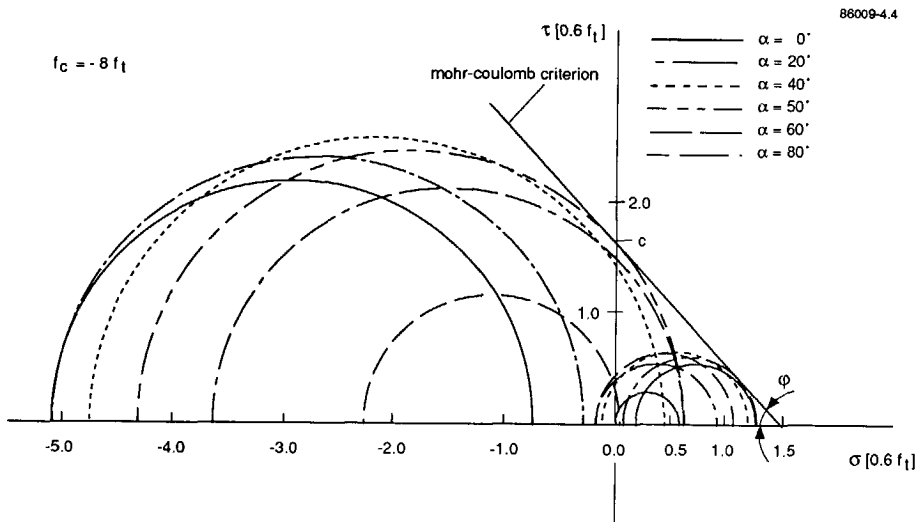
Figure 4.4   The derivation of the decisive defect orientation and the corresponding Mohr-Coulomb criterion.

In the numerical example, the commonly assumed strength ratio f_c/f_t equal to -8 was used. The MC criterion, however, strongly depends on this ratio. For larger, absolute values, the angle φ increases and the MC criterion, combined with the tension cut-off limit, ultimately evolves to a maximum stress criterion, $\varphi = 90°$. The result is an unrealistic insensitivity for the level of the compressive load.

Apparently, in general, the model with the single inclusion is not a sufficient and proper representation of the internal stress distribution decisive for bond failure. This can be explained by the fact that, under compressive loading, the additional tensile stresses between the aggregates cannot be covered by the "single-inclusion model". When the presence of the skeleton is dominant for the strength, the validity of the model is limited. The limitation becomes clearly perceptible for high quality concretes because these concretes have a high strength ratio based on an adequate exploration of the bearing capacity of the skeleton.
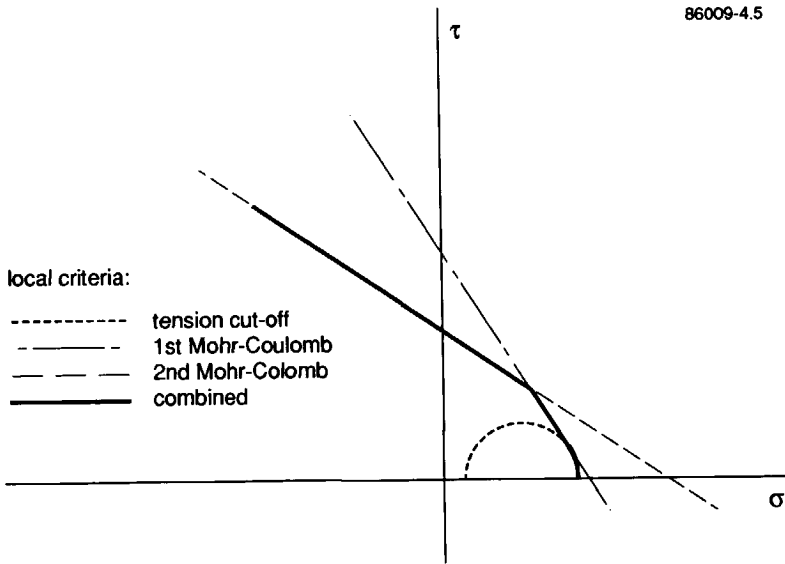
Figure 4.5   The combined failure criteria.

To overcome the shortcoming and still apply the proposed combination of local stresses at the surface of a single inclusion with a local failure criterion, another criterion should be added for conditions where the contribution of the aggregate skeleton becomes dominant. Because this contribution is present in the overall response of concrete, the failure criterion of Mohr-Coulomb of concrete itself was used to find the additional criterion for local failure at high compression levels.

The friction angle φ in the MC criterion for the overall response is determined by the strength ratio f_c/f_t and gives the orientation of the failure plane. To obtain the local criterion this friction angle was adopted and assumed to be also valid for the initiation of bond failure.

To determine the cohesion value of the additional criterion, the most critical Mohr's circle under uniaxial compression was used. The tangent, with friction angle φ of the overall response, to the most decisive stress circle gave the cohesion value. Because this

additional criterion is focused on the response under high compression levels, the most critical Mohr's circle was used for f_{cb} instead of referring to the stress distribution due to tensile loading.

Comparison of φ-values showed that the values for the single inclusion criterion are larger than for the overall response. Therefore the criterion based on the overall response indeed form a more decisive criterion at high compression levels than the criterion for the single inclusion. In the forthcoming text, the criteria based on single inclusion and global response will be denoted as the first and second MC criterion respectively.

To summarize, the procedure to derive the additional criterion for bond failure is as follows.

- Determine the angle φ of internal friction of the MC criterion for the overall response.

- Calculate the cohesion value by considering the tangent at the known angle of internal friction to the most critical Mohr circle for the stresses at the interface of a single inclusion under uniaxial compression f_{cb}.

In the final model, the three criteria were combined as depicted in Figure 4.5.

With this result, the critical load level for defects at the interface can be derived from the stress distribution around a single inclusion in combination with the most decisive failure criterion, i.e. the tension cut-off criterion, the first MC criterion based on f_{tb} and f_{cb} or the second MC criterion with the global friction angle and loading f_{cb}.

Note that in the description, the stresses perpendicular to the plane of loading were not mentioned explicitly. In the analysis procedure these stresses were calculated, but they were not decisive for the derivation of the MC criteria.

Furthermore, the effect of the third dimension on response and failure was ignored in the model by the simple, two-dimensional representation of the aggregates.

4.4   Iso-damage lines for bond fracture

With the local failure criteria given in the former section, the critical load level for initiation of bond fracture can be determined for each defect location at the interface, angle α, under uniaxial and biaxial loading. In Figure 4.6, the critical load level for uniaxial tensile loading is depicted as a function of the defect orientation α, the dashed line.

Another way of interpreting this figure, given in the solid line, is by reading the number of activated defects instead of the orientation angle α. The arc segment, in which defects become activated, can be used to relate different loading conditions.with the same level of internal damage. This feature allowed the construction of "iso-damage-lines" in the biaxial stress space for compression and tension. The known stress

distribution was used to determine these curves which present critical load levels for a certain amount of activated defects.
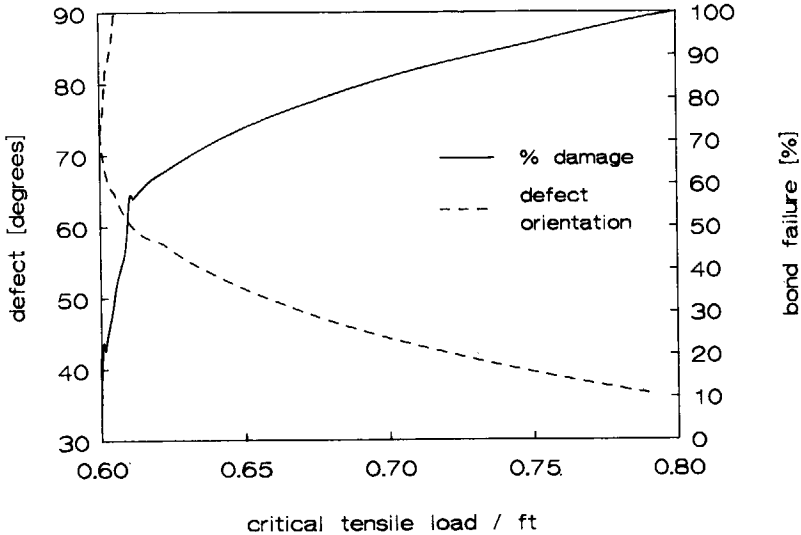
Figure 4.6   Critical load level versus defect orientation for uniaxial tension.

Referring to the basic idea and objective of translating initial damage and internal stresses due to compression to an equivalent initial condition for tension, the condition of uniaxial tensile loading was chosen as reference for the biaxial model.

Before the iso-damage lines for biaxial loading are presented and discussed, first an additional comment on the modelled damage development under tension. The solid line in Figure 4.6 that denotes the percentage of bond failure, shows that just beyond the threshold f_{tb} the damage increases significantly. This feature is caused by the almost uniform stress distribution for small values of α. The most decisive orientation is zero degrees for an infinitely stiff inclusion, but for the stiffness ratios in concrete, bond failure starts at an angle in the range of 10 - 20°. When the defects at 0° are activated the damage development becomes more moderate.

This initial sensitivity of the model affects the shape of the iso-damage lines for biaxial loading. Figure 4.7 shows a number of iso-damage lines in the tension-compression loading regime for the strength ratio $f_c/f_t = -8$ corresponding to the numerical example of Figure 4.4. The index of this figure gives the angle of the arc segment of activated defects and the percentage of damage related to maximum bond failure under tension. The kink in the curves corresponds to the condition of defect activation at 0° under uniaxial tension.
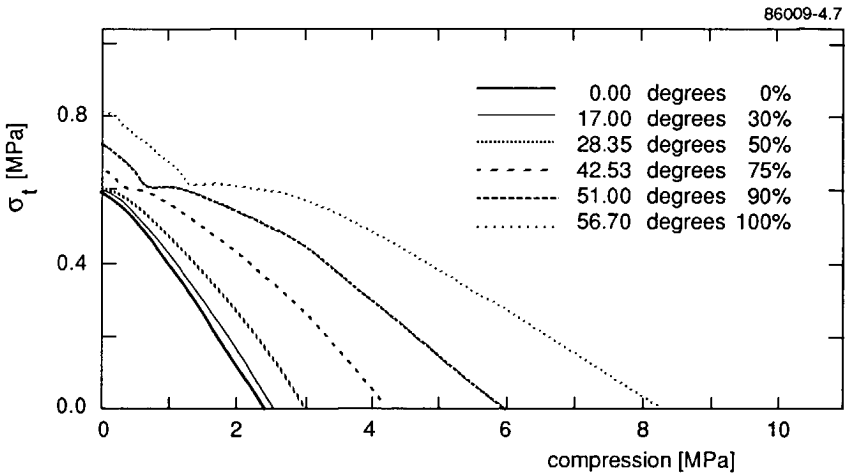
Figure 4.7   Example of iso-damage curves for a strength ratio $f_c/f_t = -8$ and granite inclusion.

In contrast to the sensitivity to small levels of lateral compression the curves show that with increasing compression level the radial compressive stresses at the surface of the inclusion hamper the development of bond failure. This is reflected in the iso-damage lines as a decreasing sensitivity for compressive loading.

The shape of the presented curves for bond failure is derived with the first MC criterion, based on the single inclusion, and reflects reasonably well the shape of the final failure envelope of concrete for this loading regime. However, this parallel vanishes when f_c/f_t increases. With increasing strength ratio, the friction angle φ increases up to 90° and the tension cut-off criterion is used. In this situation the strength of the modelled material is hardly affected by the presence of lateral compression as was mentioned in the former section. For this reason, the second MC criterion was added which covers the conditions of high compression and the contribution of the aggregate skeleton.

To illustrate the necessity of both MC criteria, the approach was applied to the high quality concrete tested in the current programme with $f_c/f_t = -11.8$. In Figure 4.8 the predicted iso-damage curves are depicted for the individual MC criteria and the combined criterion. The curves clearly show that the first criterion hardly enables additional bond cracking at high compression levels due to the presence of the compressive cones on the aggregates. The second MC criterion deals with this insensitivity, see the second diagram of Figure 4.8, but is not suitable for low compression levels. Because the second MC criterion is based on bond failure under uniaxial compression, it overestimates the strength at low compression levels. The third diagram shows the iso-damage lines for the combined criteria.

70
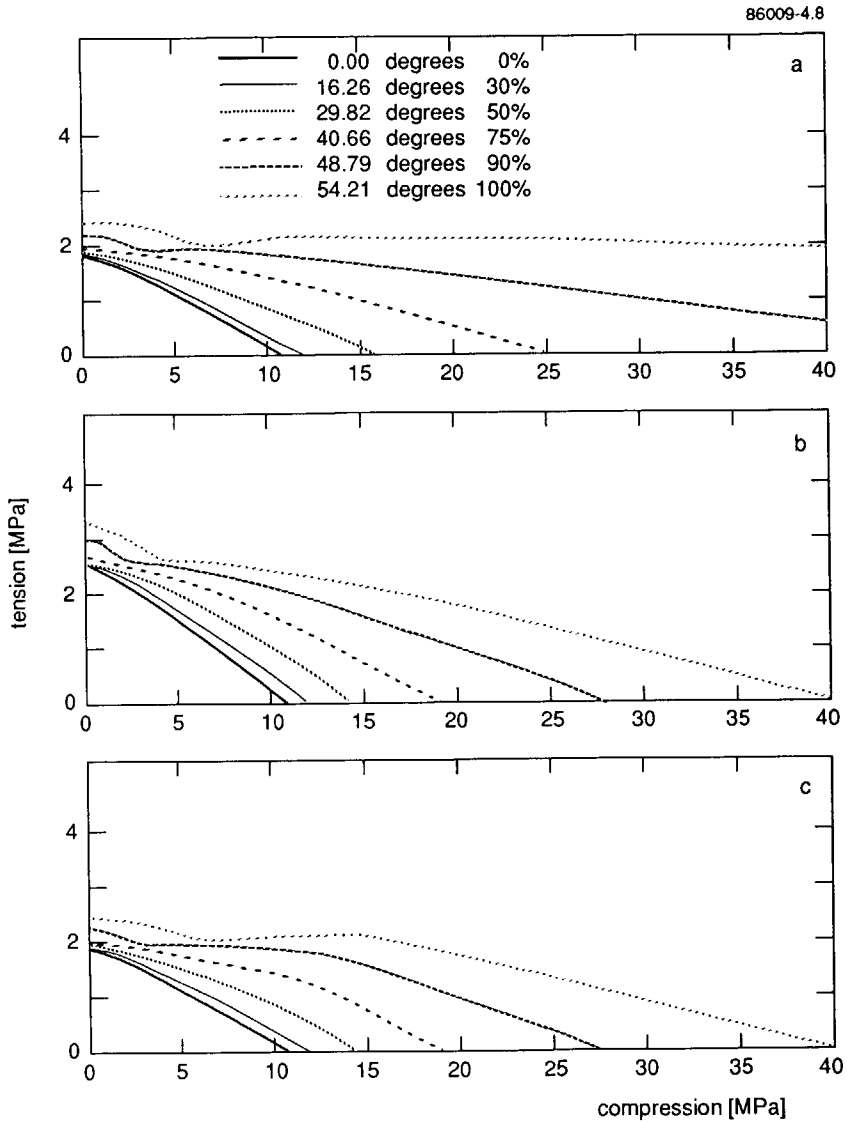
Figure 4.8   Iso-damage lines for concrete of Mix A, f_c/f_t = -11.8. The first, second and combined criterion.

With the combined criteria and the construction of iso-damage lines for bond fracture, the coupling has been achieved between load level, loading condition and level of internal damage. Consequently, a uniaxial compression level can be related to an equivalent uniaxial tensile loading causing the same level of bond failure. It is

emphasized that the equivalent condition refers to the degree of damage and not to the induced internal stresses. In the next section, the final failure envelope will be constructed and compared to results from literature to examine correspondence between iso-damage curves and strength envelopes.

It should be noted that the same damage level does not always imply the same geometrical damage. Especially at low damage levels, the arc of activated defects depends on the loading condition.

4.5 Failure envelope for concrete

To extend the iso-damage curves for bond failure to the failure envelope for concrete, mortar fracture has to be described and the final failure mode should be modelled. In the model, the tensile and the compression mode are distinguished.

In Chapter 3 the crack extension model was introduced. Using this concept, the damage development in the real material is presented in either the fictitious fracture plane for tension or compression.

Dealing with the tension scheme, no additional differentiation of the mortar fracture process is necessary when the crack extension process starts from the bond failure region. The residual resistance of the mortar phase is known and equals $f_t - f_{tm}$.

However, when the compressive loading exceeds the threshold for mortar fracture, f_{cm}, the failure processes in the mortar and the internal stresses have to be related for tensile and compressive loading.

Beyond f_{cm} the internal stress distribution changes, which follows from the volume increase that occurs in this loading range. Mortar fracture decreases the stiffness of the matrix and sliding planes start to develop. To describe the equivalent tensile stresses for this process, additional differentiation of the mortar fracture processes should be included in the model.

Due to the deformations, the ratio of equivalent internal tensile stresses and compressive load will increase. The work of Dougill [21] gives some perspective to include a changing stress distribution in the model. Also the detailed, numerical studies on the failure process using the lattice technique offer possibilities for differentiation.

The question is whether it is necessary, and possible, to include the changing stress distribution in the simple approach. On one hand little data is available to distinguish damage levels in matrix failure and, on the other hand, modelling without decreasing the considered scale level, and increasing the complexity of the model, is not possible. Only an analytical expression relating compression level and equivalent tensile stress should suffice in the current stage of reviewing the possibilities and features of the approach. Based on the aims of the simple model it was decided to use a first order approximation and assume that the equivalent tensile stresses are proportional to the compressive load.

$$\sigma_{eq} = \delta_m \cdot \sigma_c \tag{4.3}$$

with δ_m as a constant derived from the Griffith criterion for matrix fracture in the fictitious fracture plane under uniaxial compression, equation (3.11).

Before the final failure envelope of concrete can be determined by describing the crack extension in one of the fictitious fracture planes, the final failure mode has to be known.
The model does not provide a criterion for the apparent failure mode. Such a criterion should be based on the energy demand. In the compression mode, several sliding planes are formed and the fictitious fracture plane is just a representative. Therefore, a comparison of the energy demand in the single fracture planes does not lead to the failure mode to apply.

Literature provides information on failure envelope and failure mode. Most of the reported biaxial experiments were performed with a proportional tension-compression load path. However, researchers such as Nelissen and Maekawa did not observe an essential loading path dependency in their non-proportional tests. Therefore, in the current study, the results on proportional tests have been used to define the transition in failure mode.
The transition in failure mode was observed by Kupfer [55] and Nelissen [70], see Chapter 2. Kupfer defined the change in failure mode at the ratio of tension/compression of about -0.05, while Nelissen reported the ratio of -0.03. In combination with their experimentally derived failure envelope, the transition was observed at about 0.8 f_c (Kupfer) and 0.95 f_c Nelissen. Maekawa and Okamura [59] performed biaxial experiments more recently and observed a transition at 0.9 f_c.
From these results it emerges that the change in failure mode occurs at high compression levels, but a definite transition point cannot be given.

Considering the schemes in the model, three compression regions can be distinguished. First the region up to f_{cm}, bond failure occurs and additional, axial tensile loading can be described easily in either one of the fictitious planes. Secondly, the region beyond f_{cm} where mortar fracture is started under compression while in the equivalent tensile scheme bond fracture occurs. Thirdly, the region in which the compressive preloading leads to mortar fracture in both schemes.

In combination with the experimental results, it was concluded that in the first and third region, the tensile and compression mode should be used respectively. The second region leads to some discrepancy when the additional tensile load is modelled in the tensile scheme. To exclude this discrepancy, and following the results of Kupfer, the transition was stated at f_{cm}.

With the choices on the failure mode and the equivalent tensile stresses in the matrix, the whole failure process is covered and the iso-damage curves can be constructed.
To illustrate and summarize the proposed modelling, the procedure was applied to the high-quality concrete tested.

- First the iso-damage lines, including the 100% bond failure line, are constructed for bond failure in the tensile failure mode. Some of these curves are depicted in Figure 4.9, see also Figure 4.8.

- In the tensile mode, the additional strength after bond failure is completed is $(f_t - f_{tb})\ 0.2\ f_t$. The curve of 100% bond failure and the failure envelope are parallel.

86009-4.9

a) the tension mode
b) the tension and compression mode
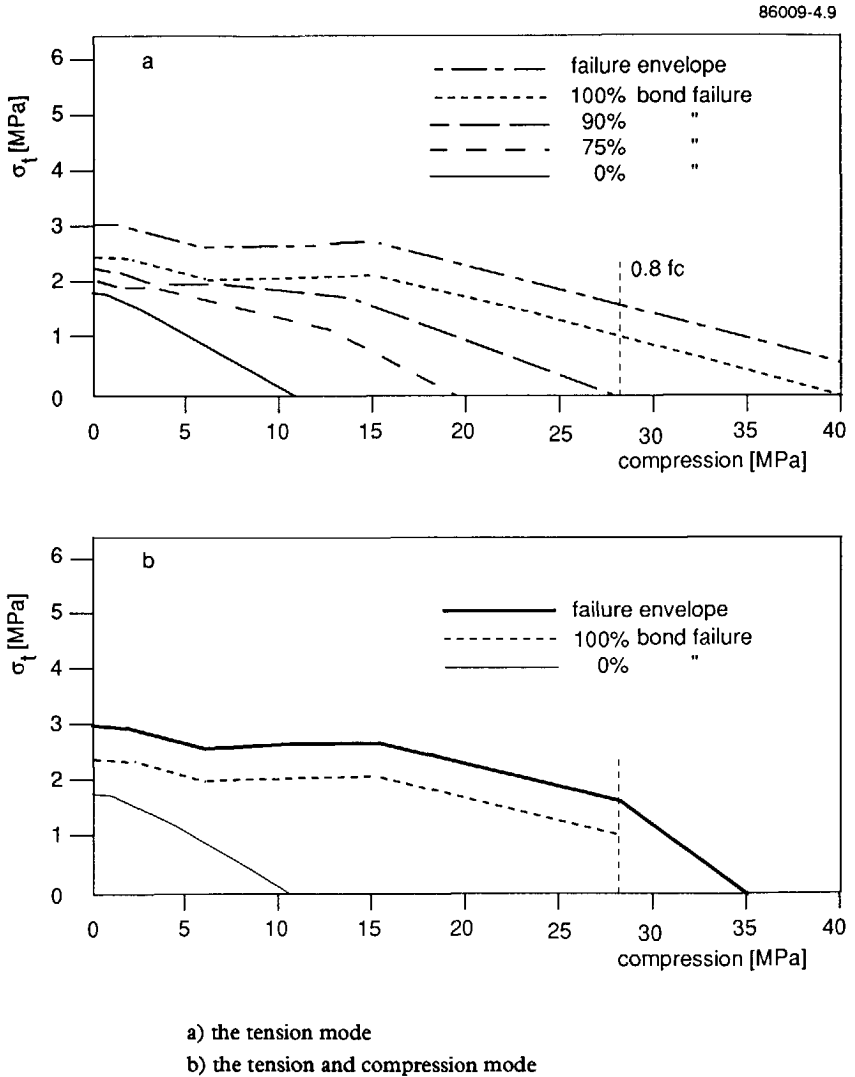
Figure 4.9   The iso-damage lines and final failure envelope for Mix A.

These iso-damage lines and failure envelope for the tensile mode are valid up to the threshold of f_{cm}. Intersection of the failure envelope with the "-0.05" and "-0.03" transition lines of Kupfer and Nelissen occurs at a compression level of 0.85 f_c and 0.97 f_c respectively, which corresponds rather well with their experiments.

- Beyond the threshold f_{cm}, the compression failure mode is assumed to occur. The transcription to the tensile scheme is disposed. The induced tensile stresses follow from equation (4.5.1), $\sigma_{eq} = \delta_m \cdot \sigma_c$. The damage development emerges from the crack extension in the fictitious fracture plane due to the induced tensile loading. Figure 4.10 shows the predicted smooth damage development as a function of the compressive load, which is normalized to the static compression strength f_c.

- The effect of the subsequent tensile loading follows from the crack extension in the compression scheme, starting with the initial damage and stresses due to the compressive load. This leads to the prediction of the final failure envelope in the compression mode.
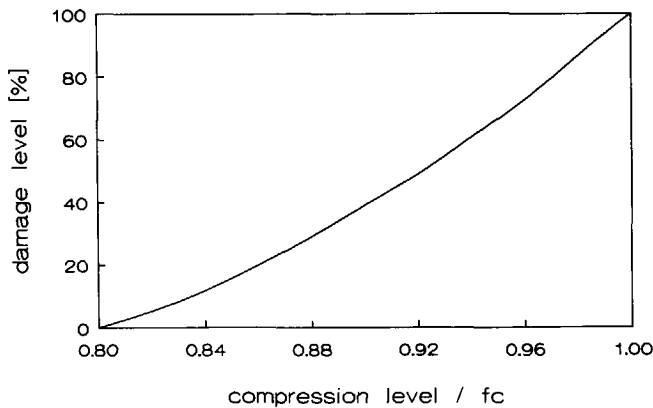
Figure 4.10   Damage development in the compression scheme.

The result for Mix A is given in Figure 4.9b. The same procedure was applied to the low quality concrete, Mix B. After the envelopes were normalized to tensile and compressive strength, the modelled damage development appeared to be just slightly different. Figure 4.11 presents these normalized envelopes and the experimental results of Kupfer for two concrete qualities with about the same compressive strengths as Mixes A and B. The envelopes are normalized by means of the static tensile and compressive strength, f_{ts} and f_{cs}, respectively. The curves show that the trends of prediction and experiments are the same. However, the model seems to slightly underestimate the influence of compression in the range of 0.2-0.7 f_c. In this loading range the model predicts that the bond failure process is hampered by the presence of

the compression cones on the aggregates. Tuning the model parameters enables us to fit the prediction to the experimental results of Kupfer.
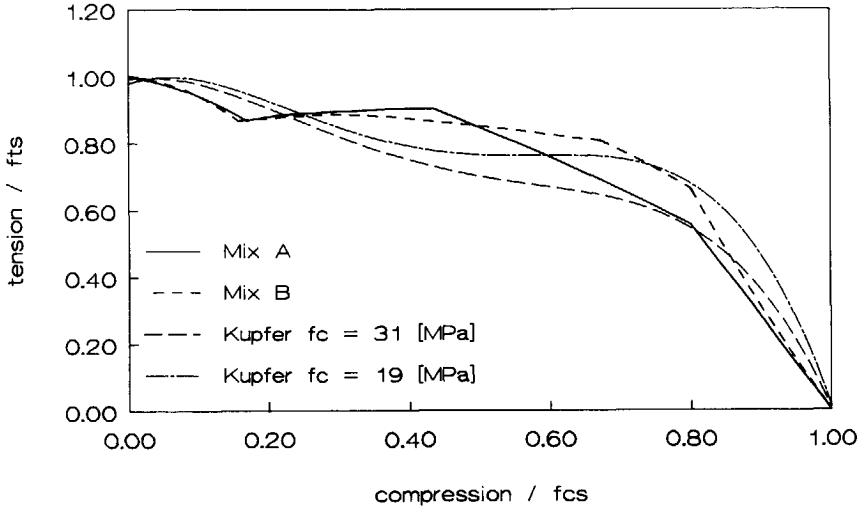
Figure 4.11   The normalized failure envelopes for Mix A, B and some experimental results of Kupfer [55]

It should be noted that the result as depicted in the Figures 4.9 and 4.11 are the result of a series of simplifications, trying to follow the main response features of concrete and including the dominant mechanisms. After the introduction of the fictitious fracture planes, with quite a number of assumptions, and the approach of equivalent damage and stresses to relate various loading conditions, the result is quite promising. The approach leads to a realistic damage envelope with a rather good correspondence with the empirical envelopes derived by Kupfer.

Because of the good correspondence between modelled damage development and strength or failure envelope from literature, the modelling approach was accepted to be a sufficiently reliable base to study the rate effect on the residual tensile strength.

4.6   Rate effect on residual tensile strength

The main objective of the current study was to determine the influence of a static, lateral compression on the residual impact tensile strength. With the model developed so far, the static failure envelope of the residual strength could be predicted. To predict the rate effect on residual strength, the fracture model, as given in Chapter 3, was

applied to describe crack extension in the fictitious fracture plane for failure in the tensile or compressive mode. The influence of static compression on the initial conditions followed from the iso-damage line corresponding the compression level.
As described in Chapter 2, and following from the results of Chapter 3, there are two mechanisms responsible for the rate effect on the uniaxial tensile strength. First, the changing energy demand due to the changing geometry of the fracture plane and multiple cracking and, secondly, the inertia effects around the crack tip that decrease the stress concentrations and delays the fracture process.

Changing the initial conditions by lateral compression will affect the crack propagation process in the fictitious fracture plane. The second mechanism is expected to be covered by the model.
The influence of compression on the first mechanism, however, is hard to quantify because there are two opposite effects. On one hand prestressing causes precracking in the potential fracture plane and the change from bond to aggregate fracture will become less. On the other hand, the precracking occurs all through the material, creating an increasing number of potentially decisive cracks. Due to this effect, multiple cracking might become much more important. The first aspect decreases the demand on fracture energy while the latter would cause an increase.
Considering the developed model, the aspect of multiple cracking was not incorporated and no data is available to estimate and quantify the change in energy demand. Therefore, this influence was ignored and only considered as a possible cause for an underestimate of the rate effects at biaxial loading.
In order to deal with the first aspect, two extreme calculations were made.

- First an upper limit for the rate effect was predicted by assuming that the specific surface energy was not affected by static compression.

- Secondly, a more realistic prediction was made. It was assumed that, after prestressing, only the residual bond fracture area could be replaced by aggregate fracture. In the range from static loading up to a loading rate of 1000 GPa/s, a logarithmic dependency was adopted

The realistic prediction will be used as "the model prediction", or it will be mentioned explicitly.

Figures 4.12 and 4.13 give the result of both calculations. It appears that, even at overestimated fracture energy, the lateral compression affects the rate effect on residual tensile strength significantly. The maximum difference between both predictions occurs in the range 10 - 100 [GPa/s] at a compression level just beyond f_{cb}. At these conditions the ratio of the predictions is about 1.2. Beyond the level of mortar fracture initiation, f_{cm}, where the compression failure mode is activated, the differences disappear because no aggregate fracture occurs.
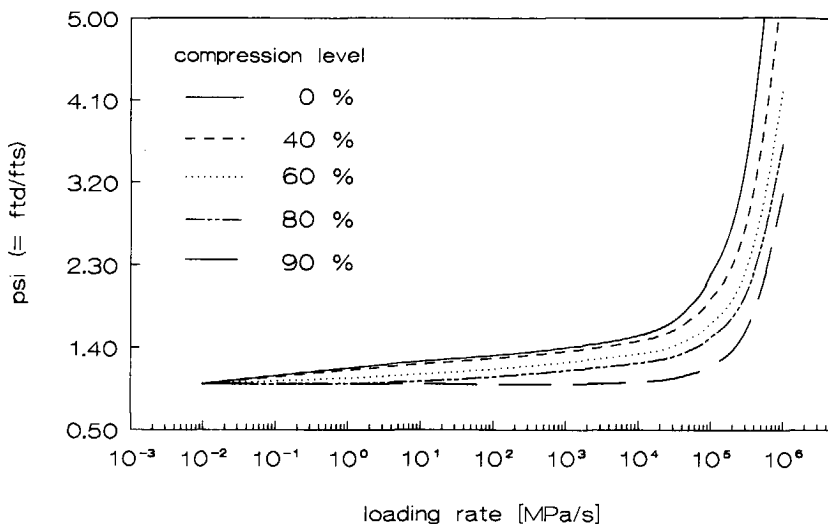
Figure 4.12   Rate effect PSI (= f_{td}/f_{ts}) on the residual tensile strength for various levels of lateral compression. Prediction with overestimate of dynamic fracture energy.
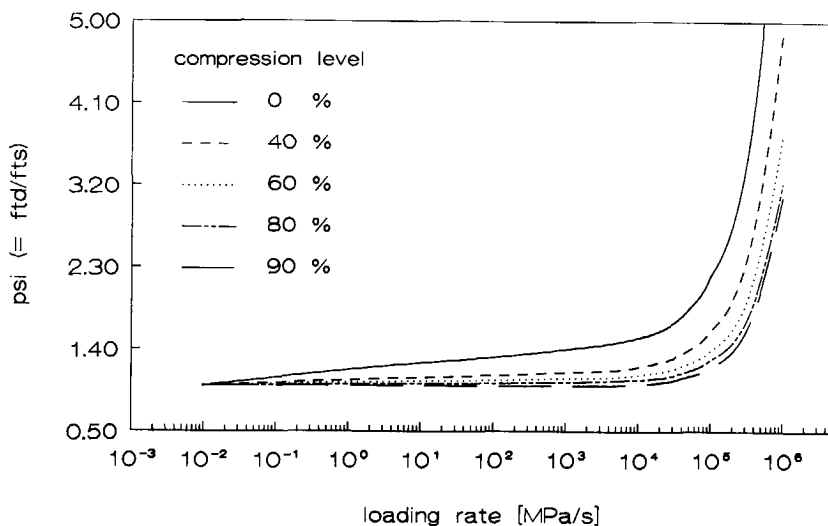
Figure 4.13   Rate effect PSI (= f_{td}/f_{ts}), on the residual tensile strength for various levels of lateral compression. Prediction with "realistic" estimate of dynamic fracture energy.

Together with the reported results of Takeda and Zielinski, who stated that the rate effect is not affected by lateral compression, three predictions can be made for the failure envelope. In order to illustrate the differences, they were applied to the empirical envelope proposed by Kupfer for low strength concretes. Figure 4.14 gives the results and illustrates the differences in the dynamic residual strength predicted.
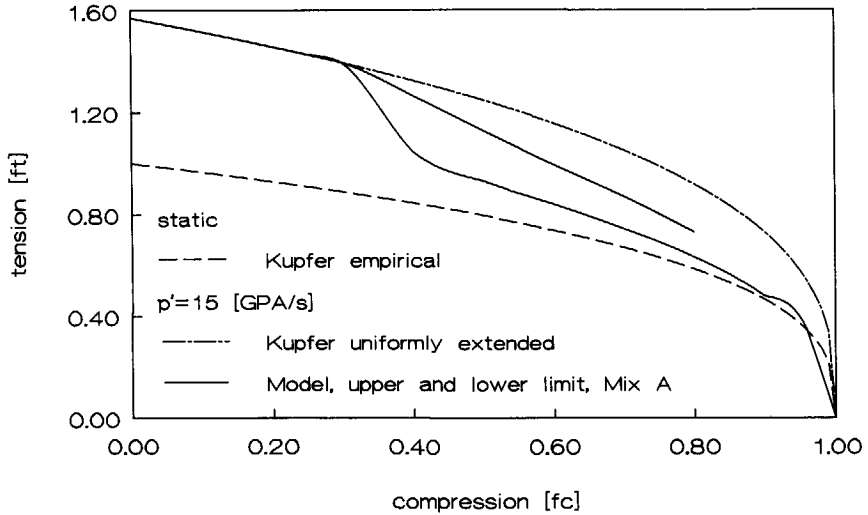
Figure 4.14   Three predictions for the dynamic failure envelope at a loading rate of 15 [GPa/s]. Static reference is Kupfers empirical relation.

In Chapter 7, the data of the current programme will be used to judge the validity of the predictions and the influence of multiple cracking on the dynamic residual strength. At this stage it is concluded that the lateral compression has a significant influence on the rate effect. The dynamic failure envelope tends to the static envelope at high compression levels. The gap between the model predictions and the constant rate effect proposed by Zielinski can only be bridged when the multiple fracture appears to be the major mechanism in the considered biaxial loading regime.

4.7   Concluding remarks on biaxial model

The biaxial model presented in this chapter results in a static failure envelope that exhibits the features given in literature. It shows that the internal stresses and damage due to lateral compression can be related to the damage development under tensile loading as described in the biaxial model. The level of internal damage and induced tensile stresses can be used as a set of new initial conditions to be presented in the fictitious fracture plane.
The description of the crack extension in the adjusted fictitious fracture plane results in a rate effect on the residual tensile strength that depends on the level of compression.

5 THE EXPERIMENTAL PROGRAMME

The main item of the experimental programme was the failure envelope under static lateral compression and axial impact tensile loading. In order to examine the influence of lateral compression, uniaxial impact tests formed the reference.

Because the strength is determined by the development of the fracture process, attention was also paid to the fracture energy and the deformation in the fracture zone. The deformation capacity of the fracture zone was the second item of the experimental programme.

The tests were performed in a modified Split Hopkinson Bar apparatus on a notched specimen with a prismatic geometry.

The scope of the experimental programme and the experimental set-up will be described in this chapter.

5.1 Scope of the experimental programme

The experimental programme was focused on answering the question whether the rate sensitivity of strength and the energy demand are affected by the level of lateral compression. The main objective was the strength envelope, while the information on the energy demand and deformation should lead to a better understanding of the failure mechanism.

The shape of the failure envelope was the subject of the former chapter and the possible influence of lateral compression was sufficiently introduced. The importance of the deformation capacity in the experimental programme, however, needs some additional comment.

From literature and the preceding chapters, it emerged that uniaxial response of concrete under impact tensile load is quite well known. Strength appears to be sensitive to loading rate, while the deformation capacity seems to increase with increasing loading rate also. The word "seems" is used because the capacity is coupled to the fracture zone and its size. The occurrence of multiple fracture will certainly affect the observed deformation during tests. The question is whether the increase is a real material response or caused by inertia effects in the structural response. This question becomes more important in view of numerical simulations in which the structural response is already dealt with and should be combined with true material behaviour in order to obtain reliable results.

For this reason, and the fact that the fracture process, with the accompanied inelastic deformation, determines the strength, it was decided to perform the experiments on a notched specimen to fix the location and realize a single fracture zone. Gathering data on the deformation capacity of a single fracture zone was stated as one of the aims of the programme. It also made the uniaxial experiments more valuable. They were given a two-fold meaning; on one hand they formed the reference for the biaxial tests, and

on the other hand, data was obtained on the deformation capacity of a single fracture zone which was not available from literature.

To summarize, the experimental programme had two items, i.e.

- the failure envelope, or strength under static lateral compression and axial impact loading, and

- the deformation capacity and fracture energy of a single fracture zone.

The tests were performed in the Stevin Laboratory of the Delft University of Technology (DUT). In this laboratory, extensive research programmes on the response of concrete under uniaxial impact tensile loading have been performed using a Split Hopkinson Bar apparatus (SHB). For the current programme, the set-up was combined with a hydraulic loading device in one, lateral direction. These devices will be described in the next sections.
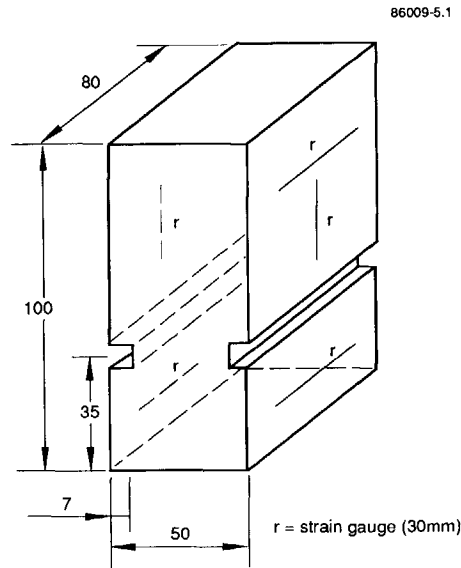
Figure 5.1   The geometry of the specimen and the locations of strain measurements.

The choice of the biaxial loading condition instead of the triaxial condition with a cylindrical specimen was mainly based on the available equipment. The compression device, with brush bearing platens, constrained to a prismatic specimen geometry. But the set-up also offered two free surfaces to perform strain measurements on the

specimen. Figure 5.1 shows the geometry of the specimen and the five locations of strain measurements. Due to the application of notches, with sufficient depth, the failure zone is fixed and the material outside responds elastically in the uniaxial tests.

By recording the total deformation of the whole specimen as well as the elastic deformation outside the fracture zone, the deformation of the fracture zone itself could be determined.
Together with the conventional way to derive the impact strength from the transmitted pulse in the SHB, the demands on strength and deformation data were covered by the experimental set-up with the prismatic, notched specimen.

5.2   Experimental set-up

Zielinski performed preliminary experiments on the biaxial loading condition [125] of the current programme. The applied experimental set-ups are basically the same. Lessons were learnt from his results, and the set-up was improved and modified, see [116 and 117].

5.2.1   Split Hopkinson Bar

The Split Hopkinson Bar (SHB) technique has been used to generate the dynamic tensile loading. This technique has proven its applicability [79] for concrete testing. In the DUT set-up loading rates in the range of 2 to 20 [GPa/s] can be realized. The SHB, shown in Figure 5.2, consists of two cylindrical (Ø 74 mm) aluminium bars between which the concrete specimen is glued. The stress wave is generated by a drop weight, which slides along the lower ("incident") bar and hits the anvil at the lower end. The loading pulse depends on the drop weight mass, the velocity (drop height) and the layer applied between the drop weight and the anvil. In this way a stress wave can be generated with an approximate constant strain or loading rate. From uniaxial wave theory, which forms the base of the SHB technique, it follows that due to the mismatch of impedances between the bars and the specimen, repeated reflections occur at the interfaces during transmission of the pulse. The stress rate in the specimen, however, is the same as in the incident pulse. Only a time delay whose magnitude depends on the impedances and the size of the specimen occurs. In the applied set-up, the stress-time relation is determined with strain measurements at the upper ("transmitter") bar, while the deformations are measured directly on the specimen. The basic ideas and theory of the SHB technique are described by Zukas et al. in [127], while the apparatus at the DUT is described in [51]. One of the limitations of the technique is the disynchronization of the load and response measurements when the response and/or the load become non-linear, see 5.3.1.

82

880431-2

1	buffer
2	upper bar
3	guide
4	straingauge
5a	upper cooling jacket
5b	lower cooling jacket
6	concrete test specimen
	Ø 74 x 75 mm
7	working platform
8	counterweight
9	lower bar
10	frame
11	drop weight
12	coupling
13	uncoupling
14	lifting device
15	damping material
16	anvil
17	guide tube
18	pneumatic jack
19	frame base
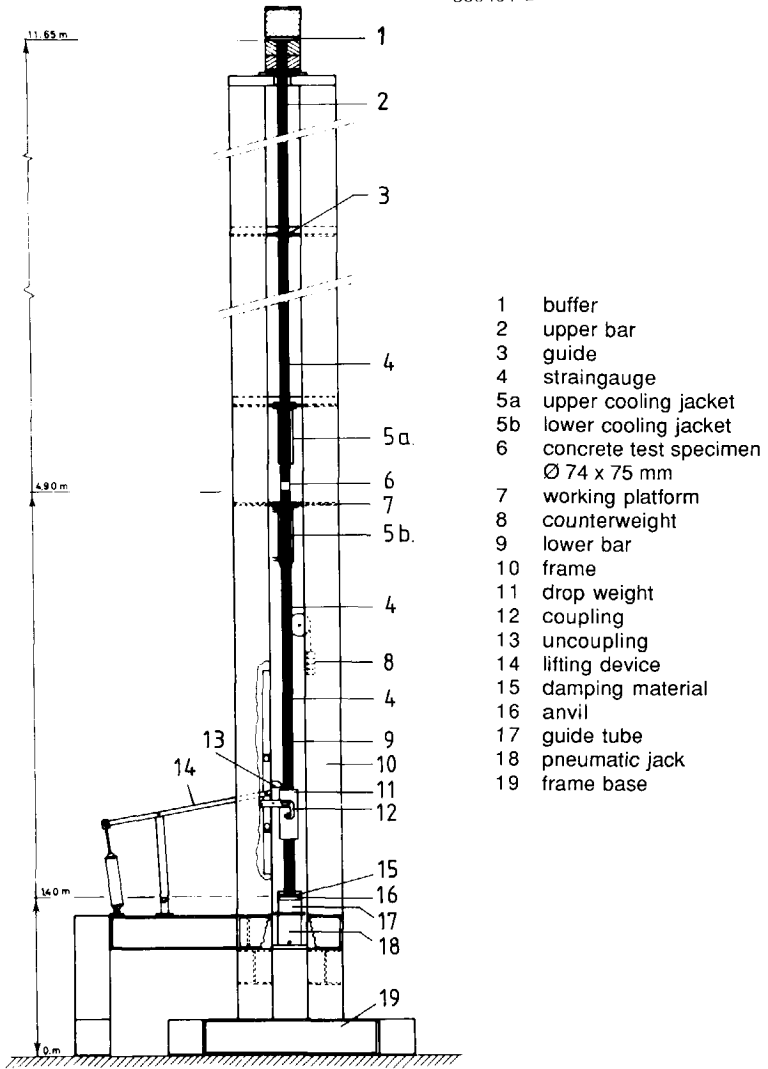
Figure 5.2 Schematic diagram of the Split Hopkinson Bar equipment.

5.2.2 Lateral-compression device

The SHB was combined with an additional prestressing device to enable biaxial testing. The equipment is depicted in Figure 5.3. The limited space available led to a compact equilibrium system of two hydraulic jacks, the specimen and tension rods. The device consists of two tension rods (1) between fixed rigid platens (2), and two

guiding platens (3), see the figure. The prestressing jacks (4) with a capacity of 200 kN each, slide along the rods and the compression force is applied to the specimen by brush-bearing platens (5). These platens consist of (4 x 4 x 100 mm³) steel rods, which are spaced with a clearance of 0.2 mm. One of the bearing platens is connected through a spherical seat. At one end of the set-up a force measuring device (7) is placed between the guiding platen and the platen at the end. To limit the friction between the platens and the rods, bronze bearings (8) are applied. Nevertheless the friction appeared to be too large to rely on the force measurement. To eliminate the influence of friction on load recording during the tests the deformation of the steel rods were measured by means of strain measurements between the guiding platens.
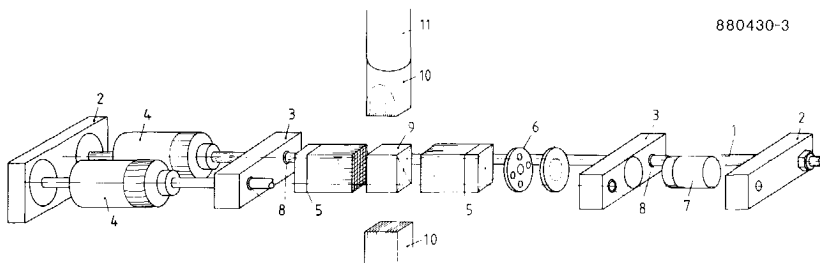
1	tension rod	7	force measuring device
2	fixed platen	8	bronze bearing
3	guiding platen	9	specimen
4	jack (200 kN)	10	aluminium adapter
5	brush-bearing platen	11	transmitter bar of
6	spherical seat		SH-equipment

Figure 5.3 Prestressing device in experimental set-up.

The transition of the cylindrical bars of the Hopkinson equipment to the rectangular cross-section of the specimen was realized by means of adapters (10) whose shape minimizes the disturbance of the stress pulse.

The geometry of the brushes satisfies the stiffness requirements with respect to free deformations at the loaded faces of the specimen, see Nelissen [70].
It should be noted that due to the limited stiffness of the compression device, the observed compressive strength will be lower than obtained from testing in a rigid device. For this reason the level of compression will be related to the specimen strength in the test set-up.
More information on the static compression device is given in [116] and [117].

5.2.3   Measurement set-up

The measurement set-up is presented schematically in Figure 5.4. At the upper bar, two strain gauges (6 and 7) were applied to measure the transmitted pulse to determine the residual tensile strength. Additionally, the strains were measured at the lower bar (8 and 9) to verify the reproducibility of the incident stress pulse. On both bars, two axially symmetric strains are measured to detect and quantify additional bending, see next section.
The longitudinal, total deformation of the whole specimen was recorded with two displacement transducers (12 and 13), which were mounted on the adapters next to the specimen. As was mentioned before and depicted in Figure 5.1, the axial deformation of the specimen outside the failure zone were measured with two strain gauges (1 and 2). The lateral deformation of the specimen under dynamic and static loading were recorded by the strain measurements (3), (4) and (5). With the five strain gauges at the specimen, symmetry of the compressive load and bending during impact loading could be verified. In addition to the force measuring device, the compressive force followed from strain measurements. On each tensile rod of the prestressing device, two pairs of strain gauges were placed, each in perpendicular pattern for longitudinal and lateral deformation. The strain signals are amplified with a bridge amplifier (I). To eliminated the influence of bending, the gauges at the tension rod were inserted in a four-arm configuration while the other nine strain measurements were performed separately in the ordinary single-arm configuration.
The displacement signals were amplified separately (III) and with the strain signals fed to a tape recorder (IV). After each test, the signals of the transmitter bar were checked with a transient recorder (II). Afterwards all the signals were digitized simultaneously (V) and stored at the central computer. The signals were analysed by means of an extensive programme for data processing [107].

5.3   Evaluation of the experimental set-up

The main part of the evaluation consisted of an experimental programme to examine several aspects of the set-up by means of an aluminium specimen. The necessity of these experiments emerged from the uncertainties about the effect on the uniaxial loading condition of the prismatic specimen geometry and the notches. The second aspect that had to be examined was the reproducibility and the shape of the generated loading pulse, especially for low stress levels. Thirdly, the lateral compression device was new and had to be evaluated. Finally, there was the most crucial aspect, the interaction between the static and dynamic device. The most important results of the preliminary tests, see [117], are summarized in this section.

86009-5.4
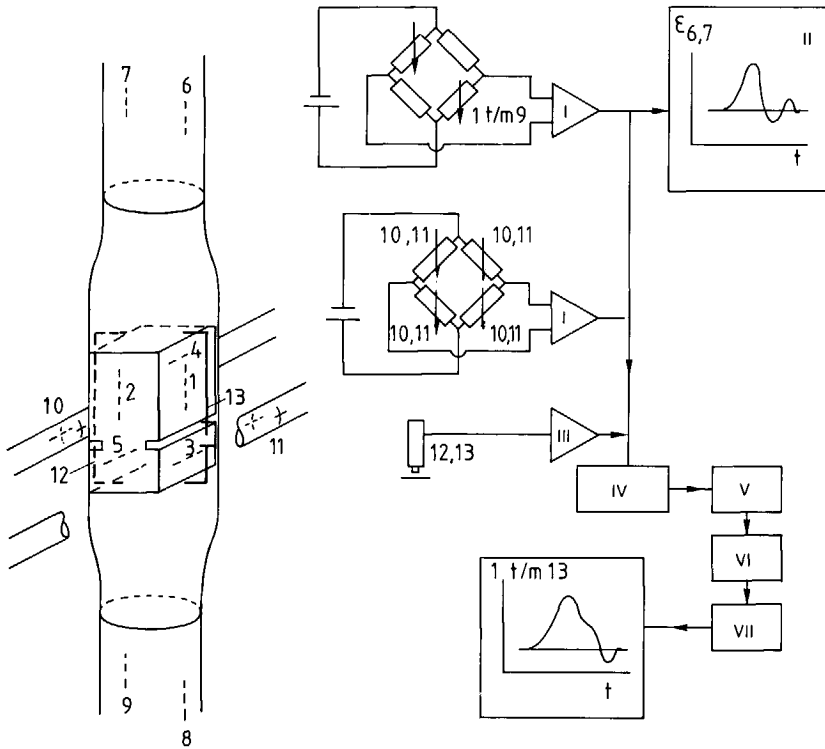
1 - 5	Strain gauges; 30 mm
6 - 9	Strain gauges; 6 mm
10 - 11	Pairs of strain gauges
12 - 13	Contactless displacement gauges; VIBRO TQ102
I	SELABS SE 994; 50 kHz; bridge amplifier
II	NICOLET Explorer II; transient recorder
III	Amplifier; Delft University
IV	SELABS SE 3000; 14 channel tape recorder; 40 kHz at 60 ips
V	DIFA Benelux TS-9000; 14 channel AD-converter; 250 kHz
VI	PC DIGITAL 350
VII	VAX 11/750

Figure 5.4   The measurement set-up.

5.3.1 Consequences of non-linear effects

The principle of the SHB technique is very simple and easy to interpret under the conditions of a linear loading pulse, a linear-elastic response and a small specimen size. Furthermore, the condition of uniaxial wave propagation must be fulfilled. In concrete testing, these conditions can never be completely fulfilled. To examine the consequences of non-linear loading and response, and determine the order of magnitude of the introduced errors, the first order effects in wave propagation were theoretically analyzed for the SHB [120].

The condition of linearity and small specimen size emerge from the situation that load and response are registered at different locations and different times. These recordings have to be synchronized to obtain the data. When a material is tested with a different acoustic impedance than the SHB, reflections occur at the interfaces and it takes some time before the loading rate in the specimen equals the loading rate of the incident and transmitted pulse. Or in more general terms, each change in load or response will cause a temporary mismatch between loading and response. Consequently, non-linear loading causes a continuously changing mismatch and a unique synchronization is impossible.

For the applied test conditions, the generated loading pulse has a linear ascending branch, except for the very first part of it. Non-linear effects occur when the concrete starts to fail. In order to limit the differences between loading and response during the failure process, the moment of maximum amplitude was used for synchronization in the analysis of the experiments.

Based on the theoretical analysis, the non-linear effects might lead to an overestimate of the strength of 5% maximum for the tests of the current programme. Concerning the reconstructed load-deformation relation, it should be noted that it will not reflect the true material response due to non-unique synchronization.

5.3.2 The specimen geometry

The uniaxial wave propagation and stress distribution will be disturbed by the transitions from circular to rectangular cross-section. Due to demands on the lateral stiffness, the adapters were also provided with twelve saw cuts of 1 mm width and 40 mm depth. From the experiments it emerged that the stress waves were definitely affected by the non-ideal geometry. But, the first part of the loading had a constant loading rate and the stress pulse in the specimen could be derived from the recorded pulse in the upper bar. Or, in other words, the principle of the SHB could still be applied and a constant loading rate could be realized if failure occurred in the first part of the pulse. An example of the pulses is given in Figure 5.5.

To study the effect of the notches on the stress distribution in the fracture zone, FE calculations were made and the strains near the notches were recorded during tests. Three types of geometry were tested, i.e. without notches, hemi-circular and rectangular notches, see [116, 117]. The application of notches leads to stress concentrations in the adjacent material. This aspect demands more attention with increasing loading

a) axial deformations
b) axial and lateral deformation in the specimen
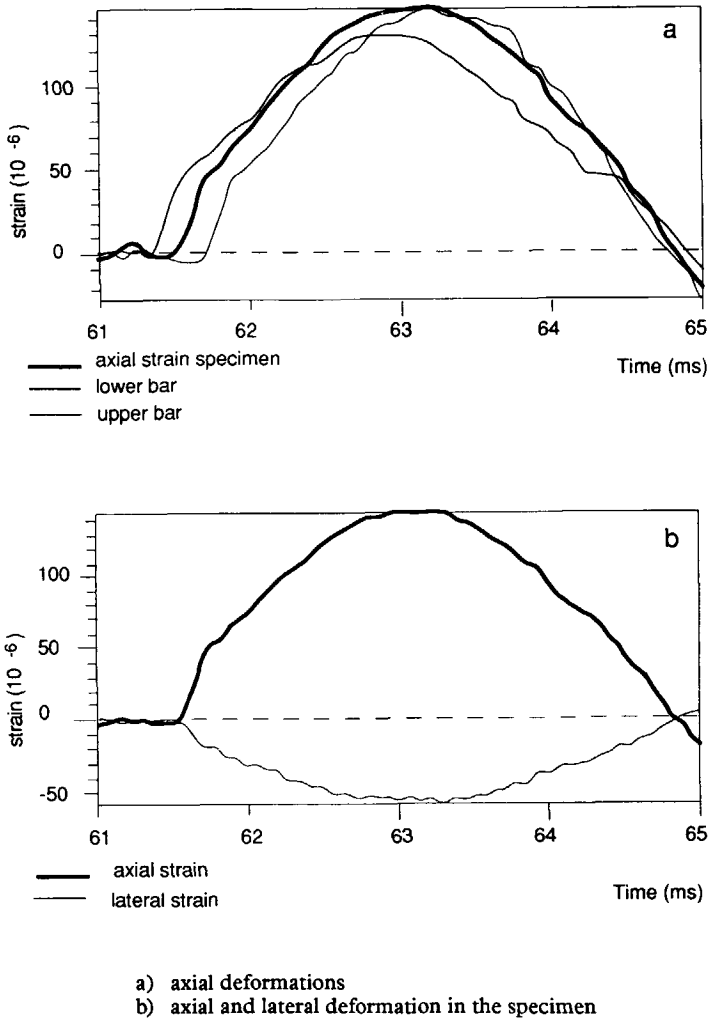
Figure 5.5   Registered pulses below, in and above the aluminium specimen for axial impact loading.

rate. The strength of the specimen will be reduced and the behaviour becomes more brittle because the redistribution of stresses, due to micro-cracking, lags behind in the extending zone of the stress concentration. For this reason, in the applied geometry with rectangular notches, the loading rate must be limited to about 10 GPa/s. This limit is based on a simple, theoretical model to predict the strength decrease as a function of crack depth and loading rate, see [115, 120] and section 6.1.3.

Under biaxial testing the influence of the reduced section will decrease as a result of the induced internal damage due to the static compressive load.

5.3.3 Axial impact loading

First of all, the reproducibility of the generated stress wave was tested. A range of pulse amplitudes and loading rates were examined. The scatter in the maximum stress of the pulse appeared to be less than 5% (coefficient of variation). For the loading rate this is about 10%. Based on the empirical strength relation, this scatter will lead to a few percent variation in strength. Another aspect is that for concrete testing a constant loading rate must be achieved, especially after crack initiation. At the beginning and near the maximum of the pulse, the loading rate is not constant. Therefore, the test conditions should be chosen carefully to create the same loading conditions for specimens with a high and a low residual strength. The preliminary programme gave the information on the optimum test conditions.

During the tests it appeared that the uniaxial stress condition in the SHB can be easily disturbed by additional bending stresses due to non-symmetrical loading of the anvil and the lower bar. Because of the low residual strength at high compression levels, these additional stresses can significantly disturb the results. This might have been one of the causes for the scatter in the results of Zielinski [125]. In the preliminary evaluation programme the conditions were determined at which the influence was diminished to an acceptable level. During the test on concrete this aspect was checked carefully.

5.3.4 Lateral compressive loading

The prestressing device is counterbalanced and can be easily handled. However, the realization of a uniaxial loading condition appeared to be rather difficult. The strain gauges at the specimen and the tension rods were an indispensable aid. Improvements can be achieved by the application of a single jack and a hemispherical seat with a larger radius.
The aspect of friction has already been mentioned before. Due to the application of bronze bearings and the strain gauges on the tension rods, the load on the specimen could be controlled well.

A significant problem appeared to be the deformation capacity of the glued seam. The most obvious sequence of test performing in the biaxial programme was to glue the specimen between the adapters of the SHB first. After hardening, the lateral compression could be applied, followed by the dynamic part of the test. In this sequence, the additional damage due to creep should be excluded. Tests with an aluminium specimen, however, showed failure of the glued seam during compressive loading. This failure occurred due to the lateral stiffness of the adapter and the limited deformation capacity of the glued seam. This problem was solved by decreasing the stiffness of the adapters by twelve saw cuts of 4 cm depth, and adding sand to the glue. The best results were obtained with sand that had a maximum diameter of 0.125 mm and a volume ratio glue to sand of 1/3. With these adjustments the seam

did not fail at a lateral deformation of 0.1%. This deformation level was not exceeded during the final test programme by changing the sequence in test preparation. First a part of the compressive load was applied, then the specimen was glued in the SHB. After hardening time, the compressive load was increased to the final level.

In this test set-up and with the described sequence, the lateral compression could be applied followed by the dynamic impact test.

5.3.5   Interaction between loading devices

Another aspect that had to be examined was the interaction of both devices during dynamic loading. During impact loading the specimen will also deform in a lateral direction and consequently the prestress level will be affected when the static loading device cannot follow the dynamic lateral deformation. Furthermore, the principle of uniaxial wave propagation in the SHB might be ruined by the "lumped mass" of the prestressing device. By comparing the incident and the transmitted wave, the dynamic response of the biaxial set-up was tested. Figure 5.5 showed the pulses in the final set-up but without compression. The influence of the compression device emerges from the recordings depicted in Figure 5.6.

From the uniaxial tests it emerged that regular transmission and reflection of the incident wave occurs and the stress in the specimen can be derived from measuring the transmitted pulse in the upper bar. The results from biaxial testing are quite different. The shapes of the incident and transmitted pulse show similarities but a relation cannot be derived from uniaxial reflections. Regular reflection only occurred in the first, linear part of the pulses. The irregular response was initiated by the lateral deformation of the specimen. This follows from the fact that first the lateral deformation of the specimen decreases to about the level before impact loading and, subsequently, the axial deformation drops to zero. Apparently the compression device could not respond sufficiently to the dynamic deformation, and the distance between the brushes was more or less fixed. Consequently the lateral deformation was forced to equal the level according to static compression. During the lateral response, the contact between specimen and brushes appeared to be diminished and after the contact is re-established, the loading device acts like a support for the residual impact loading. These experiments were described extensively in [117].

The interaction between both loading devices had no consequences for the experimental programme because the applicability of the generated loading pulse was limited to first, linear part with regular reflections. Concrete has a lower Poisson's ratio than aluminium, so the observed phenomena did not occur at a lower stress level and the test conditions did not have to be changed. In concrete testing, however, the results should be considered very carefully at large deformations because of the limited adjustment capacity of the compression device to dynamic deformation.

a) pulses below, in and above specimen
b) axial and lateral strains in the specimen
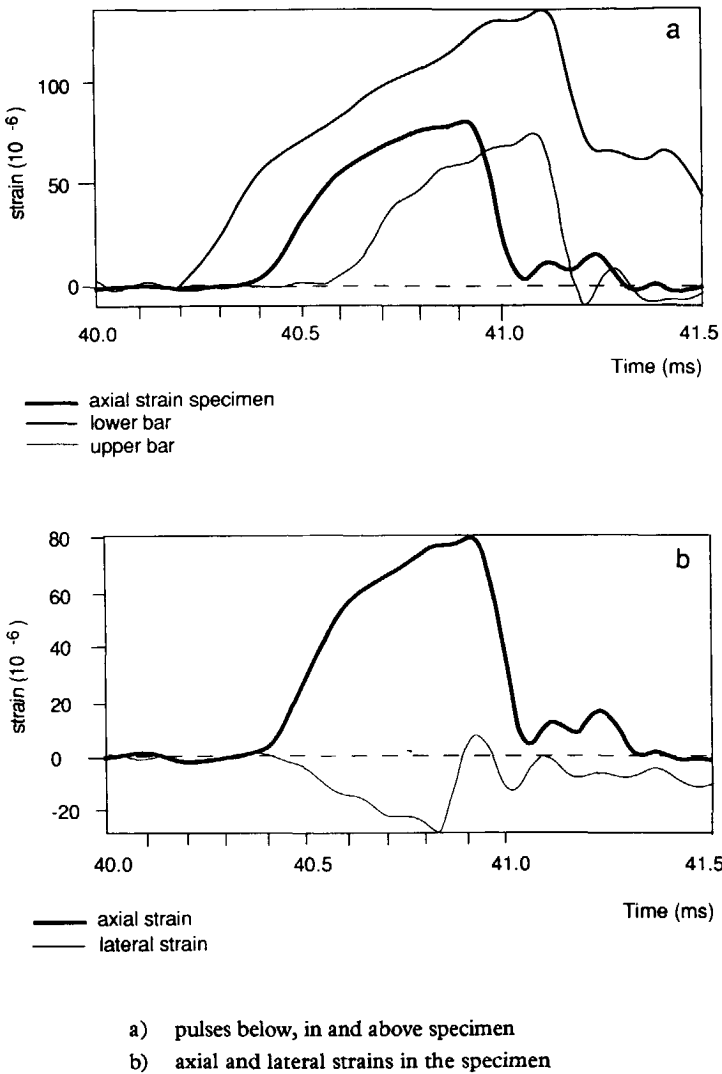
Figure 5.6   Registered pulses below, in and above the aluminium specimen during axial impact loading with lateral compression.

5.4   Experimental programme

The experimental programme was mainly focused on the objective concerning the shape of the failure envelope. The first aim was to get a definite answer on the question whether the rate sensitivity of the residual strength was affected by the compression level. It was decided to perform biaxial tests with compression levels beyond 0.5 f_c. The reasons were:

- static failure envelopes show only small deviations from the uniaxial tensile strength at low compression levels;

- at high compression levels, the apparent internal damage was expected to be sufficient to affect the geometry of the final fracture plane and the mechanism of rate sensitivity;

- testing concrete in the biaxial loading regime of compression and tension implies a considerable scatter in test results. The variance in tensile and compressive response and the variance in both independent loadings are superposed;

- the number of experiments was limited and, considering the inevitable scatter in data, attention should be focused on a few compression levels.

The chosen compression levels were 0, 50, 75, and 100% of the static compressive strength f_c. The 100% level was necessary to determine the compressive strength of the specimen in the prestressing device. The 0% formed the reference for uniaxial response.
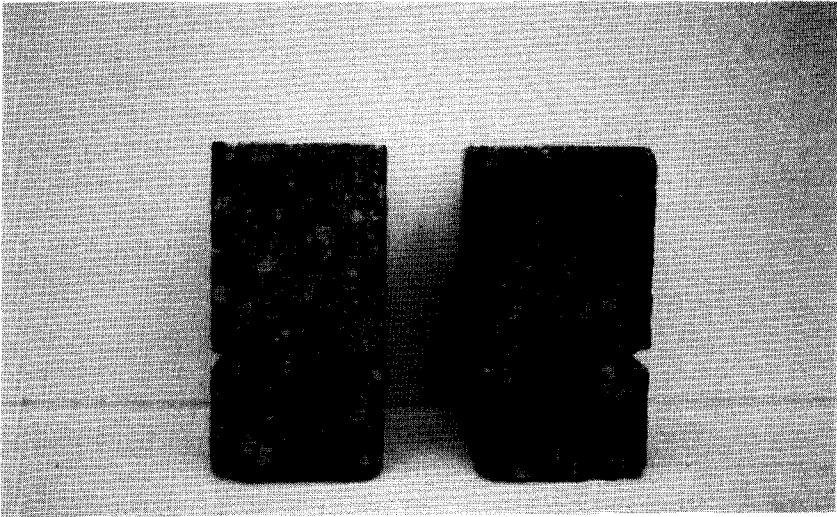
Figure 5.7 Specimens of high and low quality concrete.

It should be noted that the experimental programme was performed before the theoretical model was extended to biaxial loading conditions and a strength drop was predicted at about 0.3 f_c..

To examine the influence of concrete quality, a high and a low quality concrete were tested. The qualities are denoted as Mix A and Mix B, respectively. Figure 5.7 shows specimens of the high and low quality concrete and the difference in heterogeneity. In the original plan, static and dynamic experiments should be performed on specimens with a notch depth of 5 mm. During the first experiments at high compression levels,

the 5 mm notch appeared to be insufficient to fix the location of the final failure plane. In spite of the increase of the loading rate and the possible influence on strength, the notch depth had to be increased to 7 mm. Due to this change, the static programme had to be cancelled.

An overview of the performed experiments and the test programme is given in Table 5.1. Getting ahead of the experimental results, the loading rates of the tests are also listed in the table. They appear to be in the range where the influence of the notches on the response and final strength have to be expected.

Table 5.1   The test series and test conditions

Compression level		0%		50%	75%	100%
Notch depth [mm]	0	5	7	7	7	7
Mix A		A5	A7	A50	A75	A100
Loading rate [GPa/s]		17.7	12.0	15.0	13.4	-
Number of tests	5	6	12	12	7	
Mix B	B0	B5	B7	B50	B75	B100
Loading rate [GPa/s]	10.0	13.7	13.4	10.8	11.0	-
Number of tests	3	4	8	8	11	8

5.5   Material properties

The rate sensitivity of concrete depends on material quality. For this reason, a high and a low quality were tested in the experimental programme. The high quality concrete (Mix A) corresponded with the quality of the former test series at the DUT, e.g. [125] and [120]. The other series (Mix B) had a low quality cement matrix to realize a clear difference between both mixes. The compositions of both mixes are given in Table 5.2. The cement type was Portland cement type III (B).

It should be noted that the heterogeneity and the porosity in Mix B were high, while the quality of the matrix-aggregate bond surface was low due to the small cement content.
The prismatic specimens were sawn from plates with dimensions 50x290x320 [mm3]. These plates were cast in vertical position. Nine specimens of 50x80x100 [mm3] were obtained from each plate. The four sawn surfaces form the faces which are loaded in the biaxial device. These surfaces were polished afterwards to realize planparallel load surfaces.

Table 5.2 Concrete composition

Mix	cement content [kg/m³]	aggregate content [kg/m³]	water cement ratio [-]	air content [%]
A	375	1820	0.5	2.1
B	200	1950	0.62	2.5

Mix	aggregate grading [%]			(diameter in [mm])		
	<0.25	0.25 - 0.5	0.5 - 1	1 - 2	2 - 4	4 - 8
A	7.0	13.0	15.0	15.0	20.0	30.0
B	10.7	7.9	11.2	15.9	22.5	31.7

Companion specimens were cast for each mix:
-      12 cubes   (150 mm) for compressive tests
-      12 cubes   (150 mm) for splitting tests
-       9 cylinders   (Ø 150, height 400 mm) for compressive tests.
Demoulding of plates and control specimen took place after two days. After demoulding they were stored for two weeks at 100% relative humidity. The test specimen were cut with a slow-feed diamond saw and, together with the control specimen, stored in the test room (20°C, 60% relative humidity).
The control tests were performed after 28, 56, 112 and 167 days, while the (biaxial) test series were performed during the last period, i.e. 120 - 167 days. The mechanical properties after 112 days are given in Table 5.3.

Table 5.3 Mechanical properties, strength values and Young's moduli

Mix	cube strength f_{cu} [MPa]	splitting strength f_{spl} [MPa]	cylindrical strength f_{ccyl} [MPa]	tensile* strength f_t [MPa]	Young's modulus [GPa]
A	51.7	3.22	35.2	2.98	33.9
B	29.5	1.76	19.4	1.63	30.9

*   The tensile strength is related to the splitting strength by the relation $f_{ts} = 0.925 \, f_{spl}$.

6   UNIAXIAL TESTS

This chapter presents the data on impact tensile strength, deformation capacity and fracture energy. The main differences in relation with former test programmes are the application of notches and the recording of the deformation of the single failure zone. The set-up offered the opportunity to reconstruct the failure process during the impact tests. The reconstruction of one test series will be described to show the role of the structural response and to give a good background to interpret the data.

The test results will be used to propose an expression for the fracture energy of a single fracture zone under impact loading.

A more extensive presentation and discussion of the uniaxial impact tests are given in [120]. Figure 6.1 shows some stages of the uniaxial testing procedure.

6.1   Tensile strength

6.1.1   Test data

Using the definition of material strength as the maximum load the material can resist, divided by the cross-section area, the transmitted pulse gives explicitly the information on the dynamic strength. With the recorded pulse, the loading rate, $\dot{p}$, impact strength, f_{td}, and the occurring scatter expressed in the coefficient of variation, were calculated as listed in Table 6.1. In addition to this commonly applied procedure, the geometry of the notched specimen offers the opportunity to calculate the strength using the elastic concrete response outside the fracture zone to quantify the loading the material in the failure zone could resist. The restriction is a known value for dynamic Young's modulus, E_{dyn}. Previous research resulted in the empirical CEB-FIP formula [16].

$$\frac{E_{dyn}}{E_{stat}} = \left(\frac{\dot{p}}{\dot{p}_o} \right)^{0.016} \tag{6.1}$$

with $\dot{p}_o = 0.1$ MPa/s.

When this equation is used to quantify E_{dyn}, and under the assumption that the elastic response beyond the failure zone represents the "transmitted pulse", the strength data are obtained as listed in Table 6.1 and denoted as $f_{td}{}^{*}$. The other values for the dynamic strength, listed in this table, are the empirical value, $f_{td,emp}$, from former programmes at the DUT, and the predicted strength, $f_{td,mod}$, using the model described in Chapter 3.
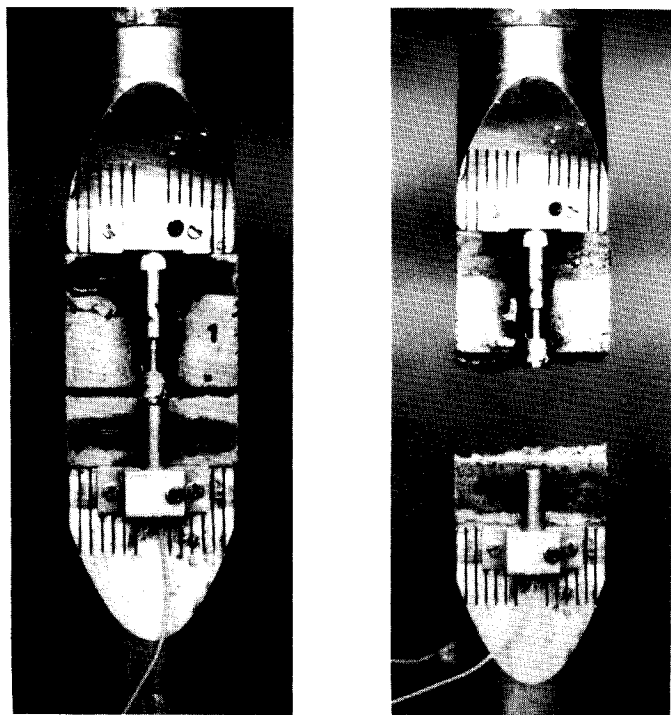
Figure 6.1 Some stages of uniaxial testing procedure.

Tabel 6.1 Strength data

Series	$\dot{p}$ [GPa/s]	f_{td} [MPa]	c.v.(f_{td}) [%]	f_{td}*# [MPa]	$f_{td,emp}$ [MPa]	$f_{td,mod}$ [MPa]	PSI f_{td}/f_{ts}
A5	17.7	4.44	5.2	3.83	4.9	4.7	1.49
A7	12.0	3.93	5.0	3.62	4.9	4.7	1.32
B0	10.0	2.69	4.8	- ##	2.7	3.3	1.65
B5	13.7	2.45	8.9	2.70	2.7	3.3	1.50
B7	13.1	2.74	11.8	2.69	2.7	3.3	1.68

\# E_{dyn}-values are 40.7 and 37.1 [GPa] for Mixes A and B respectively.

\#\#   Fracture zone coincided the zone of strain measurement.

6.1.2   Loading conditions

Before the strength data are discussed, the loading conditions, presented in the first column of Table 6.1, need some comments. Analysis of the incident and transmitted pulses showed that the differences in loading rates were mainly caused by variations in the generated loading pulse. Nevertheless, after adjustment for this variation it appeared that the observed loading rate decreased with increasing notch depth and decreasing concrete quality. The latter result is reasonable, the dispersion of the loading pulse will be larger in the more heterogeneous, low quality concrete. The other result was unexpected, at constant loading rate, reduction of the cross-section should lead to an increasing loading rate. An opposite tendency was observed, in spite of the 10% reduction in cross-section, the loading rate in the net section of the A7-series was just 102% of the A5-series, while the loading rate in the B7-series was only 98% of the B5 results. The differences are not large, but they indicate that the application of the notches affected not only the strength, but also the pre-peak fracture process, see 6.2.

6.1.3   Influence of notches

The first conclusion that has to be drawn from the strength data is that the impact strength was affected by the application of notches in the case of the high quality concrete but not for the low quality concrete.
Considering the difference in material quality for both series and the low strength of the A7-specimen, the most probable explanation of the results is the sensitivity to stress concentrations which occurred due to the applied notches. In the low quality concrete, apparently the high level of heterogeneity enabled sufficient crack arrest for the redistribution of stresses. For the A-series, the redistribution was insufficient and the high stress levels adjacent to the notches caused early failure. That the application of notches and early failure do not have to be coupled necessarily to brittle failure will be shown in section 6.2. and is indicated already by the observed loading rate.
Concerning the biaxial tests, it is expected that the notch sensitivity will decrease with the increasing level of compression.

These test results gave some information on the notch sensitivity of concrete. The notch sensitivity depends on initial heterogeneity and rate of sufficient micro-cracking which in its turn is related to the loading rate. The last two aspects have been coupled in a simple model [120] to estimate the influence of loading rate and notch depth on the specimen strength. The model is based on the comparison of the extension rate of the zone in which the stresses exceed the limit of micro-cracking and the extension rate of the zone of sufficient micro-cracking. The first extension rate followed from the stress distribution, using LEFM relations, and the loading rate. The rate of micro-cracking is an unknown parameter. Data on crack extension in the pre-peak fracture process of micro-cracking is very scarce. The only available data was presented by Shah and John [87] as a logarithmic dependency between pre-peak crack rate and loading rate. In the range up to 10 [GPa/s], the crack velocity increased from 0.001 to

80 [m/s]. When the test results of the A-series were used to calculate the unknown extension rate of sufficient micro-cracking, the value was 40 [m/s].

Application of the model and the order of magnitude for the velocity of 50 [m/s], notch sensitivity appears to occur for loading rates where the internal inertia effects become important for the failure process. The model for crack extension in the fictitious fracture plane showed that the inertia effects are responsible for the steep strength increase beyond loading rates of 10 [GPa/s]. The relation between both results is reasonable, in the case of the strength increase, inertia effects delay crack extension and thus the failure process. In case crack extension is needed for the redistribution of stresses, the inertia effects will cause early failure and notch sensitivity will increase.

6.1.4   Material strength

The strength data of the B-series fit very well with the results of former research programmes at the Delft University of Technology (DUT). The former studies, e.g. [124], resulted in an empirical formula for the impact tensile strength. For mixes A and B this relation is given by, respectively

$$A: \quad \ln(f_{td}) \quad = \quad 1.48 + 0.042 \ln(\dot{p}) \tag{6.2}$$

$$B: \quad \ln(f_{td}) \quad = \quad 0.88 + 0.042 \ln(\dot{p}) \tag{6.3}$$

with the loading rate $\dot{p}$ expressed in [GPa/s] and the strength f_{td} in [MPa].

Because these former tests were performed on un-notched specimens, these former programmes included tests on concrete with the same properties as Mix A has, and because of the good correspondence with the B-data, the empirical relation will be used as the reference for the dynamic material strength.

In section 5.3.1. the introduced error in SHB testing due to non-linear effects and the specimen size was mentioned. The dynamic strength could be overestimated with utmost 5%. The listed values $f_{td}^{\star}$ in Table 6.1 do not give a definite answer on the introduced error in the current tests, because the empirical formula for dynamic Young's modulus is an average result for all kinds of concrete and testing methods, including SHB testing. Nevertheless, a comparison of f_{td} and $f_{td}^{\star}$ is worthwhile. For the A-series the f_{td} shows about a 10% higher value than $f_{td}^{\star}$. The B-series, however, shows an opposite feature which could not be explained based on the recordings.

Based on these numbers it cannot be recommended to use the elastic strain measurements outside the fracture zone and the empirical Young's modulus to derive a more accurate strength and loading rate for notched specimens.

Finally, it is promising that the model prediction of the rate effect for the high quality is within 5% accuracy of the, empirical, material strength. The prediction is based on the static material properties and concrete composition, no dynamic test data are used

to fit the result. For the B-series, this resulted in an overestimate of the change in fracture energy demand and a 20% too high dynamic strength. Referring to the description of the model and the failure mechanisms, the overestimate shows that the transition from bond to aggregate fracture is not only a function of loading rate but also of parameters as heterogeneity and initial fraction of bond fracture.

6.2   Structural response

The features of material response are best presented in the relation between loading and deformation. The applied measurement set-up made the derivation of this relation for the specimen response possible, which is the combination of material and structural response. Analysis of the test results showed that the structural response had an important influence on the failure process and deformation data. Therefore, a reconstruction of the failure processes for the A-series is given in this section. It forms a background for the discussion of the deformation and fracture energy data and it illustrates the complex failure process during a simple impact test.

6.2.1   Response of A5-series

The average response of specimen and fracture zone are depicted in Figure 6.2. The response curve of the fracture zone shows the common feature of elastic deformation and just before the top the pre-peak fracture process causes some minor deformation. The fracture energy is determined by the post-peak fracture process corresponding to the Hillerborg approach. In most cases the failure process was not symmetrical, which is shown in the last graph of Figure 6.2.

These deformations show that at the rear face, the pre-peak fracture process was more pronounced, while at the front face, no fracture process was observed at all. The failure process was asymmetric which was also seen clearly in the elastic response outside the fracture zone. The recordings depicted in Figure 6.3 show the failure process in more detail. The sequence was as follows. At t = 2.9 [ms] the pulse arrived and the response was linear elastic. At t = 3.04 [ms] non-linear deformation occurred at the rear face, which emerges from the δ_{frac}-t diagram and is reflected as a deviation of the elastic responses in the δ_{elast}-t diagram. The load level at this moment, see Figure 6.2, was σ_{net} = 2.57 [MPa]. After 0.16 [ms] non-linear deformations also occurred at the front face while the load was increased to 3.60 [MPa], which was slightly below the maximum load of 4.13 [MPa]. From this sequence it emerges that the onset of non-linear deformations at the rear face was followed by continuing stress increase. Apparently the material in the zone of stress concentration was not yet loaded up to its strength. From the elastic deformation curve it emerges that just at t = 3.125 [ms] the material in this zone failed and reached the softening branch. This implies that during the time interval, t = 3.04 - 3.125, redistribution of stresses was possible reducing the effect of the notch on the specimen strength. The total deformation curves show that the deformation rate at the front face decreased as soon as the material at the rear face reached the softening branch. Additionally to the translation, rotation occurred

resulting in some failure delay at the front face. The rotation process, which starts just before maximum load, continued more pronounced in the softening branch of the specimen response.
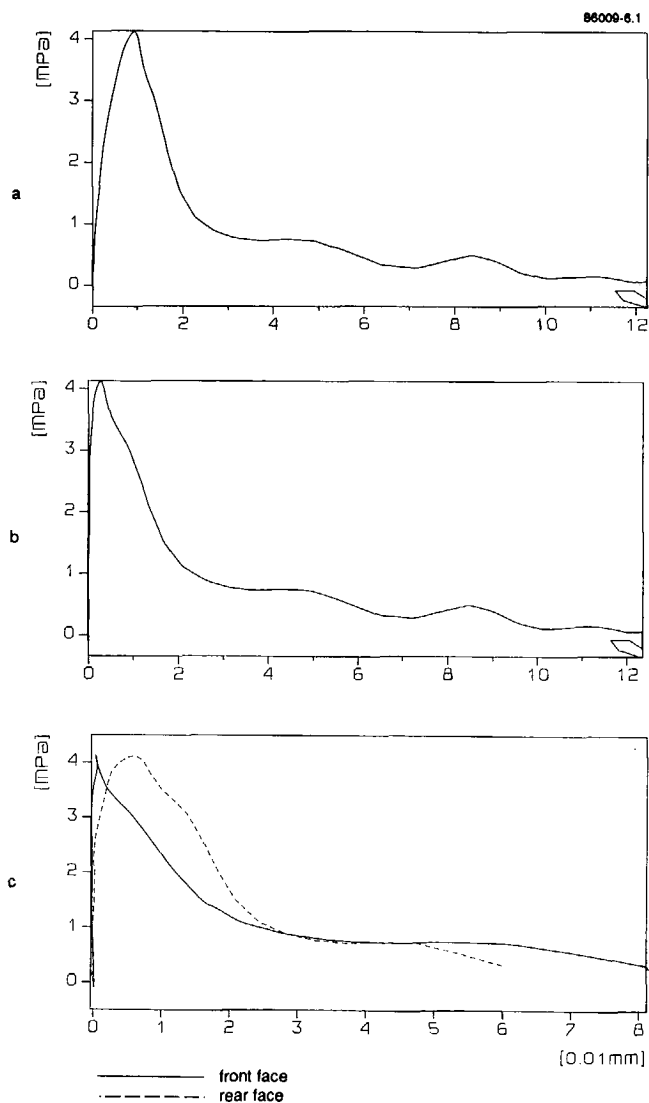
a) Mean, total deformation
b) Mean, deformation of fracture zone
c) Deformations of fracture zone at front and rear face

Figure 6.2   The load-deformation curves for the A5-series.
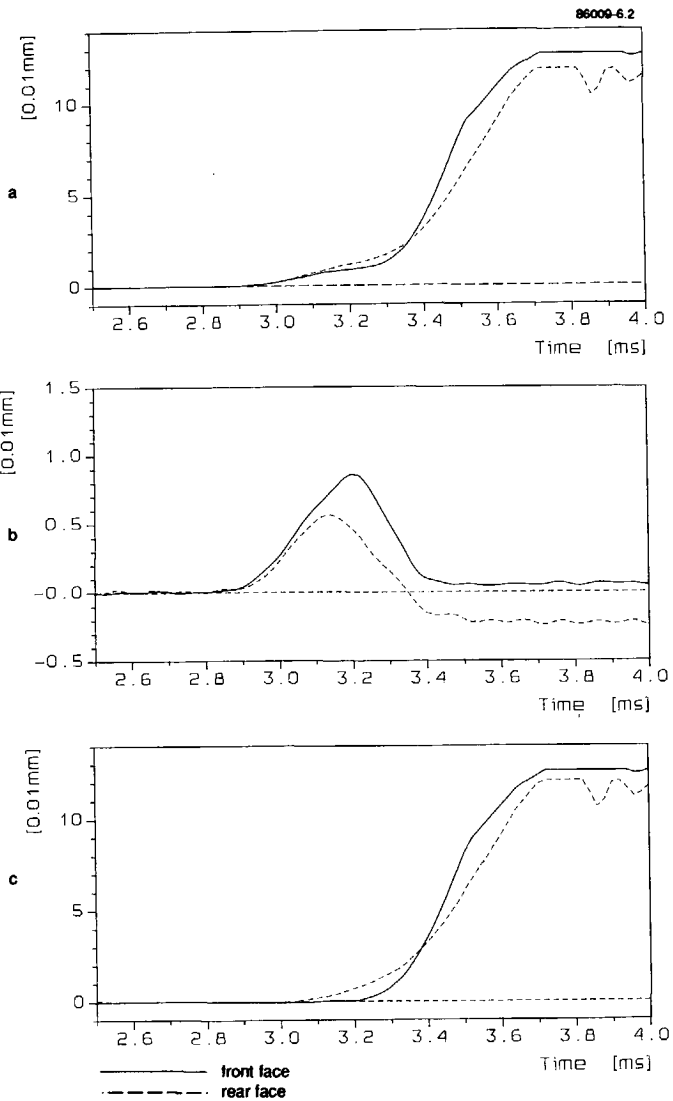
a) Total deformation
b) Elastic deformation
c) Deformation in fracture zone.

Figure 6.3   The deformations in the A5-tests at the front and rear face as a function of time.

Considering the failure process, it emerges that after the specimen started to fail, the major part of the impinging pulse was reflected by the softening fracture zone. The transmitted pulse, which is per definition the true loading pulse, only slightly increased. The equilibrium was formed by the resistance of the material and the activated inertia due to the deformation rate. In this final stage, the point of rotation was located at the front side resulting in an apparent brittle failure of the material. At this face, the moment of non-linear deformation coincided with the onset of softening because no stress redistribution could occur.

6.2.2   Response of A7-series

Similar to the presentation of the A5 results, Figure 6.4 gives the load-deformation curves for the specimen response for the A7-series. Striking are the pronounced pre-peak fracture process and the symmetric response.
In contrast to the response in the A5-series, non-linear response started at both sides and at a low load level, i.e about 30% of the specimen strength. The graphs in Figure 6.2.4 show the symmetry in elastic and plastic response. This symmetrical response remained up to t = 5.18 [ms] at a load level of 3 [MPa]. At that moment the material at the rear face reaches the softening branch and additional rotation occurred. The evidence for the rotation is given by the sudden decrease of deformation rate at the front face, see Figure 6.5c. Due to the stress concentrations and already significant level of non-linear deformation at the front face, the residual resistance of the specimen to a load increase was minimal. The material at the front face reached the softening branch at t = 5.22 [ms].

In comparison with the A5-series, the rotation is much more pronounced, which caused a definite failure delay at the front side up to t = 5.33 [ms], see Figure 6.5b. At the rear side the deformation of the fracture zone is accelerated by the rotation process. The asymmetric response during the softening phase is clearly shown in the load-deformation curves of Figure 6.4c.

The failure sequence of the A7-series show the existence and importance of the pre-peak fracture process for the response of plain concrete specimen more clearly than the A5 results. The deep notches caused high stress levels in the material and the onset of failure at low load levels. The observed additional strength can be attributed to inertia effects or to the pre-peak fracture process and stress redistribution. The numerical simulation of the A7-tests, performed by Sluys [92] without a pre-peak non-linearity for concrete response, showed that inertia effects were not responsible for the observed response. The simulation showed failure of the specimen almost as soon as the material next to the notches reached the softening branch, see 6.5. Therefore, the observed non-linear response must be attributed to the property of concrete response, a pre-peak fracture process.

Finally it is mentioned that the rotation process as observed in the impact tests is similar to that observed in deformation controlled, static tensile tests, see the work of Hordijk [34] and Rots [83].
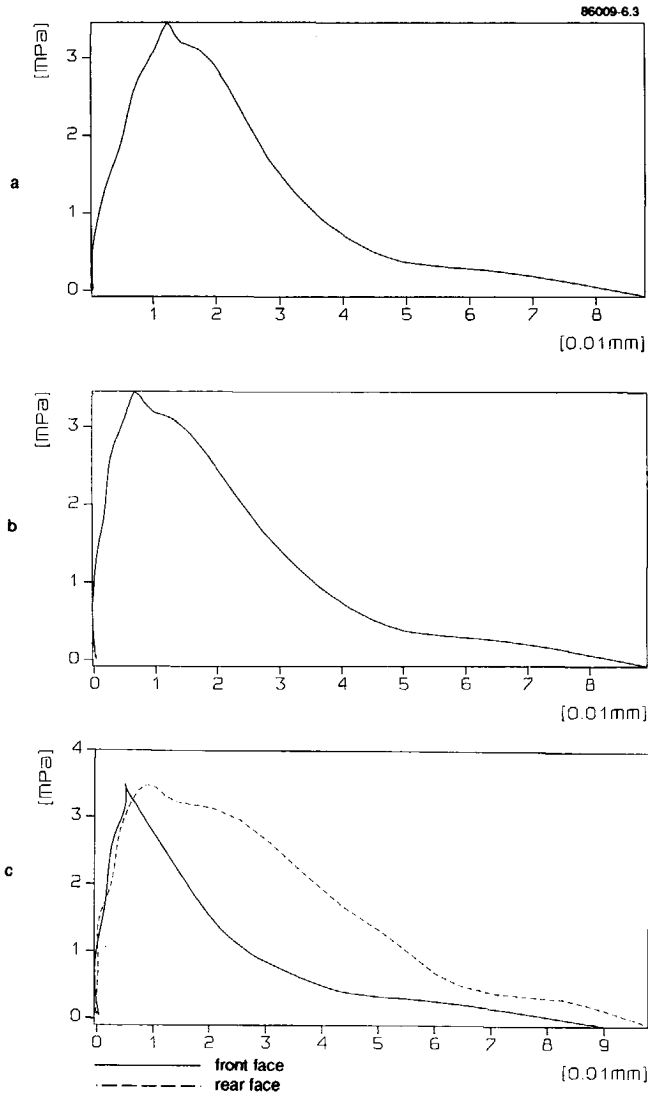
86009-6.3

a) Mean, total deformation
b) Mean, deformation of fracture zone
c) Deformations of fracture zone at front and rear face

Figure 6.4   The load-deformation curves for the A7-series.
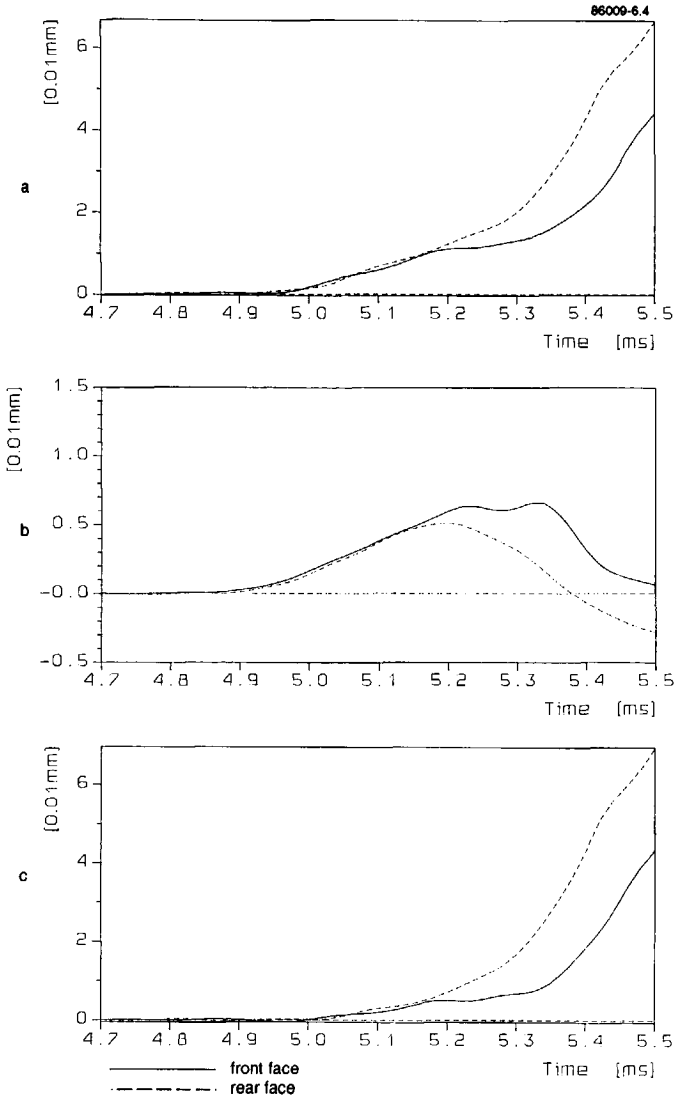
a) Total deformation
b) Elastic deformation
c) Deformation in fracture zone.

Figure 6.5   The deformations in the A7-tests at the front and rear face as a
function of time.

6.3 Deformation capacity and fracture energy

One of the objectives of the uniaxial impact tests was to gather data on the deformation capacity and fracture energy for a single failure zone. The applied notches and the measurement set-up were dedicated to get this information. The load and deformation were recorded independently and had to be related afterwards. The results and discussion given in the former sections showed that the shape of the load-deformation curve constructed is affected by the structural response and the disynchronization. These aspects will be taken into account in the interpretation and discussion of the data on deformation and fracture energy.

6.3.1 Experimental data

The measurement set-up and the geometry of the specimen enabled us to determine the deformation of the whole specimen and the deformation of the single fracture zone itself. The load-deformation curves for the various series are given in the Figures 6.6 and 6.7. The data is listed in Table 6.2. To indicate the various parameters and response stages, the following notation is used.

- maximum strain outside the failure zone, ε
- total deformation at maximum stress, $\delta_{tot,top}$
- deformation of fracture zone at maximum stress, $\delta_{frac,top}$
- maximum recorded deformation, δ_{max}
- sum of deformation energy and fracture energy at maximum stress, $G_{tot,top}$
- fracture energy at maximum stress, $G_{f,max}$
- fracture energy at maximum deformation, G_f

Table 6.2   Experimental data

Series	ε [10^{-6}]	$\delta_{tot,top}$ [0.01 mm]	$\delta_{frac,top}$ [0.01 mm]	δ_{max} [0.01 mm]	$G_{tot,top}$ [N/m]	$G_{f,max}$ [N/m]	G_f [N/m]
A5	68.3	0.91	0.26	12	26.3	10.1	101
A7	58.0	1.14	0.65	9.5	26.7	16.5	99
B0	-#	1.74	-	> 9.2 ##	26.9	-	112
B5	58.2	0.91	0.38	> 12.6 ##	15.5	9.0	71
B7	47.9	0.98	0.53	> 9.3 ##	17.2	10.8	73

\#   Fracture occurred in the zone of strain measurement

\#\#   The numbers correspond with the maximum range of transducer-amplifier for the series. Extrapolation leads to an estimate of the maximum deformation of 14, 14 and 13 [0.01mm] respectively.

a) A5, δ_{tot} c) A7, δ_{tot}
b) A5, δ_{frac} d) A7, δ_{frac}
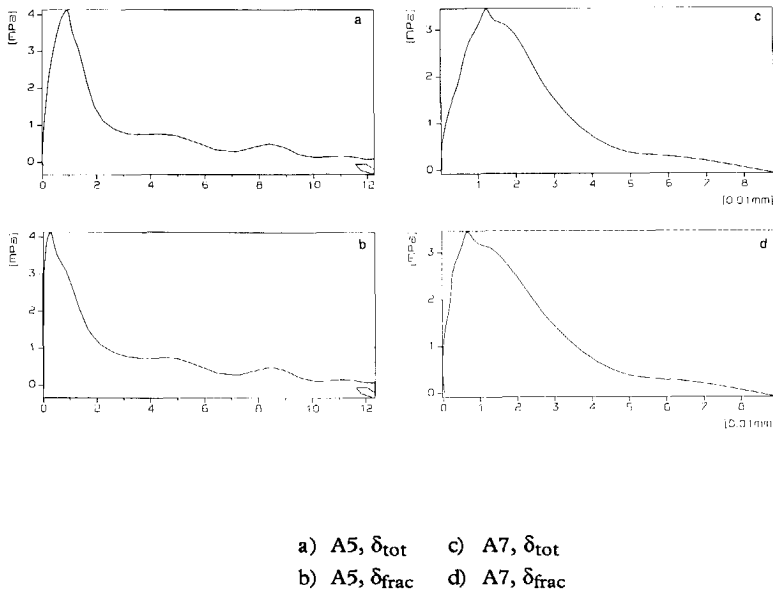
Figure 6.6   The load-deformation curves for the whole specimen and the single fracture zone, the A-series.

Before the response data are discussed, first some comments to enlighten three aspects. First, the B-series show the influence of the measuring length. In the B0-series the measuring length equalled the specimen height, just as in the former research programmes at the DUT. The observed deformation, $\delta_{tot, top}$, corresponds with the reported deformation of 0.015 mm by Körmeling [49]. Because no notches were applied, fracture could occur over the whole measuring length.

In the other series, the fracture process was concentrated in the zone of reduced cross-section. Comparison of the values of the pre-peak total deformation, $\delta_{tot, top}$, show that the deformation in the B0-series was larger than for the notched specimen. As the strength was the same for all the B-series, the large deformation in the B0-series must have been caused by multiple fracture, which phenomenon was also observed in the former programmes of the DUT [124] and is reflected in the shape of the softening branch.

This emphasizes the importance of a measuring length corresponding to the width of the fracture zone. For dynamic loading there is the additional demand for the definition of the width of the fracture zone. In the current programme, the width is limited and multiple fracture, which is a structural response effect, is excluded by the application of the notches.

Concerning the B0-series and the results of the former programmes it was concluded that multiple fracture obscured the data of the deformation capacity and led to an overestimate.

a) B0, δ_{tot}
b) B5, δ_{tot} c) B5, δ_{frac}
d) B7, δ_{tot} e) B7, δ_{frac}
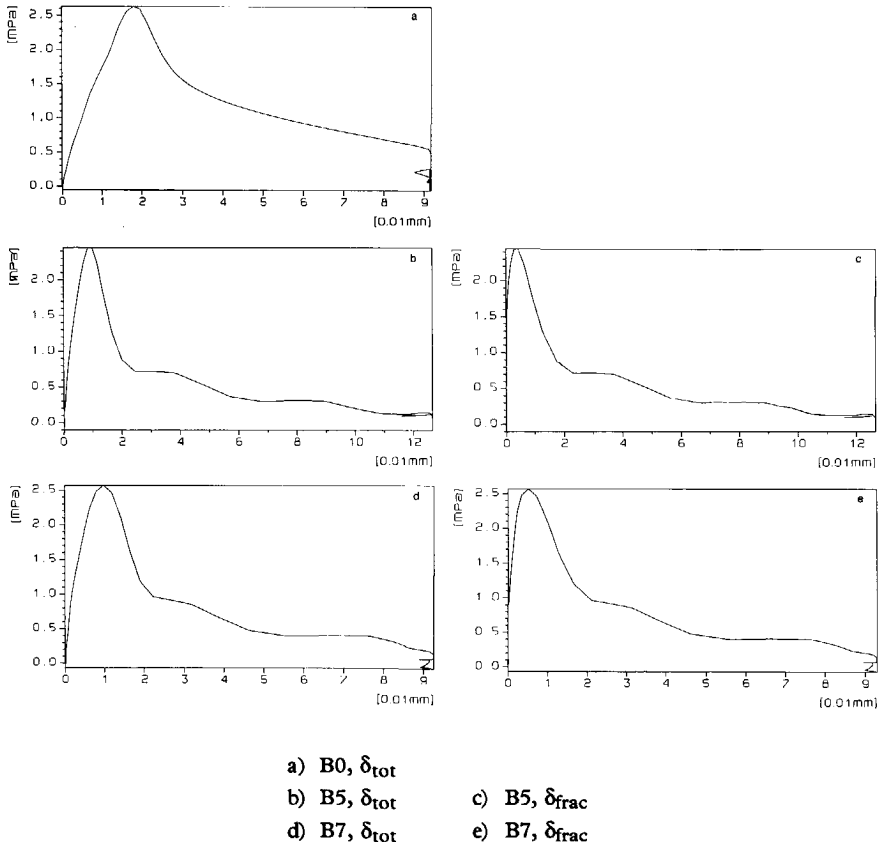
Figure 6.7   The load-deformation curves for the whole specimen and the single fracture zone, the B-series.

The second aspect is the increasing, pre-peak deformation with increasing notch depth. The strength data showed that, for the A-series, the notches led to early failure. The structural response, as described in 6.2, showed that this early failure was not coupled to brittle behaviour. The pre-peak fracture process was activated to neutralize the stress concentrations. The stress redistribution, however, was insufficient to prevent failure below the true material strength.

The third aspect concerns the derived fracture energy. The descending branch of the response forms an unstable equilibrium between supplied and dissipated energy. The SHB equipment is a uniaxial equilibrium system, in which the transmitted pulse

loaded the material. The combination of the loading pulse and the non-elastic deformation of the specimen gives the dissipated energy in the fracture zone. The shape of the load-deformation curve might be affected but the G_f value represents the fracture energy of the material. The constant value of G_f, at different structural responses, supports this statement.

6.3.2   Deformation capacity

Concerning the post-peak deformations, the load-deformation curves give the most information. The notched specimen shows a rather steep drop beyond the peak, followed by a moderate response giving the curve its long tail as is known from static tests. Only the A7-series with its pronounced rotation process, section 6.2, and the B0-series with multiple fracture show a more continuous softening branch.
The values δ_{max} are all of the same magnitude, except the low A7-value. Related to static data, the numbers for the deformation capacity are rather small. The conclusion of a lower deformation capacity under dynamic loading is in contradiction with the common opinion. Therefore a thorough analysis is necessary. It is emphasized again, that the structural response had an important influence on the observed softening behaviour. Moreover, the disynchronization of load and response measurements have affected the shape of the load deformation curve. These facts oppose a quantification of the deformation capacity of concrete. Some tendencies, however, can be derived.

For the analysis, the A7 and B0 results are neglected because of the dominant structural response effect. The available data on uniaxial, dynamic tensile tests concern the former impact tests at the DUT on specimens without notches. Therefore, the response in static, deformation controlled tests is considered to be the best reference for the dynamic response of a single fracture zone.
The static response also shows the feature of two stages, the steep decay is followed by a gentle strength decay, or better resistance decay, with increasing deformation. Various mathematical expressions for this behaviour were proposed in literature. Rots [93] proposed a bilinear expression, Reinhardt proposed a more gentle shape given by a power function [77] and later by an exponential expression [78]. Because of their simplicity, the bilinear and power expression were used in the comparison with the dynamic results. The expressions are:

$$\frac{\sigma}{f_t} = 1 - \frac{8\,\delta_{trans}}{\delta_{max}} \qquad \text{first branch}$$

$$\frac{\sigma}{f_t} = \frac{1}{3} - \frac{4\,\delta_{trans}}{11\,\delta_{max}} \qquad \text{second branch}$$

$$\frac{\sigma}{f_t} = 1 - \left(\frac{\delta}{\delta_{max}}\right)^{k} \qquad \text{power function}$$

with δ_{trans} the deformation at the transition point of both branches.

The average values under static loading are:

$$d_{max} \quad = \quad 12\text{-}20 \, [0.01mm]$$

$$d_{trans} \quad = \quad 1/12 \, d_{max} \, (= 1\text{-}1.7 \, [0.01 \, mm])$$

$$s_{trans} \quad = \quad 1/3 \, f_t$$

$$k \quad = \quad 0.2 \text{-} 0.4$$

Some comments on the maximum deformation:

The dynamic values of δ_{max} were rather small. Considering the synchronization aspect, it might be expected that during the descending branch the actual load level is overestimated, especially in the part of moderate decay.

More significant is the influence of the inertia effects. The contribution of inertia in the force equilibrium will increase due to the acceleration of the deformation rate in the fracture zone. Therefore the transmitted pulse is the sum of material resistance and inertia forces. Again the material response is mixed with other effects, see also 6.4 numerical simulation.

Especially due to the inertia effects, the observed maximum deformation is an upper limit for the true deformation capacity of the material.

The maximum deformation is the integrated deformation in the fracture zone. If the width of the zone and the amount of micro-cracking in this zone are not affected by the loading rate, δ_{max} would be the same for static and dynamic loading. The tendency of the decreased deformation capacity indicates that they were affected. The objection because of the applied notches is refuted by the results of the low quality concrete in which the notch effects were neutralized at maximum load.

Considering the data on the fracture energy more insight in the geometry of the fracture zone is obtained.

6.3.3   Dynamic fracture energy for single fracture zone

The deformation data indicated a reduced deformation capacity at high loading rates when a single fracture zone is considered. The G-values at maximum stress show the same feature as the deformation data, i.e. multiple cracking in the B0-series and the structural response in the A7-tests resulted in large values for G. Most remarkable is the constant value of G_f for the single fracture zone in the different modes of structural response. It shows that the failure mechanism of the material itself was not affected by the structural response. This enables a comparison with static data. When the power function is used to characterize the static load-deformation curve, the fracture energy G_f is given by the following expression, with k as a parameter to characterize the softening branch.

$$G_f = f_t \cdot \delta_{max} \cdot \left(\frac{k}{(1+k)}\right)$$

with k = 0.2 - 0.4

δ_{max} = 0.12 - 0.2 [mm]

Using the values $\delta_{max}=0.18$[mm] and $k = 0.3$ results in $G_f = 125$ and 66 [N/m] for Mix A and Mix B, respectively. Including a more ductile response for Mix B, $k = 0.4$, G_f equals 82 [N/m]. Mix A corresponds with the concrete tested by Zielinski and Körmeling. The latter reported a static G_f value of 22 at maximum stress and 116 [N/m] at δ_{max} [50]. It should be noted that Körmeling used notched specimens in some of his tests, but did not record the elastic deformation. Consequently, he had no additional reference for synchronization and applied a measuring length of 100 [mm]. Körmeling did not report on the consequences of the application of notches.

Comparison with the dynamic data, Table 6.1, shows that the fracture energies are of the same order of magnitude. Due to the testing technique the G_f values are rather an upper limit than a lower limit for the material response. Therefore, the conclusion is that the fracture energy does not increase with increasing loading rate. This result for the single fracture zone is contrary to the common opinion on material response.

Listing the test results gives:

-   dynamic material strength corresponds to the data in literature;

-   dynamic deformation of the fracture zone is smaller than reported in literature and even shows a tendency to be smaller than under static conditions;

-   dynamic fracture energy is unique for each mixture and is definitely smaller than reported in literature, and of the same order of magnitude as the static fracture energy.

Or in summary, rate effects lead to higher strength but the failure process becomes more brittle. This observation corresponds with the experimental results reported by Shah and John [86] in the notched beam experiments.

The results on the fracture energy and the strength are rather confusing. When the G_f value is the same for static and dynamic loading, the conclusion could be drawn that the failure mechanism and fracture process is not affected by rate effects. But this contradicts the fact that the rate dependency of the strength can be explained and modelled by considering the changing geometry of the fracture plane and thus a changing energy demand in the pre-peak fracture process, see Chapter 3. From the test data it appears that these observations for the tensile strength may not be extended to the macro-cracking process given in the softening branch. Consequently, the well-known rate dependency of the tensile strength may not be applied to characterize the

rate effects for the fracture energy, not even for moderate loading rates up to 10 [GPa/s].

These facts and observations are combined in the following reasoning:

- The dynamic G_f values did not differ considerably from static values. Therefore it is stated that for loading rates up to 10 [GPa/s], the fracture energy G_f is constant.

- The pre-peak fracture process, which determines the tensile strength, is affected by a changing energy demand. This energy is characterized by the specific surface energy γ and should be used to characterize the ascending branch of the load deformation relation. The fact of $f_{td} > f_{ts}$ corresponds with $\gamma_d > \gamma_s$.

- The fracture energy G_f represents the dissipated energy in the material around the tips of the macro-cracks. Therefore, G_f is the summation of the energy, characterized by γ, for all the fracture planes in the failure zone.

- Combination of these points leads to the conclusion that the number of fracture planes reduces with increasing loading rate. Or, in other words, the width of the failure zone becomes smaller at higher loading rates and the ultimate crack width, δ_{max}, decreases.

Application to the theoretical shape of the softening branch given by the power function and the empirical strength results of former DUT programmes led to the following expressions:

$$\delta_{max,d} = \delta_{max,s} \cdot \left(\frac{\dot{p}}{\dot{p}_o}\right)^{-0.042}$$

for

$$f_{td} = f_{ts} \cdot \left(\frac{\dot{p}}{\dot{p}_o}\right)^{+0.042}$$

$$\sigma_d = f_{ts} \cdot \left(\frac{\dot{p}}{\dot{p}_o}\right)^{+0.042} \cdot \left[1 - \left(\frac{\delta}{\delta_{max,d}}\right)^k\right]$$

The results are depicted in Figure 6.8.

The base for the proposed dynamic softening relation is only formed by the data of the current programme. The results correspond with the observations of Shah that the deformation capacity of concrete decreases with increasing loading rate. The tendency of a reduced deformation capacity, δ_{max}, at high loading rates was also recently reported by Kobayashi and co-workers on their experiments on double-wedged specimens [120b]. This phenomenon was not observed in former research programmes because of the application of unnotched specimens and long measuring lengths.

Because of the small base, more research specially focused on this subject is necessary to examine the validity of the proposed softening relation.
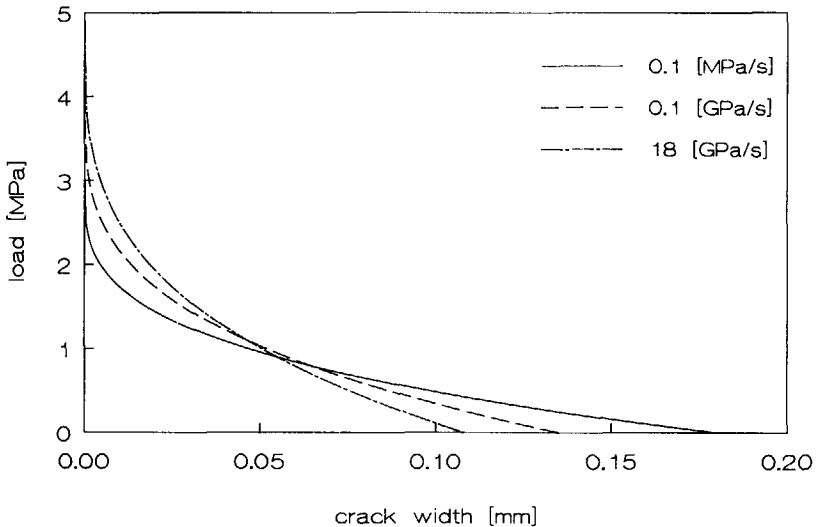
Figure 6.8   Theoretical softening branch for rate dependent deformation capacity of the fracture zone, $\delta_{max,d}$.

6.4   Numerical simulation of impact tests

In the framework of another research programme, the impact tests were simulated by Sluys with the FE-code DIANA. The co-operation offered the opportunity on one hand to examine the features of the numerical algorithm and the applied material model, and on the other hand, to separate material and structural response.
A discussion of the results, limitations and specific problems concerning mesh dependency is not given in this section. These aspects are discussed by Sluys and De Borst in [94, 95 and 96] and in relation to the current programme in [120].
Here, the aspect of structural response, the applied softening model and some general remarks on numerical simulation will be given.

6.4.1   Numerical modelling

The A7-series was selected for simulation. The numerical modelling was performed under the following three main restrictions:

-     The plane stress condition was assumed, while three dimensional effects were present in the tests.

- The numerical scheme for the test set-up differed from the real set-up; the upper and lower bar of the SHB were modelled with the acoustic impedance of concrete.

- Only a rate independent material model was available in which dynamic, but constant, material properties could be included.

The feature of strain-softening leads to an ill-posed system of equations which cannot describe the true physics of material response. In numerical analysis this is reflected in a mesh-dependent behaviour. The best solution is obtained when the dissipated fracture energy in the modelled failure zone equals the fracture energy of the true material. This implies that the input data for the material model, the strain-softening curve characteristics, depend on the element mesh. In the simulation, a coarse and a fine mesh were used. The element distribution is given in Figure 6.9.

86009-6.4.1

a

b

a) Fine mesh
b) Coarse mesh
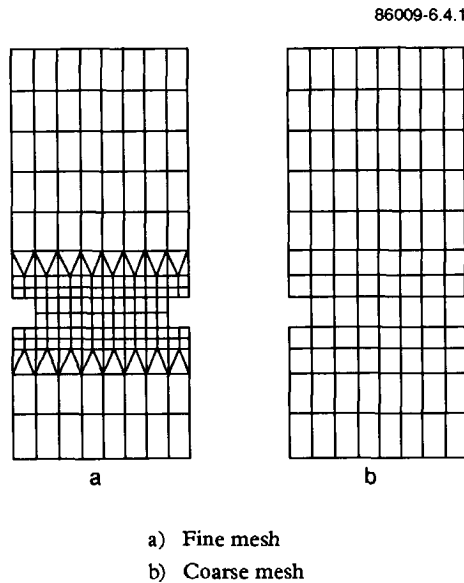
Figure 6.9 The element configuration for the fine and coarse mesh.

The numerical results presented in this chapter are obtained with the fine mesh element configuration, which led to a more brittle response than calculated with the coarse mesh. The more brittle response was obtained due to the classical strain-softening modelling and because the stress singularities at the notch were stronger in the fine mesh.

In a later stage, Sluys simulated the experiments using a rate-dependent softening model which resulted in a mesh-independent solution, except some minor dependency due to the singularity at the notch, see [95].

The constitutive model was formulated within the smeared crack concept [83]. In this concept the dissipated energy and the deformation of the failure zone is spread over a crack band whose size is related to the element configuration. The constitutive model is separated in a linear elastic model for the uncracked material and a softening model for the cracked concrete. No pre-peak fracture is modelled.

Two softening models were tested, i.e. a linear and a non-linear softening model. The latter equals the power function, proposed and discussed in 6.3. Both curves are depicted in Figure 6.10. Note the difference in ultimate strain and the different slope at maximum stress which will affect the stress redistribution process near the notches.

The values of f_{td} and G_f were 4.9 [MPa] and 100 [N/m], respectively.
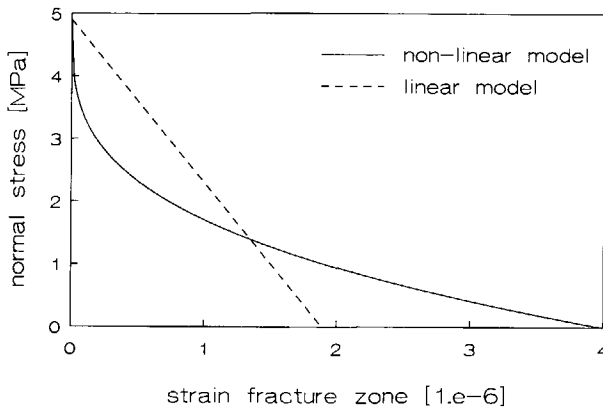
Figure 6.10   The stress-strain curves for the linear and non-linear softening model.

6.4.2   Numerical results

Three aspects of the numerical simulation will be discussed in this section, more information is given in [120] and [94 - 95].

The first concerns the notch sensitivity. Up to maximum stress the size of the influence zone has the same order of magnitude as the notch depth, i.e. 7[mm]. The maximum amplification is about a factor two. The influence of the slope of the softening branch on the process of stress redistribution appeared to be significant. The linear model resulted in an almost equally distributed stress distribution and, consequently, a specimen strength almost equal (95%) to the material strength. The non-linear model enables much less redistribution, resulting in an irregular stress distribution and a lower strength of the specimen, i.e. 80% of f_{td}.

The numerical calculations showed the stress distribution to be non-uniform and changing in time. Initially, the loading rate in the material adjacent to the notches is higher than the rate in the impinging wave. When softening occurs the incident wave is

partly reflected and the loading rate for the material decreases. The condition of uniaxial wave propagation is not fulfilled in the notched geometry. In the case of the linear softening, the regular stress distribution provides the means to analyse the processes of loading and unloading. Application of the non-linear model leads to many more irregularities and complex feature of the response.
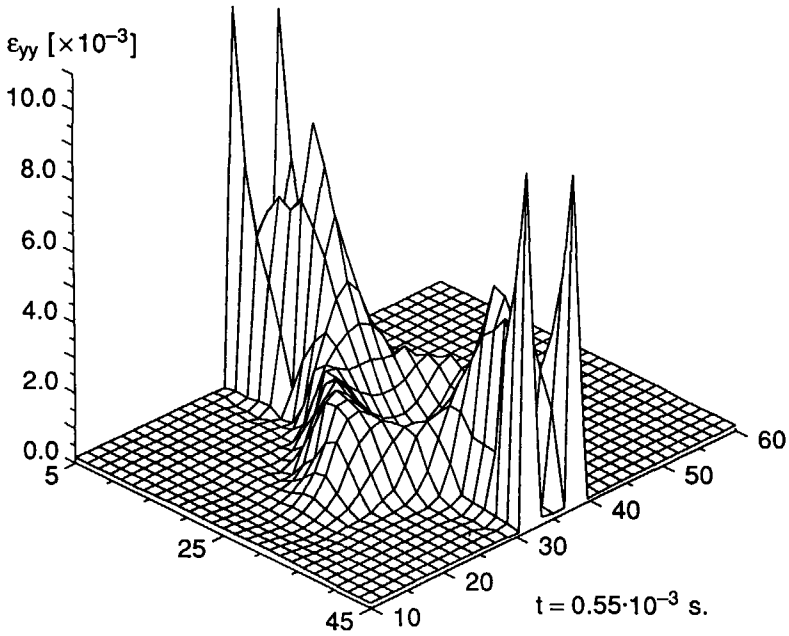
Figure 6.11   The longitudinal strain distribution in the failure zone between the notches, calculated with a rate dependent material model [94]. The scale of the surface plane is given [mm].

More recent calculations [94, 95], with a rate dependent material model, confirmed the irregular stress distribution and showed a non-uniform width of the fracture zone, see Figure 6.11.

The third aspect concerns the contribution of inertia to the equilibrium forces. The calculated stresses are the sum of the material resistance and the inertia forces. Especially during the failure process with large deformation rates, the inertia effects become very important. This is illustrated by the fact that at the end of the failure
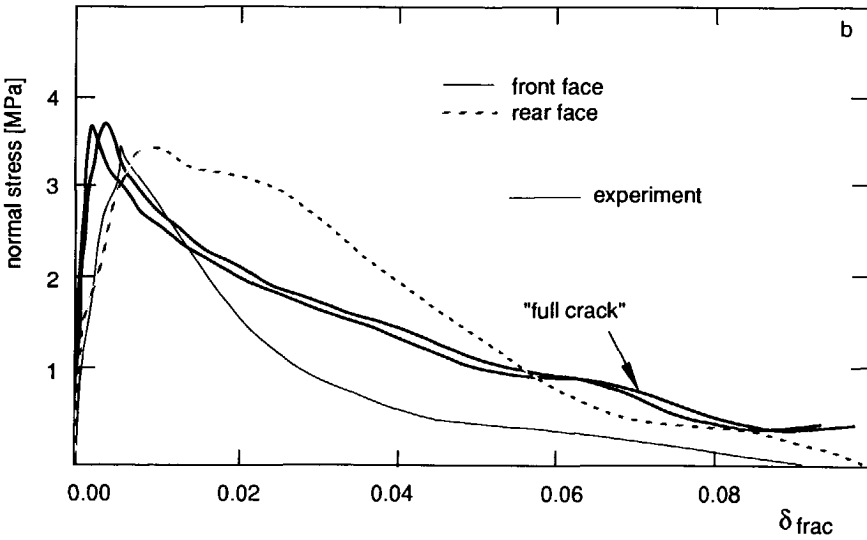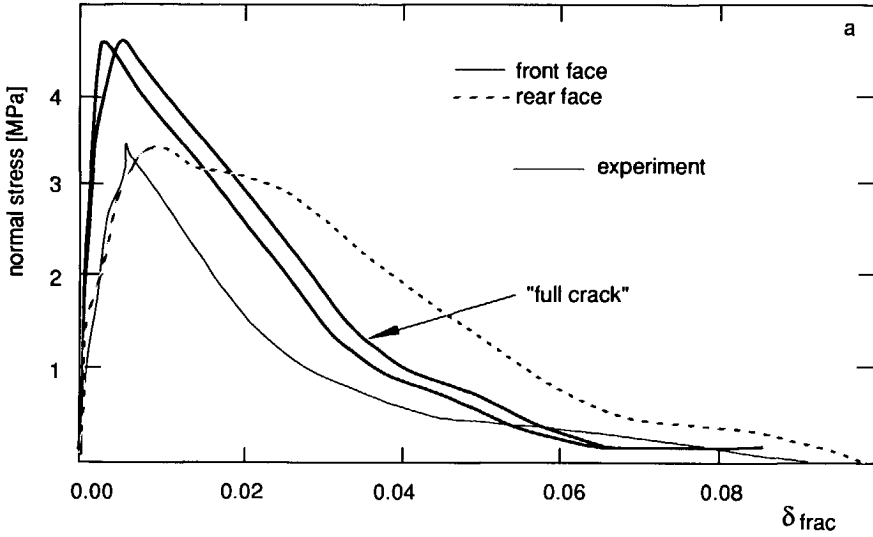
a) Linear softening model; fine mesh
b) Non-linear softening model; fine mesh

Figure 6.12   Stress-deformation curves inside fracture zone.

process, when the resistance of the material is already reduced to zero, the inertia contribution still leads to an observed residual strength beyond the fracture zone. This results in a longer tail of the load-deformation curve when the transmitted pulse

defines the load level. This counts for the numerical simulation as well as for the experiments.

Because the inertia effects within the material are a part of the observed dynamic material resistance, these effects must be attributed to the material properties as long as they are not covered by the numerical simulation itself. In the performed simulation, a part of the inertia effects is covered by the mechanical response due to the small-scale discretisation. Consequently, inertia effects are partly incorporated twice in the calculation.

The first and third aspect are clearly present in the calculated load-deformation curve as given in Figure 6.12. In this figure the test results are depicted as thin solid lines. The most pronounced differences concern the predicted strength, the pre-peak fracture process and the rotation during the softening branch. The latter is probably caused by a too high stiffness of the simplified schematisation of the test set-up. More important is the dependency of the predicted maximum strength from the chosen material model. The failure process, the stress redistribution and the rotation process all depend on the equilibrium of supplied and dissipated energy. Pre-peak fracture occurs in neither material model. Therefore, when the material strength is reached near the notches, the slope of the descending branch determines the rate of energy dissipation and thus the amount of stress redistribution, the capability to rotate and delay the failure process. These aspects are reflected in the predicted load-deformation curves.

In the reconstruction of the response in the A7 tests, the pre-peak fracture process appeared to be decisive for the total response. The absence of the early onset of non-linearity in the numerical simulation confirms the presence and importance of the pre-peak fracture process in the true material response.

The good result of the non-linear model is no proof of the correctness of the proposed power function. Apparently the energy dissipation in the pre- and post-peak fracture near maximum stress, is covered by the shape of the applied non-linear model. The simulation of other experiments is necessary to examine the general applicability of the model.

6.5 Conclusions on the uniaxial impact tests

The results of the uniaxial impact experiments form a thorough reference for the biaxial experiments. The ideal conditions for material testing in the SHB set-up were not fulfilled, on one hand because of the non-linear response of concrete and on the other hand because of the uncommon geometry of the specimen and the application of notches. Nevertheless, reliable data on dynamic strength, deformation capacity and fracture energy were derived from the test data.

Of special interest is the information on the single failure zone. The deformation capacity appears not to increase with increasing loading rate, and also the fracture energy showed the tendency not to increase at high loading rates. The increase of deformation capacity and fracture energy observed in former test programmes must be attributed to multiple fracture and multiple failure zones, which is an aspect of

structural response and should not be incorporated in a material model. The inertia effects inside the material have to be separated from material properties when these effects are covered by the mechanical response in the (numerical) calculation.

The numerical simulation of dynamic material tests offers perspectives for material modelling. The performed simulation showed the sensitivity to the applied material model and the necessity to incorporate the pre-peak non-linearity for the prediction of the dynamic response of plane concrete.

Finally, it is recommended to determine the dynamic fracture energy for concrete for a single failure zone, using notched specimens.

7   BIAXIAL TESTS

The experiments in the biaxial test programme were performed in the set-up as described in Chapter 5. The summarized evaluation of this set-up showed that interaction between the static and dynamic device leads to a complex stress distribution and uncertainties about the contribution of the lateral loading device in the axial equilibrium. The interaction might even dominate the load transfer and specimen response observed.

Due to the uncertainties about load transfer in the dynamic tests, especially during the fracturing process, it becomes impossible to reconstruct quantitatively the load-response curve up to failure. Therefore, the analysis of the biaxial tests was directed to the original objective, i.e. the strength envelope, to examine the influence of lateral compression on the rate dependency of the residual axial impact tensile strength.

7.1   Test programme and test procedure

The experimental programme was mainly focused on the objective given above and it was decided to perform experiments with prestressing levels beyond 50% of the compressive strength. In section 5.4, the experimental programme was presented and the choice of the 50%-threshold was motivated. The test series and test conditions are summarized in Table 7.1.

Table 7.1 The test series and test conditions.

				0%		50%	75%	100%
Compression level				0%		50%	75%	100%
Notch depth		0	5	7		7	7	7
High quality, Mix A			A5	A7		A50	A75	A100
Loading rate [GPa/s]			17.7	12.0		15.0	13.4	-
Number of experiments			5	6		12	12	
Low quality, Mix B		B0	B5	B7		B50	B75	B100
Loading rate [GPa/s]		10.0	13.7	13.4		10.8	11.0	-
Number of experiments		3	4	8		8	11	8

From the evaluation as described in section 5.3, the following test procedure was derived.

- Because of the limited deformation capacity of the glued seam, the static compression level was applied in two steps. Before the specimen was glued between the SH bars, 75% of the final compressive load was applied. This level was chosen related to the deformation under sustained load.

- Examination and adjustment of symmetry were a part of the compressive loading procedure. Symmetry was examined by the lateral strain-gauges, while the total compressive level was derived from the deformation of the tension rods, see Chapter 5.

- Subsequently the specimen, clamped in the lateral compression device, was placed in the SHB apparatus and glued between the bars. The residual of the glue was thoroughly removed from the adapters and from the brushes, to ensure the deformation capacity.

- During the hardening time of the glue, about half an hour, the compressive load was kept constant by using an accumulator in the hydraulic system close to the jacks.

- After the glue had hardened the remaining 25% of the compressive load was applied.

- The accumulator was blocked and the dynamic tensile test was performed.

- After the impact test, the compressive load was manually released to prevent crushing the specimen.

The various stages of the test procedure are illustrated in Figure 7.1.

Commonly the scatter in biaxial test results is large. Referring to the evaluation of the test set-up and the fact that the applied test method is new, a significant scatter was expected. In order to select the most reliable tests three criteria were used.

- symmetry of the static lateral compression;

- uniaxial wave propagation during impact test;

- sequence of axial and lateral response during impact test.

Concerning the criterion of symmetry, it is mentioned that in about 80% of the tests the ratio of observed deformation at front and rear side or at top and bottom, was larger than 0.5, which was the arbitrary criterion applied. Note that symmetry appeared to increase with increasing compression level.

Both the other criteria need more extensive discussion which is given in the next section.
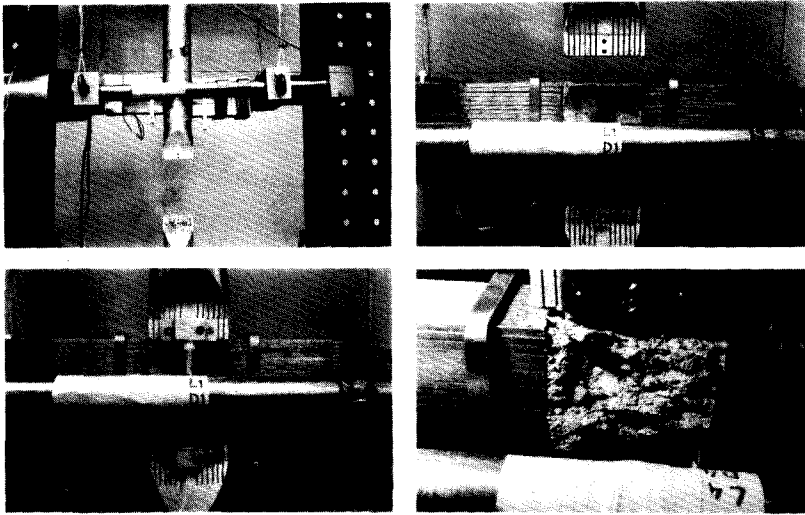
Figure 7.1   Four stages of the biaxial test; e.g. for high compression level.

7.2   Effects due to interaction of loading devices

To determine the failure envelope, the most critical aspect that emerged from the evaluation of the biaxial test set-up is the interaction process between the static and dynamic device. The influence of the lumped lateral device appeared to increase significantly with increasing axial deformation.

The principle of the Split Hopkinson Bar is based on uniaxial wave propagation. Therefore the second criterion to judge the performed biaxial tests is the validity of this principle. It is emphasized that only the response was considered up to maximum stress.

As in the uniaxial tests the shape and the strain rates of the recorded pulses in the lower bar, the specimen and the upper bar were examined. The shapes reflected the process of wave reflection and transmission. The sequence in time was the same as observed during the uniaxial tests.

The next step was the comparison of the various strain rates that were recorded, to gain information on wave transmission. Table 7.2. gives the data for the experiments which passed the "symmetry-criterion".

Table 7.2   Strain rates in the lower bar ($\dot{\varepsilon}_l$), the specimen ($\dot{\varepsilon}_s$) and the upper bar ($\dot{\varepsilon}_u$) experiments selected on symmetry.

	n*	$\dot{\varepsilon}_l$ [1/s]	$\dot{\varepsilon}_s$ [1/s]	$\dot{\varepsilon}_u$ [1/s]	$\dot{\varepsilon}_u/\dot{\varepsilon}_l$ [-]	$\dot{\varepsilon}_u/\dot{\varepsilon}_s$ [-]
A7	6	0.136 (11)*	0.211 (13)	0.118 (28)	0.87	0.56
A50	9	0.179 (19)	0.243 (22)	0.134 (19)	0.76	0.61
A75	11	0.178 (16)	0.208 (32)	0.114 (27)	0.64	0.57
B7	8	0.183 (19)	0.259 (15)	0.124 (20)	0.68	0.48
B50	9	0.198 (7)	0.208 (26)	0.102 (15)	0.52	0.49
B75	9	0.198 (11)	0.313 (79)	0.094 (29)	0.48	0.44

*   n is the number of tests and the coefficient of variation [%] is given in brackets.

From these data it emerges that

-   The loading rate of the generated loading pulse varied during the experimental programme but was about constant in both biaxial test series.

-   The scatter in response and transmitted pulse increased with increasing compression level.

-   Application of the lateral device led to a significant reduction of the stresses transmitted to the specimen.

-   Wave transmission from the specimen to the upper bar seems to be hardly affected by the lateral compression. Note that the strain rate in the specimen might increase due to a reduction in Young's modulus at higher compression levels. Therefore, a constant ratio $\dot{\varepsilon}_u/\dot{\varepsilon}_s$ implies that, related to the stress pulse in the specimen, the stress pulse transmitted to the upper bar possibly increased with increasing compression level.

The most dominant observation is the fact that a minor part of the incident loading pulse is transmitted to the specimen. An explanation could be a reduced acoustic impedance of the specimen at higher compression levels. But, during the ascending branch of the pulse, multiple reflections occur at the interfaces and the influence of the acoustic impedance on the average loading rate in the specimen can be neglected. Most consistent with the observations is the explanation that a part of the incident pulse was transmitted to the lateral loading device.
To examine the coupled response of specimen and brush bearing platens to resist the dynamic loading, the transmitted pulse in the upper bar was related to the deformation of the specimen. A linear elastic response of the specimen was assumed which resulted in an apparent stiffness, E*, for the first part of the loading and response curve. Figures 7.2 and 7.3 show the E* values for the selected tests for the A-series and B-series, respectively.
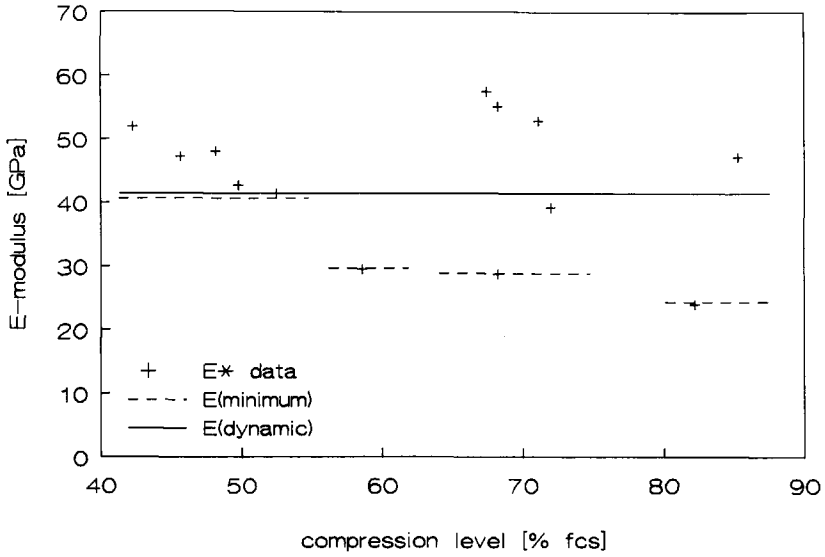
Figure 7.2   The observed E* values as a function of the compression level; A-series.
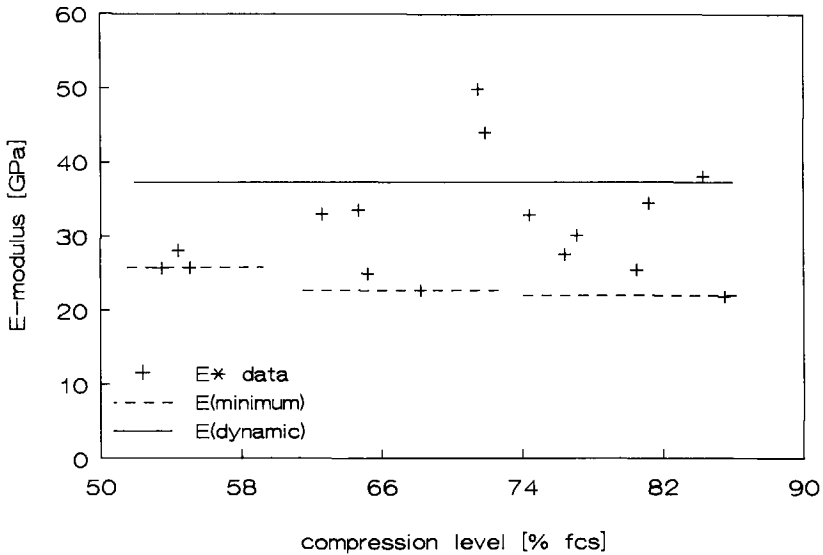
Figure 7.3   The observed E* values as a function of the compression level; B-series.

In these figures, the E values for dynamic, uniaxial loading are given as solid lines. The influence of the lateral device is clearly present. It appears that stiffnesses observed even exceed the upper limit of E_{dyn}. The feature of the high $E^\star$ values and the ratios of the strain rates led to the conclusion that a part of the loading was transmitted to the lateral device and recorded in the upper bar as an additional strength of the specimen. The contribution of the lateral device in axial response had to be quantified, while the true values of the dynamic Young's moduli at the various compression levels were unknown.

In order not to overestimate the influence of lateral compression on the residual impact tensile strength, the contribution of the lateral device was estimated in a lower limit approach. The procedure was as follows.

The experiments were clustered in groups with a small variance in compression level. For each group, the lowest $E^\star$ value observed was considered to be the "true" dynamic Young's modulus of the material. The upper limit is given by the dynamic Young's modulus for uniaxial loading. The decisive $E^\star$ values for each group are given as dashed lines in Figures 7.2 and 7.3. These reference values varied from the dynamic upper limit to about ninety per-cent of the static Young's modulus.

The contribution of the lateral device was estimated for each test by using the ratio of the apparent stiffness $E^\star$ and the lowest value of the group.

This approach leads to a lower limit estimate for the lateral device contribution because the linear parts of the ascending branches were used to calculate the $E^\star$ values, which implies a threshold at about 70% of the observed residual strength. Beyond the threshold, the response becomes non-linear, the deformation increases and the contribution of the lateral device increases.

In the next section, the results of the followed procedure on the strength data will be presented and discussed. To select the representative set of experiments, first another aspect of interaction had to be examined, i.e. the third criterion mentioned in the former section.

From the evaluation it emerged that a test should be refuted when the lateral deformation initiates a response in axial direction, see section 5.3.5. It was concluded that the lateral deformation due to the impact load could lead to a sudden change in load transfer and ruin the "uniaxial" wave propagation completely. Therefore, the recordings were examined to see whether the lateral response initiated an axial response in the ascending branch of the stress pulse. It appeared that this sequence did not occur in any of the experiments on concrete.

From this observation it was concluded that the experimental data could be used to determine the residual impact strength, including the contribution of the lateral device in the axial response.

The examination on uniaxial wave propagation and the interaction during the impact test resulted in a further reduction of the number of representative tests. The "transmission data" as presented in Table 7.2, are given in Table 7.3 for the

representative tests. Note that the data in Figures 7.2 and 7.3 correspond to the finally selected tests.

It is emphasized that the scatter in residual impact strength was not a part of the selection procedure. The selection was based on the test conditions, i.e. symmetry and influence of interaction.

Table 7.3   Strain rates in the lower bar ($\dot{\varepsilon}_l$), the specimen ($\dot{\varepsilon}_s$) and the upper bar ($\dot{\varepsilon}_u$); representative experiments.

	$n^\star$	$\dot{\varepsilon}_l$ [1/s]	$\dot{\varepsilon}_s$ [1/s]	$\dot{\varepsilon}_u$ [1/s]	$\dot{\varepsilon}_u/\dot{\varepsilon}_l$ [-]	$\dot{\varepsilon}_u/\dot{\varepsilon}_s$ [-]
A7	6	0.136 (11)*	0.211 (13)	0.118 (28)	0.87	0.56
A50	6	0.171 (19)	0.249 (19)	0.143 (17)	0.84	0.58
A75	7	0.181 (11)	0.237 (27)	0.126 (17)	0.70	0.53
B7	8	0.183 (19)	0.259 (15)	0.124 (20)	0.68	0.48
B50	7	0.196 (6)	0.220 (20)	0.102 (16)	0.52	0.47
B75	9	0.202 (11)	0.252 (52)	0.103 (21)	0.51	0.41

$\star$ n is the number of tests and the coefficient of variation [%] is given in brackets.

7.3   Data on residual impact strength

In this section, the strength data of the biaxial experiments will be presented and related to the question whether the rate effect is influenced by the level of lateral compression.

Unfortunately, the static reference tests had to be cancelled and, consequently a reference envelope from literature had to be chosen. It was decided to use the results Kupfer obtained for his intermediate and low quality concrete with compressive strengths of 31 and 19 [MPa], respectively.

The observed residual strength of the representative experiments on the high quality concrete is given in Figure 7.4 denoted with crosses. Because of the contribution of the lateral device to the observed strength, the data had to be adjusted. The method based on stiffness values, as given in section 7.3, was used to obtain an upper limit estimate for the residual strength. The set of adjusted data is depicted as triangles in Figure 7.4. The dashed and solid lines are third order polynomial fits for both set of data presented in this figure.

These data show that by taking the contribution of the lateral device into account leads to a significant reduction in strength. The considerable scatter, however, is not reduced in the adjusted data. For the biaxial tests, the scatter is not quantified because of the limited number of experiments and the variation in compression level.
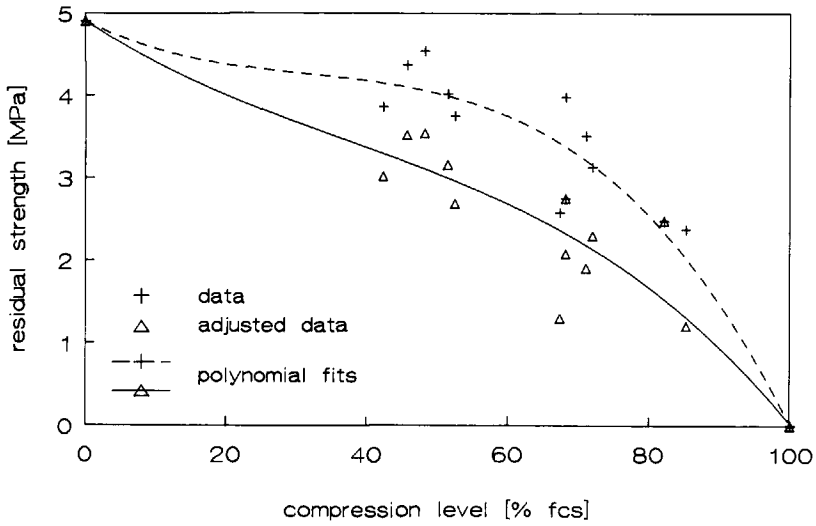
Figure 7.4   The residual strength data and polynomial fits for the measured and adjusted data; Mix A.
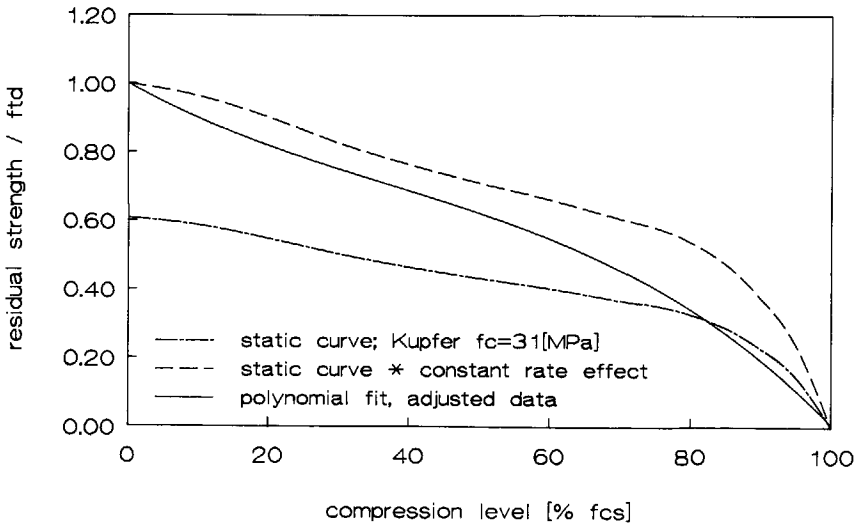
Figure 7.5   Failure envelopes for Mix A.
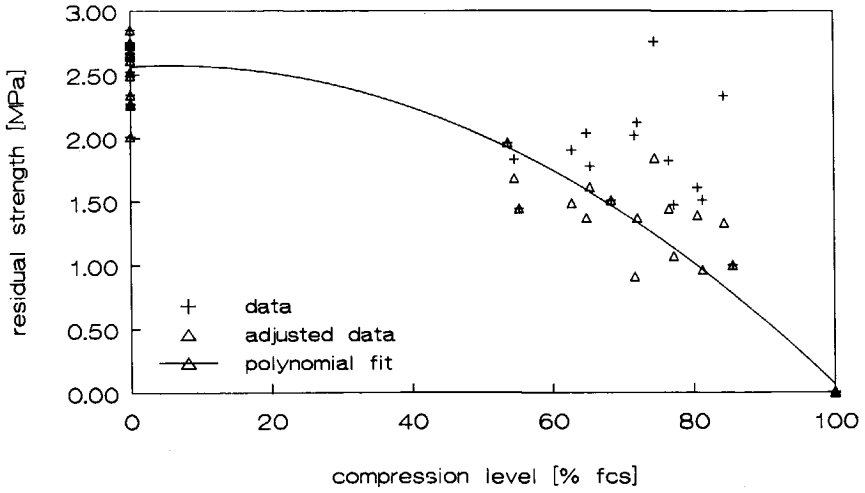
Figure 7.6   The residual strength data and polynomial fits for the measured and adjusted data; Mix B.
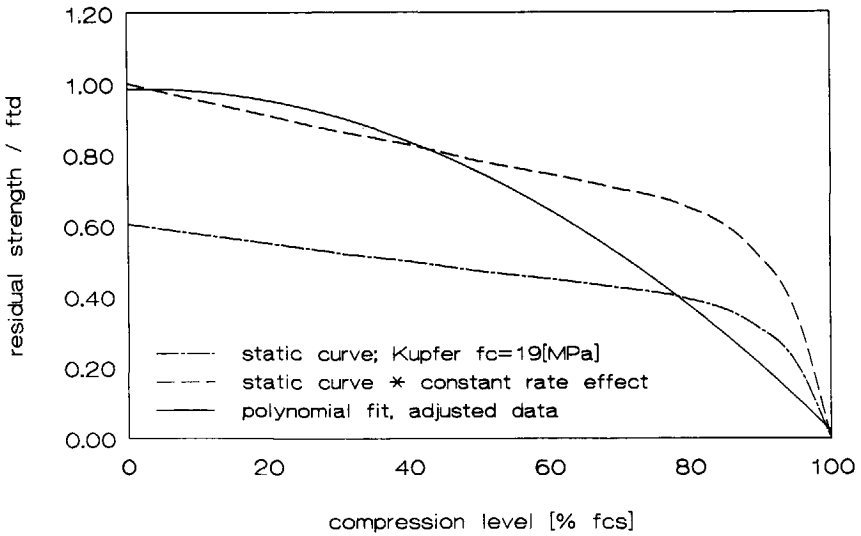
Figure 7.7   Failure envelopes for Mix B.

Because the effect of the lateral device could only be estimated, no definite conclusions can be drawn from these data. Nevertheless, tendencies in the effect of lateral compression on the rate effect can be observed and determined.

In Figure 7.5 three failure envelopes are given for the residual tensile strength. The residual strength is normalized with the dynamic uniaxial tensile strength, f_{td}, of Mix A of the current programme.

The lower dashed line in this figure is the failure envelope determined by Kupfer from his static tests on concrete with $f_c = 31$ [MPa]. This curve is the reference to judge the influence of the compression level on the rate effect in the residual tensile strength. When the rate effect is not affected by the level of lateral compression, the observed rate effect for uniaxial tensile loading can be used to determine the residual impact strength. Thus, the static envelope is extended uniformly which results in the upper dashed line in Figure 7.5. The experimental data, represented by the polynomial data fit is depicted as the solid line in this figure. This curve shows the tendency of the experimental data to approach the static envelope at high compression levels. The rate effect is reduced by the lateral compression.

Concerning the reliability of the compression level, it is mentioned that the deformations recorded during the lateral prestressing show a regular feature and do not indicate an overestimate of the compression level.

Figures 7.6 and 7.7 give the results for the low quality concrete with the static reference envelope of Kupfer for $f_c = 19$ [MPa].

From these figures it emerges that the tendency concerning the rate effect is similar to the results for the high quality concrete.

In addition to the comments given above for the high quality concrete, it is mentioned that the recorded deformation due to the lateral compression was relatively small in comparison with the observed deformation at static failure. Consequently, the compression level given in the figures might be too high.

Referring to the upper limit approach for the residual strength, it is concluded that the rate effect decreases with increasing compression level. The reduction could not be quantified because of the scatter and the uncertainties in the axial load transfer during the impact tests. At the applied loading rate of 15 [GPa/s], the dynamic failure envelopes for the high quality concrete and for the low quality concrete show the tendency to approach the static envelope at high compression levels.

A comparison with the model prediction and the questions raised on the effect of multiple cracking will be discussed in section 7.6.

7.4   Reconstructed load-deformation curves

With the applied measurement set-up it was possible to examine the failure process in each test. An average response or failure process, however, could not be deduced because the interaction process appeared to be unpredictable. From the load and response measurements, it emerged that the effect of the interaction increased with increasing compression level and axial deformation. Similar to the procedure followed

for the uniaxial loading, the load-deformation curves were derived. Because of the significant influence of the interaction process, these relations are not suitable to study the material response.

In this report, the aspects of deformation capacity and fracture energy will not be discussed for the biaxial loading condition. Just to illustrate the shortcomings of the test set-up, and show some of the observed features, the reconstructed load-deformation curves are given in Figure 7.8.

a) Mix A, high quality concrete
b) Mix B, low quality concrete
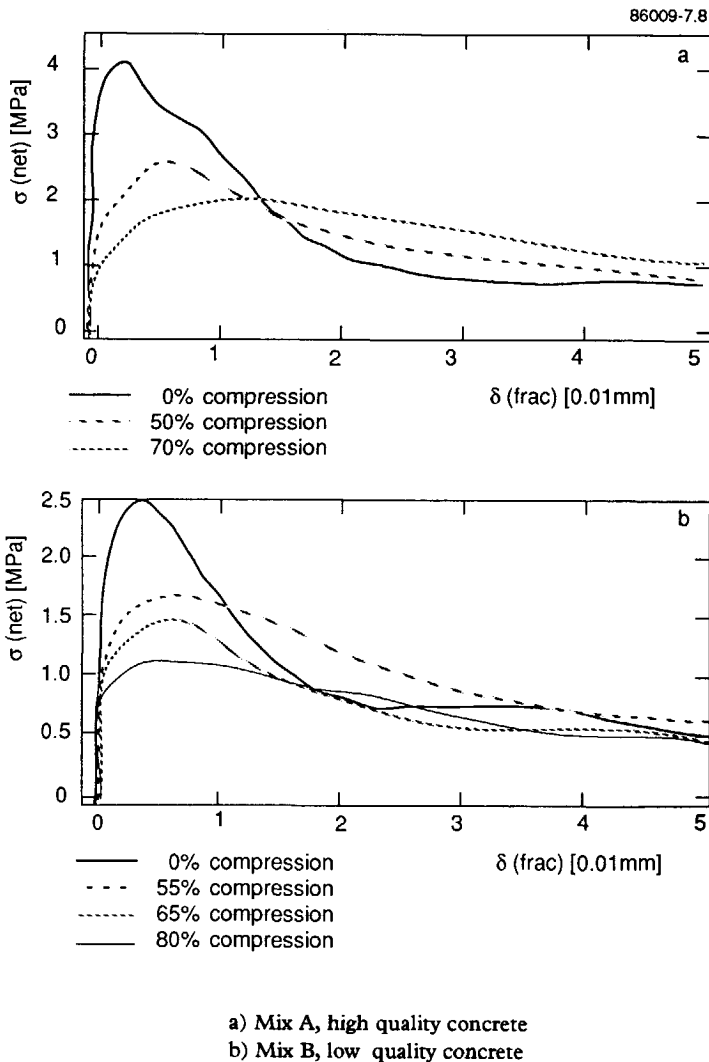
Figure 7.8   The load deformation curves for the high and low quality concrete.

The general feature of the ascending branches is an increasing deformation with decreasing residual strength, while the descending branches were definitely affected by the lateral device. The latter resulted in too high stress levels in the softening branch and a long-tailed curve.

The increase in deformation was also observed by Zielinski [125] and is a feature of the static response.

Note that for these curves the load levels are adjusted for the contribution of the lateral device, using the first part of the ascending branch. This contribution, which was the highest for Mix A, will be more pronounced in the response just before the maximum strength is reached. Therefore, the difference in non-linearity for the low and high quality concrete cannot be used for conclusions on material response.

Finally it is mentioned that the regular change in shape of the various curves do not indicate a change in failure mechanism.

7.5   Residual impact strength in experiment and model

The biaxial model as presented in Chapter 4, uses the uniaxial tensile condition as reference. The effects of lateral compression on the geometry of the fracture plane, the initial stress and damage conditions were translated to the fictitious fracture plane and load conditions. The possible effects of multiple cracking on the balance of energy supply and demand were not included in the model. Consequently, when multiple cracking is a dominant mechanism in the biaxial response, the model underestimates the residual impact strength. Figures 7.9 and 7.10 give the model predictions, the fit to the adjusted data and the references based on the Kupfer data as given in section 7.3.

Note that the model prediction comprises the static failure envelope as well as the rate effect on the residual strength.

The results for Mix A show a very good correspondence between experiment and prediction. From the fact that the adjusted data give an upper limit for the residual strength while, on the other hand the model does not deal with the mechanism of multiple cracking, it is concluded that for the high quality concrete the supplied energy is not diffused along multiple cracks.

It should be noted that the predicted rate effect for uniaxial loading was too high for the low quality concrete, see Chapter 6. To enable a judgement of the predicted effect of lateral compression, the prediction for the residual strength was normalized at the dynamic tensile strength.

The model prediction for Mix B shows a strong decrease of the residual impact strength just beyond the compression level of 0.3 f_c. The initiation of bond fracture due to the lateral compression clearly affects the predicted rate effect on the residual strength, see Chapter 4, Figure 4.14.

The curves in Figure 7.10 show that the model prediction is too low. The difference between model and experiment, however, is too small to prove the presence of a mechanism which is not covered by the model. Nevertheless it indicates a possible effect of multiple cracking. It is expected that this mechanism results in a larger width of the failure zone and larger deformations in the pre-peak fracture process. Referring

to the former section, the load-deformation curves do not indicate a more pronounced non-linearity of the ascending branch at high compression levels.

From these observations it is concluded that the mechanism of multiple cracking and energy dispersion might have been active for the low quality concrete, but it was of minor importance.

Figure 7.9   The failure envelopes given by the model, the experiments and the static Kupfer data; Mix A.

The curves in Figure 7.10 show that the model prediction is too low. The difference between model and experiment, however, is too small to prove the presence of a mechanism which is not covered by the model. Nevertheless it indicates a possible effect of multiple cracking. It is expected that this mechanism results in a larger width of the failure zone and larger deformations in the pre-peak fracture process. Referring to the former section, the load-deformation curves do not indicate a more pronounced non-linearity of the ascending branch at high compression levels.

From these observations it is concluded that the mechanism of multiple cracking and energy dispersion might have been active for the low quality concrete, but it was of minor importance.

In contrast with all the uncertainties of the true material response, the correspondence of the model prediction and the experimental data clearly show that the rate dependency of the residual impact strength is affected by the level of lateral compression. Although the reference base of experimental data is small, the conclusion that the dominant mechanisms are covered properly by the model seems to be justified.
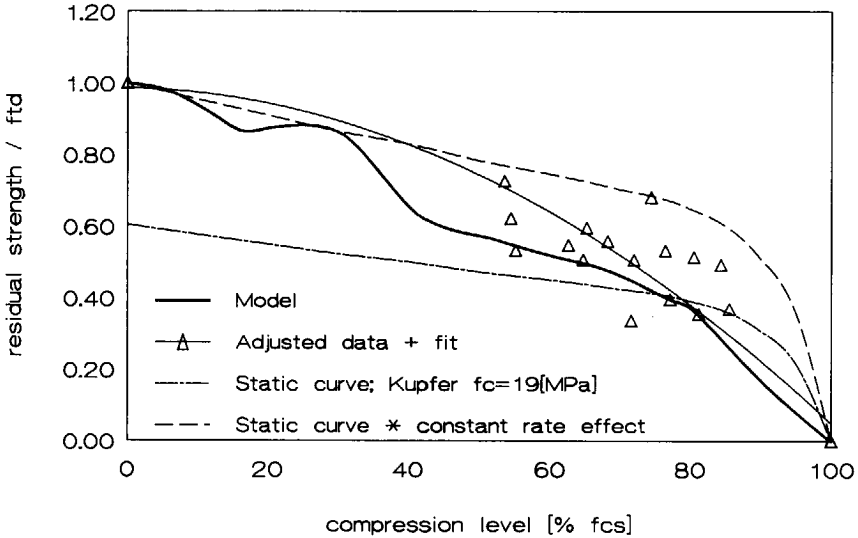
Figure 7.10 The failure envelopes given by the model, the experiments and the static Kupfer data; Mix B.

7.6   Applicability of the biaxial set-up

After the evaluation of the biaxial test set-up, Chapter 5, it was clear that the set-up had several shortcomings. The biaxial concrete tests confirmed the presence of imperfections, but from these tests it is also emerged that the applied testing technique introduces too much uncertainly about the load transfer during the dynamic part of the test on concrete onsequently the residual impact strength could only be determined by approximation.

For future research, it is recommended not to proceed with the applied biaxial test set-up. An alternative is given by the fluid pressure cell, such as was recently successfully applied by Malvern in his biaxial compression-compression tests with the SHB [60b]. In combination with the SHB, the axial-symmetric loading condition of radial static compression and, axial dynamic tension can be realised

7.7   Concluding remarks

The biaxial loading condition and the applied test set-up led to a complex process of loading and response. The interaction between the static and dynamic loading device results in response data in which material and structural response of specimen and loading device were integrated. This feature constrained the analysis of the data to the primary objective, the residual impact strength.

The contribution of the lateral loading device to the dynamic axial response could be estimated and an upper limit of the residual tensile strength was obtained. From the data it emerged that the rate dependency of the residual tensile strength reduced with increasing lateral compression. This feature was also predicted by the theoretical model. The prediction for the high quality concrete was in very good agreement with the experiments. For the low quality concrete, the residual strength was slightly underestimated.

The effect of multiple cracks on the energy demand for the dynamic failure process was not observed and is considered to be of minor importance for the residual impact strength.

8   SUMMARY AND CONCLUSIONS

The subject of the research programme was the material response of concrete under impact tensile loading. Special attention was paid to the influence of static lateral compression on the residual tensile strength and to the deformation capacity of a single failure zone under uniaxial tensile loading. The study can be considered as a continuation of the research programmes on the uniaxial response at the Delft University of Technology. In Delft the SHB technique is applied, which is considered to be the most suitable experimental technique to study the material behaviour under uniaxial conditions.

Former research has shown that the rate effect on the tensile strength appears to be considerable, especially at high loading rates, and contributes to the resistance of concrete structures to dynamic loading. The knowledge on the uniaxial response covers an important but limited part of the loading conditions in structures, while the knowledge on material behaviour under dynamic multiaxial loading is very scarce. To continue the material research, and extend the knowledge needed for numerical modelling, a theoretical and experimental study was started.

In the theoretical part, attention was focused on the failure process at meso level related to the response features at macro-level. The extension of the initially present damage was considered to be the key to understanding and modelling the dynamic properties.

First the loading of uniaxial tension was considered. The damage extension was modelled to a fictitious fracture plane as described in Chapter 3. Concrete composition and properties were used to translate the geometry of the real fracture plane to a fictitious fracture plane with equally distributed penny-shaped cracks. The fictitious plane represented the initial damage and the energy demand in the pre-peak fracture process under static loading. Linear Elastic Fracture Mechanics was used to describe crack extension as a function of the loading rate.

In the model, the predicted crack extension under static loading was used as the reference to quantify the rate effect on tensile strength. Both the moderate and steep strength increase are described by the model, and quantitatively the rate effect is predicted well for all loading rates.

From the model it emerged that the rate effect up to a loading rate of about 10 [GPa/s] depends on the changing energy demand to form the fracture plane. At higher loading rates, the mechanical response of the material around the crack tips govern the energy demand for fracture and not the changing geometry of the fracture plane or multiple cracking. It appears that inertia effects become dominant, resulting in a reduced rate of crack propagation and therefore a steep strength increase.

From the fact that the model describes the rate effect on tensile strength well for all loading rates and reflects also the rate sensitivity for different concrete qualities, it was concluded that the most important aspects of dynamic, pre-peak material response can be characterized by the extension of existing damage in the fictitious fracture plane.

Consequently, it offered the possibility to predict the effect of changing initial conditions due to static lateral compression.

The initial conditions due to lateral compression and the prediction of the rate sensitivity of the residual tensile strength were the subjects of Chapter 4. The modelling procedure proposed in this chapter had a speculative character because of the uncertainties about the initial conditions, and the criterion to judge the final result, i.e. the predicted rate sensitivity, which was unknown from literature.
The tensile and compressive failure mode have been considered in the model. In the case of tensile failure, the initial damage and stresses could be related to equivalent conditions for uniaxial tensile loading. The model description for this uniaxial loading functioned as a reference. For compressive failure, the scheme of one of the representative fictitious fracture planes for compression was used to represent the initial conditions and to describe the damage extension due to the subsequent tensile loading. In the model, attention was mainly focused on the tensile failure mode which is dominant for compression levels up to about 80% of the compressive strength.

A relation between the degree of bond failure under tension and compression was derived by considering the local stresses at the surface of spherical aggregates embedded in the mortar matrix. The stresses were combined with a local Mohr-Coulomb failure criterion which followed from bond fracture initiation under uniaxial compression and tension. With the assumption that each aggregate particle has a single defect with random orientation, the number of activated defects followed from the local stresses and failure criterion for each biaxial loading condition of tension and compression. Iso-damage curves for bond failure were the result, and the wanted relation between the initial conditions under compression and tension was obtained.
The final failure envelope for concrete under static loading followed from the iso-damage line of 100% bond failure and the additional strength given by the matrix under uniaxial tension. Beyond the compression level of 0.8 f_c, the residual strength follows from crack extension in the fictitious fracture plane for compression. Application of this approach to the concrete qualities tested in the experimental programme, results in failure envelopes which show good correspondence with the envelopes determined experimentally by Kupfer.
To examine the influence of lateral compression on the rate dependency of the residual tensile strength, the crack extension model was applied. The calculations showed that the rate effect decreases with increasing compression level for all loading rates. The reduction predicted is large especially at high loading rates .
In literature, no experimental support is given for the predicted feature. On the contrary, from the only two published programmes on this loading condition it was posed that the rate effect was not affected by the lateral compression. The predicted dependency, however, is not refuted by the published data because of the large scatter. The results of the model and the available data emphasize the necessity of the planned experimental programme.

The experimental programme consisted of uniaxial and biaxial experiments. For the latter, the Split-Hopkinson Bar has been combined with an hydraulic loading device to apply the lateral compression. The specimen geometry was prismatic and two notches were applied to predetermine the failure zone and enable the deformation of a single failure zone to be recorded.

In a preliminary test programme, the new test set-up was evaluated and improved. Chapter 5 gives a description of the set-up and the results of the evaluation. The most critical aspect appeared to be the interaction between the lateral and axial loading devices. The lateral device contributes in the axial load transfer during the impact test. The contribution increases with increasing lateral and axial deformation and could not be quantified explicitly for the concrete tests. Consequently, the applicability of the set-up was limited to the main objective, the residual strength. The load-deformation relation could not be determined for the biaxial loading condition.

In the experimental programme, two concrete qualities were tested. The uniaxial impact tests on the notched specimen reflected the advantages and the disadvantage of the simple Split-Hopkinson testing technique. The ideal conditions for material testing were not fulfilled, on one hand because of the non-linear response of concrete and on the other hand because of the uncommon geometry of the specimen. The structural response of the specimen, and the synchronization of the load and response measurements complicated the analysis. Nevertheless, reliable data on dynamic strength, deformation capacity and fracture energy could be derived from the test data. Of special interest is the information on the single failure zone. The deformation capacity appears not to increase with increasing loading rate and the fracture energy also showed the same tendency. The increase of deformation capacity and fracture energy observed in former programmes must be attributed to multiple cracking and multiple failure zones, and therefore, the width of the considered fracture zone. The occurrence of these phenomena is caused by inertia effects and is a feature of structural response. Therefore, the inertia effects inside the material have to be separated from the material properties when these effects are covered by the mechanical response in the (numerical) calculation.

The experiments were simulated numerically by Sluys. According to the experience for static conditions, the numerical simulation offers good perspectives for material modelling. The simulation showed the sensitivity to the applied softening model and the necessity to incorporate the pre-peak non-linearity for the prediction of the dynamic response of plane concrete.

It is recommended to apply notched specimens to determine the dynamic fracture energy. Reference data for static conditions are necessary to judge the observed tendency in rate effect on the deformation capacity and fracture energy.

The considered width of the failure zone in experiments has a considerable impact on the observed material response. Attention should be paid to this phenomenon, in relation to the applied material parameters and element size in numerical calculations.

The biaxial experiments resulted in failure envelopes for the residual tensile strength at the applied loading rate of about 15 [GPa/s]. The effect of the lateral device on the residual strength was significant and was estimated using the observed stiffnesses in the first part of the load and response signals. The adjusted data represent an upper limit for the residual strength.

As references for static conditions, the experiments of Kupfer and the model prediction were used. From the data it emerged that the rate dependency of the residual strength reduced with increasing level of lateral compression. The dynamic envelope tends to approach the static envelope at high compression levels, the same feature as predicted by the theoretical model.

The model prediction for the residual impact strength of the concrete qualities tested was good. Therefore, it is concluded that the effect of multiple cracks, the initial damage level, has no major effect on the energy demand during the dynamic failure process.

Summarizing the results of the research programme, the main conclusions are:

-   The moderate rate effect on the uniaxial tensile strength is governed by the change in energy demand to form the fracture plane. Beyond loading rates of about 10 [GPa/s] the inertia effects inside the material dominate the response, delay damage extension and lead to a steep strength increase.

-   At uniaxial tensile loading, the deformation capacity and the fracture energy for a single failure zone do not increase with increasing loading rate.

-   The proposed model is capable of predicting the rate effect on strength for uniaxial tension and the influence of lateral compression. The model predictions are in accordance with the experimental data.

-   The rate effect on the residual impact strength decreases with the increasing level of lateral compression.

Samenvatting en achtergrond van onderzoek

Beton is een materiaal dat zich bij uitstek leent om toegepast te worden in constructies of delen van constructies die weerstand moeten bieden aan explosie- of stoot-belastingen. In het algemeen geldt dat om tot een veilig en economisch ontwerp te komen, de krachten in de constructie en de weerstand van het materiaal bekend dienen te zijn. De conditie van een explosie- of stootbelasting blijkt te leiden tot een respons van zowel de constructie als het materiaal, die in sterke mate verschilt van statische condities. Het verschil wordt veroorzaakt door het feit dat de belasting, en daarmee de energie, niet geleidelijk maar in zeer korte tijd en soms zeer lokaal wordt opgelegd. Hierdoor ontstaan er spanningsgolven met een hoge amplitude die het materiaal zwaar maar ook zeer snel belasten. Nu blijkt het materiaalgedrag van beton afhankelijk te zijn van de belastingsnelheid. Het meest duidelijk is dit voor de treksterkte die sterk toeneemt bij hogere belastingsnelheden. Deze sterkte toename bij snelle belastingen blijkt voor een belangrijk deel de weerstand onder dynamische belasting te bepalen. Voor het ontwerpen en dimensioneren van beschermingsconstructies betekent dit dat er materiaalmodellen nodig zijn die de invloed van de belastingsnelheid goed beschrijven en toegepast kunnen worden in moderne computercodes. In combinatie met de berekende krachtsverdeling kan dan de weerstand en de schade ten gevolge van een stoot- of explosiebelasting goed worden bepaald.

De kennis van het dynamisch materiaalgedrag van beton is echter nog beperkt. Onderzoek op dit gebied heeft zich tot nu toe met name gericht op de sterkte onder één-assige belasting. De invloed van de belastingsnelheid op andere belangrijke parameters als de vervormingscapaciteit en de breukenergie is echter nog nauwelijks onderzocht, terwijl het dynamisch materiaalgedrag onder meer-assige belasting nog als onbekend moet worden beschouwd.

De theoretische en experimentele studie die in dit proefschrift is beschreven betreft het materiaalgedrag van beton en richt zich op genoemde onderwerpen. Als voortzetting en uitbreiding van de eerder uitgevoerde onderzoeken aan de TU-Delft, is speciale aandacht geschonken aan de invloed van laterale, statische voorspanning op de resterende dynamische treksterkte in axiale richting. Daarnaast is de breukenergie en de vervormingscapaciteit van één enkele bezwijkzone onder één-assige dynamische trek-belasting onderzocht.

In het theoretische deel van de studie is de aandacht gericht op het bezwijkproces in het beton. Het beschouwde schaalniveau is dat van grindkorrels in een matrix van cement en zand. De schadeontwikkeling op dit niveau is namelijk direct gerelateerd aan de respons zoals dat op macro niveau wordt waargenomen. Voor de modellering van het dynamisch gedrag hebben als uitgangspunten gediend de initieel aanwezige schade en de wijze waarop deze schade zich onder dynamische belasting uitbreidt.

Allereerst is de één-assige trekbelasting beschouwd. In hoofdstuk 3 is het model be-schreven voor het bepalen van de dynamische treksterkte. Het model beschrijft de schade uitbreiding in het beton als de uitbreiding van schijfvormige scheurtjes in een fictief breukvlak.

Met behulp van de betonsamenstelling en de statische betongegevens is de geometrie van het fictieve breukvlak bepaald, en wel zodanig dat in het fictieve breukvlak de initieel aanwezige schade en de energiedissipatie in het bezwijkproces tot het punt waarop de maximale sterkte is bereikt, wordt vertegenwoordigd. Met behulp van de Lineair Elastische Breukmechanica is de scheuruitbreiding in het fictieve breukvlak beschreven als functie van de belastingsnelheid.

Met de gemodelleerde scheuruitbreiding onder statische belasting als referentie blijkt de invloed van de belastingsnelheid op de sterkte goed beschreven te kunnen worden. Het model geeft een goede predictie van zowel de geleidelijke sterkte toename voor belastingsnelheden tot aan 10 [GPa/s] als de zeer sterke toename voor hogere snelheden. Uit de modellering volgt dat het bezwijkproces bij hoge snelheden niet beheerst wordt door veranderingen in breukvlak geometrie of de vorming van meervoudige breukvlakken, maar de mechanische respons van het materiaal rondom de scheurtips. Traagheidseffecten gaan domineren en vertragen de scheuruitbreiding wat resulteert in een aanzienlijke sterkte toename.

Uit het feit dat de invloed van de belastingsnelheid op de sterkte goed beschreven kan worden aan de hand van de uitbreiding van de initieel aanwezige schade, is geconcludeerd dat de gevolgde werkwijze ook mogelijkheden moet bieden om de dynamische reststerkte te voorspellen als het beton al belast is door een statische voorspanning in laterale richting. Afhankelijk van de mate van het voorspanniveau zal het beton extra beschadigd zijn en de spanningen in het materiaal zijn toegenomen. Voor de modellering was het nodig, en voldoende, om de beginvoorwaarden voor het beschrijven van de dynamische scheuruitbreiding aan te passen. In hoofdstuk 4 staat beschreven op welke wijze de nieuwe beginvoorwaarden zijn bepaald en op welke wijze de voorspanning de invloed van de belastingsnelheid op de sterkte beïnvloed. Dit deel heeft een tamelijk speculatief karakter omdat het resultaat nagenoeg niet getoetst kon worden aan gegevens uit de literatuur. Het resultaat lijkt echter heel aannemelijk. De schade en de inwendige spanningen tengevolge van de statische voorbelasting blijken te leiden tot een afname van de dynamische sterkte. De invloed van de belastingsnelheid op de sterkte neemt duidelijk af, zelfs dusdanig dat bij hoge voorspangraden van 80 à 90% van de druksterkte, dit effect nagenoeg is verdwenen. De aanwezige schade maakt dat de geometrie van het uiteindelijke breukvlak al dusdanig is bepaald dat het mechanisme, verantwoordelijk voor de sterkte toename onder één-assige dynamische belasting, zich niet meer volledig kan ontwikkelen.

Tweemaal eerder was de twee-assige belastingstoestand experimenteel onderzocht. Beide onderzoeken leidden tot de conclusie dat de invloed van de belastingsnelheid op de resterende dynamische treksterkte niet wordt beïnvloed door statische dwarsvoorspanning. De tegenspraak tussen de modellering en de experimentele gegevens uit de literatuur onderstrepen het belang van het experimentele gedeelte van de huidige studie. Dit deel staat beschreven in de hoofdstukken 5, 6 en 7.

De experimenten zijn uitgevoerd met de Split Hopkinson Bar (SHB) op de TU-Delft. De SHB is met name geschikt om de éénassige dynamische sterkte van materialen te bepalen. De opstelling bestaat uit twee lange staven waartussen een proefstuk van het te

onderzoeken materiaal wordt geplaatst. De SHB op de TU-Delft is vertikaal opgesteld en de dynamische belasting wordt met behulp van een valgewicht, dat langs de onderste staaf glijdt en een aanbeeld treft, gegenereerd. Op deze wijze wordt een éénassige trekspanningsgolf opgewekt die zich naar boven voortplant en het te beproeven materiaal belast. Bij de experimenten zijn zowel de vervormingen van het proefstuk als de spanningsgolf in de bovenste staaf gemeten. De doorgegeven spanningspuls geeft de informatie over de grootte van de belasting op het proefstuk terwijl de vervormingen informatie geven hoe het materiaal op de belasting heeft gereageerd. In het huidige onderzoek wilden we naast de éénassige dynamische sterkte ook informatie krijgen over de dynamische vervormingscapaciteit, de hoeveelheid energie die opgenomen kan worden en bovendien nog de invloed van een statische dwarsvoorspanning op de rest-sterkte onderzoeken. Om dit te realiseren is de opstelling gecombineerd met een hydraulische voorspaneenheid en is de geometrie van het proefstuk aangepast. De proefstukken hadden een rechthoekige vorm en waren voorzien van zaagsneden om de plaats van bezwijken vast te leggen. Het een en ander had tot gevolg dat aan het eenvoudige concept van de SHB, dat gebaseerd is op één-assige golfvoortplanting, afbreuk werd gedaan. Om te onderzoeken of de opstelling geschikt was voor het geplande onderzoek, is allereerst een evaluatie uitgevoerd. Hieruit volgde dat de experimenten met grote zorg uitgevoerd dienden te worden en dat met name gelet moest worden op de wisselwerking tussen de statische en dynamische opstelling. Wij hadden te maken met een zeer complexe beproevingsconstructie waarin de statische voorspan-eenheid het proces van de dynamische respons meer ging beïnvloeden naarmate de vervorming tijdens het dynamische experiment toenam. Voor het gestelde doel om de invloed van een statische voorspanning op de dynamische reststerkte te bepalen was de opstelling echter in principe geschikt.

Wat betreft het aspect van de dynamische vervormingscapaciteit en de breukenergie onder één-assige dynamische trekbelasting voldeed de gebruikte beproevings- en meetopstelling goed. Dankzij de uitgebreide meetopstelling kon het bezwijkproces van de proefstukken gereconstrueerd worden. Door het toepassen van een doorsnede reduktie werd de grootte van de bezwijkzone goed gedefinieerd en kon met behulp van de uitgevoerde metingen de dynamische breukenergie eenduidig worden bepaald. Dit was met de tot nu toe gebruikte opstellingen en beproevingsmethoden niet mogelijk.

Het uitgevoerde éénassige onderzoek was beperkt van omvang, toch kan de belangrijke conclusie getrokken worden dat de dynamische breukenergie niet toeneemt bij toenemende belastingsnelheid. De resultaten lieten een tendens zien dat de breukenergie en de vervormingscapaciteit juist afnemen. Deze conclusie is belangrijk omdat de tot nu toe gehanteerde beproevingswijzen, waarbij de grootte van de bezwijkzone of de belastingafdracht niet eenduidig bepaald is, juist een toename van de breukenergie lieten zien. De nieuwe informatie over de vervormingscapaciteit en de breukenergie is verwerkt in een "softening" model dat het gedrag van beton weergeeft in de fase van het moment dat het zijn maximale sterkte heeft bereikt tot aan volledig bezwijken. Dit model is samen met een aantal andere modellen in de eindige elementen code DIANA geïmplementeerd. De numerieke simulatie van de experimenten met behulp van het voorgestelde softening model was succesvol. Vergelijking met andere modellen liet zien hoe gevoelig het berekeningsresultaat is voor het toegepaste materiaalmodel.

Tot slot de resultaten van de twee-asssige proeven. De evaluatie had al laten zien dat de interactie tussen de statische en dynamische opstelling de beperkende factor zou zijn bij het herleiden van de materiaalrespons uit de testdata. De analyse van de beproevingsresultaten bevestigde dit met als direkt gevolg dat wij ons moesten beperken tot het afleiden van de sterkte. Informatie over de vervorming en de breukenergie bleek te zeer verstrengeld te zijn met de respons van de beproevingsopstelling in z'n geheel. De dynamische reststerkte als functie van de voorspangraad was het vooraf gestelde doel en die kon worden bepaald.

De experimentele resultaten lagen volledig in dezelfde lijn als de theoretische voor-spelling van de modellering. Duidelijk nam de invloed van de belastingsnelheid op de reststerkte af naarmate de statische voorspanning toenam. Het ontwikkelde model bleek ook kwantitatief een goede voorspelling te geven voor de dynamische reststerkte. De gevolgde werkwijze om de dynamische sterkte van beton te beschrijven aan de hand van de schade-ontwikkeling in een representatief breukvlak, blijkt dus voor meerdere belastingscondities toepasbaar.

Wanneer we de hele problematiek van betrouwbare materiaal modellen voor de dynamische respons van beton beschouwen en daarin het bereikte resultaat plaatsen, dan is een kleine stap voorwaarts gezet in een nieuw onderzoeksgebied.

Als direkt resultaat van het experimentele deel ligt er nu een methode om de breuk-energie als functie van de belastingsnelheid eenduidig te bepalen. Ook is aangetoond dat de invloed van de belastingsnelheid op de reststerkte afneemt naarmate het beton vooraf meer door een statische belasting is beschadigd. Daarnaast is de invloed van de dynamica op het bezwijkproces van beton langs theoretische weg bestudeerd en ge-modelleerd. De schade-ontwikkeling in combinatie met de dynamica blijkt de sleutel te zijn om de dynamische repons van beton te begrijpen en te modelleren.

Notation

Mathematical symbols are defined the first time that they are used. Brief definitions of the most frequently used symbols are listed below. Some symbols have different definitions in different sections. In such cases, definitions are stated locally and are used consistently within sections.

A	surface
a	crack radius
$\dot{a}$	crack tip velocity
b	centre to centre crack distance
d	aggregate diameter
D	mean diameter of considered aggregates
D_{max}	maximum aggregate diameter
C_p	longitudinal wave velocity
C_r	Rayleigh wave velocity
C_s	shear wave velocity
E	Young's modulus
$E^\star$	apparent Young's modulus
E_d	fracture energy
E_o	energy level at time t_o
E_k	kinetic energy
E_v	deformation energy
f_c	uniaxial compressive strength
f_t	uniaxial tensile strength
$f(a/b)$	geometry function
G_f	fracture energy
G_I	energy release rate
$g(a/b)$	geometry function
$h(a/b)$	geometry function
k	coefficient
K	characteristic length
$k(\dot{a})$	function to adjust stress field to inertia effects
K_I	stress intensity factor
$\underline{l}(\theta)$	field vector
p	load
p_a	aggregate volume ratio
p_c	chance of decisive initial defect at aggregate
$\dot{p}$	loading rate
PSI	ratio dynamic and static tensile strength
r	distance to crack tip
S	$\lambda \cdot K$
t	time
t_o	time zero of crack growth initiation
$\underline{u}$	displacement field

$\dot{\underline{u}}$	velocity field
V	volume (of torus)
W	external work

α	angle, orientation of defect at aggregate
β	coefficient
γ	specific surface energy
δ	deformation
δ_b	coefficient of equivalent load in compressive scheme for bond failure
δ_m	coefficient of equivalent load in compressive scheme for matrix failure
ε	strain
$\underline{\varepsilon}$	strain field
$\dot{\varepsilon}$	strain rate
φ_c	critical angle of aggregate intersection
λ	coefficient of characteristic length
θ	angle related to crack tip
υ	Poisson's ratio
ρ	density
σ	stress
$\underline{\sigma}$	stress field
τ	time parameter
ω	damage parameter
ξ_c	$\sin\varphi_c$
ψ	ratio of dynamic and static strength

Subscripts

a	aggregate
b	bond, begin
c	compression, critical
cyl	cylinder
d	dynamic
el	elastic
emp	empirical
eq	equivalent
i	inclusion
fr	fracture
frac	parameter related to failure zone
l	lower bar
m	mortar
m+a	mortar and aggregate
max	maximum
mod	model

r	radial
s	static, specimen
t	tension
tan	tangential
top	at maximum load level
tot	total
u	displacement , upper bar
o	at time t_o, static condition
t	at time t

Superscript

'	refers to compressive loading
.	derivative to time

Abbreviations

$CTOD_c$	critical Crack Tip Opening Displacement
FCM	Fictitious Crack Model
LEFM	Linear Ekastic Fracture Mechanics
MC	Mohr Coulomb
SHB	Split Hopkinson Bar

REFERENCES

1   Achenbach, J.D. and Brock, L.M.
"On quasistatic and dynamic fracture"
In: Dynamic Crack Propagation. ed. G.H.Sih
Noordhoff Int. Publ. Leyden, 1972

2   Alexander, M.G.
"Fracture energies of interfaces between cement paste and rock, and application to the engineering behaviour of concrete"
In: Fracture processes in concrete, rock and ceramics.
eds. J.G.M. van Mier et al.
RILEM Proceedings, Noordwijk, 1991.

3   Amman, W.
"Stahlbeton- und Spannbetontragwerke unter stossartiger Belastung"
Doctoral thesis, Zürich University of Technology, 1983.

4   Atkinson, C. and Shelby, J.D.
"The flow of energy into the tip of a moving crack"
Int. J. of Fract. Mech., Vol 26, No.4, 1984.

5   Baker, R.B.
"Dynamic stress created by a moving crack"
J. of Appl. Mech. Sept.1962, pp.449-458.

6   Berry, J.P.
"Some kinetic considerations of the Griffith criterion for fracture I.
Equations of motions at constant force"
J. Mech. Phys. Solids, Vol.8, 1960, pp.194-206.

7   Beskos, D.E.
"Fracture of plain concrete under biaxial stresses"
Cement and Concrete Research. Vol.4, 1974, pp.979-985.

8   Bischoff, P.H. and Perry, S.H.
"Compressive strain rate effects of concrete"
Proc. Materials Research Society Fall 1985, Boston, December 1985.

9   Borst, R. de
"Continuum models for discontinuous materials"
In: Fracture processes in concrete, rock and ceramics.
eds. J.G.M. van Mier et al.
RILEM Proceedings, Noordwijk, 1991.

10   Broberg, K.B.
        "The propagation of a brittle crack"
        Arkiv for Fysik, 18, 1960, pp.159-192

11   Broek, D.
        "Elementary engineering fracture mechanics"
        Noordhoff Int. Publ. Leyden, 1977.

12   Buyukozturk, O., Nilson, A.H. and Slate, F.O.
        "Stress-strain response and fracture of a concrete model in biaxial loading"
        ACI Journal, Proceedings.V. 68, No.8, 1971, pp 590-599.

13   Carpinteri, A., Ingraffea, A.R. (editors),
        "Fracture mechanics in concrete: Material characterization and testing."
        Martinus Nijhoff Publishers, 1984.

14   Chen, E.P.
        "Continuum damage mechanics studies on the dynamic fracture of
        concrete"
        Proc. Cement based composites: Strain rate effects on fracture. Boston,
        Massachusetts, USA, 1985.
        Mat. Res. Soc. Symp. Proc. Vol.64, 1986, pp.63-77.

15   Chen, A.C.T. and Chen, W.F.
        "Constitutive relations for concrete"
        J. of Engineering Mechanics Division, Vol.101, No.EM4, August 1975, pp.
        465-481.

16   "Concrete structures under impact and impulsive loading"
        Synthesis Report, CEB-FIP Bulletin d'information No.187, 1988.

17   Curbach, M.
        "Festigkeitssteigerung von Beton bei hohen Belastungsgeschwindigkeiten"
        Doctoral thesis, Karlsruhe University, 1987.

18   Curbach, M. and Eibl, J.
        "Crack velocity in concrete"
        Int. Journal Engineering Fracture Mechanics, Vol.35, No.1/2/3, 1990,
        pp.321-326.

19   Dargel, H.J.,
        "Zur rechnerischen Analyse von Stahl-betontragwerken unter stossartiger
        Beanspruchung". Doctoral thesis, Darmstadt University, 1984.

20   DiTomasso, A.
        "Evaluation of concrete fracture" in Fracture Mechanics of Concrete"
        Editors: Carpinteri, A and Ingraffea, A.R.
        Engineering Application of Fracture Mechanics publication. Martinus
        Niihoff Publishers, 1984.

21   Doudill, J.W.
        "Some results for the average stresses induced in the principal components
        of concrete"
        University of London, Kings College, London, 1970.

22   Dugdale, D.S.
        "Yielding of steel sheets containing slits"
        J. of Mechanics and Physics of Solids, Vol.8, 1960, pp.100-108.

23   Ewalds, H.L. and Wanhill, R.J.H.
        "Fracture Mechanics"
        Co-publication of Edward Arnold and Delftse Uitgevers Maatschappij,
        1985.

24   Freund, L.B.
        "Crack propagation in an elastic solid subjected to general loading I.
        Constant rate of extension"
        J. of Mechanics and Physics of Solids, Vol.20, 1972, pp.129-140.

25   Freund, L.B.
        "Crack propagation in an elastic solid subjected to general loading II. Non-
        uniform rate of extension"
        J. of Mechanics and Physics of Solids, Vol.20, 1972, pp.141-152.

26   Freund, L.B.
        "Crack propagation in an elastic solid subjected to general loading III.
        Stress wave loading"
        J. of Mechanics and Physics of Solids, Vol.21, 1973, pp.47-61.

27   Freund, L.B.
        "Crack propagation in an elastic solid subjected to general loading IV.
        Obliquely incident stress pulse"
        J. of Mechanics and Physics of Solids, Vol.22, 1974, pp.137-146.

28   Friedman, M., Handin, J. and Alani, G.
        "Fracture surface energies of rocks."
        Int. J. of Rock Mechanics, Vol.9, 1972, pp.757-766.

29   Gerstle, K.H., et al.,
"Behaviour of concrete under multiaxial stress states"
Proceedings, ASCE, Vol.106, EM6, December 1980, pp 1383-1403.

30   Glücklich, J.
"Fracture of plane concrete"
Proceedings of ASCE, Vol.89, No.EM 6, December 1963, pp.127-138.

31   Grady, D.E. and Kipp, M.E.
"Dynamic rock fragmentation"
In: Fracture mechanics of rock, ed. B.K. Atkinson, Academic Press, 1987.

32   Gran, J.K.
"Development of an experimental technique and related analyses to study the dynamic tensile failure of concrete"
Doctoral thesis, Stanford University, May 1985.

33   Hillerborg, A.
"Analysis of one single crack"
In: Fracture toughness and fracture energy of concrete, ed. F.H.Wittmann.
Elsevier Science Publishers B.V. Amsterdam, 1986.

34   Hordijk, D.A.
"Local approach to fatigue of concrete"
Doctoral thesis, Delft University, 1991.

35   Hordijk, D.A.
"Deformation-controlled uniaxial tensile tests on concrete"
Report 25.5-89-15/VFA, TU-Delft, 1989

36   Hughes, B.P. and Ash, J.E.
"Anisotropy and failure criteria for concrete"
Materiaux et constructions, Vol.3, No.18, 1970, pp.371-374.

37   Irwin, G.R.
"Fracture, Handbuch der Physik", Vol.VI, pp.551-590.
Springer, 1958.

38   Isida, M.
"On the tension of a strip with a central elliptic hole"
Trans. Jap. Soc. Mech. Eng., 21, 1955.

39   Jenq, Y.S. and Shah, S.P.
"A fracture toughness criterion for concrete"
Int. J. Engineering Fracture Mechanics, Vol.21, No.5, 1985, pp.1055-1069.

40   Jenq, Y.S. and Shah, S.P.
        "Fracture Mechanics and Constitutive Modeling of Concrete"
        In: Constitutive Laws for Engineering Materials: Theory and Applications,
        eds. C.S.Desai, et al.
        Elsevier Science Publishers B.V. Amsterdam, 1987.

41   Jensen, J.J.
        "Ductility of high strength concrete under special loading conditions".
        SINTEF Report, No. STF65 A91011, Norway, December 1990.

42   John, R., Shah, S.P. and Jenq, Y.S.
        "A Fracture mechanics model to predict the rate sensitivity of Mode I
        fracture of concrete"
        Northwestern University, Evanston, November 1986.

43   John, R. and Shah, S.P.
        "Effect of high strength and rate of loading on fracture parameters of
        concrete"
        Proc. Fracture of concrete and rock, Houston, June 1987.

44   John, R. and Shah, S.P.
        "Constitutive modeling of concrete under impact loading"
        Proc., sMiRT-9-Post Conference Seminar on Impact, Lausanne, August
        1987.

45   Kanninnen, M.F. and Popelar, C.H.
        "Advanced Fracture Mechanics"
        Oxford University Press, 1985.

46   Kipp, M.E., Grady, D.E. and Chen, E.P.
        "Strain rate dependent fracture initiation"
        Int. Journal of Fracture, Vol.16, 1980, pp.471-478.

47   Kipp, M.E., and Grady, D.A.
        "Dynamic fracture growth and interaction in one dimension"
        J. of Mechanics and Physics of Solids, Vol.33 No.4, pp.399-415, 1985.

48   Körmeling, H.A.
        "Strain rate and temperature behaviour of steel fiber concrete in tension"
        Doctoral thesis, Delft University of Technology, 1986.

49   Körmeling, H.A.
        "Impact tensile strength of steel fibre concrete"
        Stevin Report 5-84-8, Delft, 1984.

50   Körmeling, H.A. and Reinhardt, H.W.
"Strain rate effects on steel fibre concrete in uniaxial tension"
Int. Journal of Cement Composites and Leightweight Concrete. Vol.9,
No.4, November 1987, pp.197-204.

51   Körmeling, H.A., Zielinski, A.J. and Reinhardt, H.W.
"Experiments on concrete under single and repeated uniaxial impact tensile
loading"
Stevin Report 5-80-3, Delft University of Technology, 1980.

52   Kotsovos, M.D. and Newman, J.B.
"Behavior of concrete under multiaxial stress"
ACI-Journal, September 1977, pp.443-446.

53   Krajcinovic, D. and Fonseka, G.U.
"The continuous damage theory of brittle materials"
Part 1: General theory
Part 2: Uniaxial and plane response modes
J. of Applied Mechanics, Vol.48, December 1981, pp. 809-815 and 816-
824.

54   Krausz, A.S. and Krausz, K.
Fracture kinetics of crack growth"
Kluwer Academic Publishers, Dordrecht, 1988.

55   Kupfer, H.
"Das Verhalten des Betons unter mehrachsiger Kurzzeitbelastung unter
besonderer Berücksichtigung der zweiachsigen Beanspruchung".
Deutscher Ausschuss für Stahlbeton, Heft 229, 1973.

56   Kupfer, H. and Hilsdorf, H.K.
"Behavior of concrete under biaxial loading"
ACI Journal, August 1969, pp.656-666.

57   Lankford, J.
"Mechanisms responsible for strain-rate-dependent compressive strength in
ceramic materials"
Communications of the American Ceramic Society, February 1981,
pp.C33-C34.

58   Løland, K.E.
"Continuous damage model for load-response estimation of concrete"
Cement and Concrete Research, Vol.10, 1980, pp.395-402.

150

59   Maekawa, K. and Okamura, H. .
"The deformational behaviour and Constitutive equation of concrete using the elasto-plastic and fracture model"
Journal of the Faculty of Engineering, The University of Tokyo (B), Vol.XXXVII, No.2, 1983.

60   Mall, S., Kobayashi, A. and Loss, F.J.
"Dynamic fracture analysis of notched bend specimen"
Special Techn. Publ. No.711, American Society for Testing Material, 1980.

60[b]   Malvern L.E. and Jenkins D.A.
"Dynamic testing of laterally confined concrete"
ESL-TR-89-47, Engineering Research Division,
Air Force Engineering & Services Center, Tyndall AFB FL 32403

61   Mazars, J.
"Mechanical damage and fracture of concrete structures"
Proc. 5th International symposium on fracture, Cannes, 1980.

62   Meier, R.W., Ko, H.Y. and Sture, S.
"A direct tensile loading apparatus combined with cubical test cell for testing rocks and concrete"
Geotechnical Testing Journal. GTJODJ. Vol.8, No.2, June 1985, pp.71-78.

63   Mier van, J.G.M.
"Strain softening of concrete under multiaxial loading conditions"
Doctoral thesis, Eindhoven University of Technology, 1984.

64   Mihashi, H. and Wittmann, F.H.
"Stochastic approach to study the influence of rate of loading on strength of concrete"
Heron Vol.25, No.3, 1980.

65   Mindess, S.
"The application of fracture mechanics to cement and concrete: A hisyorical review"
In: Fracture Mechanics of Concrete, ed. F.H.Wittmann,
Elsevier Science Publishers B.V. Amsterdam, 1983.

66   Mlakar, P.F., Vitaya-Udom, K.P.and Cole R.A.
"Dynamic tensile and compressive behavior of concrete".
ACI Journal, July-August 1986, pp 484-491.

67   Modéer, M.
      "A fracture mechanics approach to failure analyses of concrete materials"
      Report TVBM-1001, Lund Institute of Technology, Sweden, 1979.

68   Mott, N.F.
      "Fracture of metals: some theoretical considerations"
      Engineering, 165, 1948, pp.16-18.

69   Muskhelishvili, N.I.
      "Some basic problems of the mathematical theory of elasticity"
      Noordhoff Int. Publ. Leyden, 1953.

70   Nelissen, L.J.M.
      "Biaxial testing of normal concrete"
      HERON, Vol.18, 1972, No.1.

71   Nozaki, H., Shindo, Y. and Atsumi, A.
      "Impact response of a cylinder composite with a penny-shaped crack"
      Int. J. Solids Structures, Vol.22, No.10, 1986, pp.1137-1147.

72   Oh, B.H.
      "Fracture behavior of concrete under high rates of loading"
      Int. J. Engineering Fracture Mechanics, Vol.35, No.1/2/3, 1990, pp.327-332.

73   Paul, B.
      "Macroscopic criteria for plastic flow and brittle fracture"
      In: Fracture, Vol.I. ed.H. Liebowitz
      Academic Press, 1968.

74   Perlman, A.B. and Sih, G.C.
      "Elastostatic problems of curvilinear cracks in bonded dissimilar materials"
      Int. J. of Science, Vol.5, 1967, pp.845-867.

75   Peterson, P.E.
      "Crack growth and development of fracture zones in plain concrete and similar materials"
      Report TVBM-1106, Lund Institute of Technology, Sweden, 1981.

76   Reinhardt, H.W.
      "Concrete under impact loading, Tensile strength and bond"
      Heron, Vol. 27, No.3 1982.

152

77   Reinhardt, H.W.
Fracture mechanics of an elastic softening material like concrete"
HERON, Vol 29, No.2, 1984.

78   Reinhardt, H.W., Cornelissen, H.A.W., Hordijk, D.A.
"Tensile tests and failure analysis of concrete"
J. Structural Engineering, ASCE, Vol.112(11), 1986, pp.2462-2477.

79   Reinhardt, H.W., Körmeling, H.A. and Zielinski, A.J.
"The Split Hopkinson Bar, a versatile tool for the impact testing of concrete"
Materiaux et Constructions, Vol.19, No 109, 1986, pp.55-63.

80   Reinhardt, H.W., Rossi, P. and Van Mier, J.G.M.
"Joint investigation of concrete at high rates of loading."
Materials and Structures/Matériaux et Constructions, Vol. 23, 1990, pp.213-216.

81   Robert, D.K. and Wells, A.A.
"The velocity of brittle fracture"
Engineering 172, 1954, pp.820-821.

82   Romstadt, K.M., Taylor, M.A. and Herrmann, L.R.
"Numerical biaxial characterization for concrete".
J. of Engineering Mechanics Division, Vol.100, No.EM5, October 1975, pp.935-948.

83   Rots, J.
"Recent developments, complicated fracture models in numerical calculations"
Doctoral thesis, Delft University, 1989.

84   Scavuzzo, R., et al.,
"Stress strain curves for concrete under multiaxial load histories"
University of Colorado, Boulder, 1983.

85   Shah, S.P., McGarry, F.J.
"Griffith fracture criterion and concrete"
J. of Engineering Mechanics Division, Proc. ASCE, December 1971, pp.1663-1676.

86   Shah, S.P., John, R.
"Strain rate effects on Mode I crack propagation in concrete"
Fracture toughness and fracture energy of concrete, ed. Wittmann, F.H., Developments in Civil Engineering 18, Elsevier, 1986.

87   Shah, S.P., John, R.
      "Strain rate effects on Mode I crack propagation in concrete"
      Fracture toughness and fracture energy of concrete, editor: Wittmann, F.H.,
      Developments in Civil Engineering 18, Elsevier, 1986.

88   Shen, W., et al.
      "Generalized elastic damage theory and its application to composite plate"
      Int. J. of Engineering Fracture Mechanics, Vol.28, No.4, 1987, pp.403-412.

89   Sih, G.C.
      "Mechanics of Fracture I, Solutions of crack problems. Introductory
      Chapter"
      Noordhoff Int. Publ. Leyden, 1973.

90   Sih, G.C.
      "Mechanics of Fracture 4, Elasto dynamic crack problems"
      Noordhoff Int. Publ.Leyden, 1977.

91   Sih, G.C.
      "Mechanics of material damage in concrete"
      In: Fracture mechanics of concrete, eds. A.Carpinteri and A.R. Ingraffea.
      Martinus Nijhoff Publishers, 1984.

92   Sluys, L.J.
      "Numerical analysis of impact tensile tests on concrete"
      Report No. 25.2.89.5.15, Delft University of Technology, 1989.

93   Sluys, L.J.
      "Strain softening under static and dynamic loading"
      Report No. 25.2.89.5.09, Delft University of Technology, July 1989.

94   Sluys, L.J. and De Borst, R
      "Rate dependent modelling of concrete fracture"
      HERON, Vol.36, No.2, 1991.

95   Sluys, L.J.
      "Wave propagation, localisation and dispersion in softening solids"
      Doctoral thesis, Delft University of Technology, 1992.

96   Sluys, L.J. and De Borst, R.
      "Solution methods for localisation in fracture dynamics"
      In: Fracture processes in concrete, rock and ceramics.
      eds. J.G.M. van Mier et al.
      RILEM Proceedings, Noordwijk, 1991.

154

97   Sneddon, I.N.
        In: "Mechanics of Fracture I, Methods of analysis and solutions of crack
        problems", ed.G.C.Sih.
        Noordhoff Int. Publ. Leyden, 1973.

98   Stroeven, P.
        "Some aspects of the micromechanics of concrete"
        Doctoral thesis, Delft University of Technology, 1973.

99   Suaris, W. and Shah, S.P.
        "Mechanical properties of materials subjected to impact"
        Proc. Concrete structures under impact and impulsive loading, Introductory
        report, Berlin, June, 1982.

100   Suaris, W. and Shah, S.P.
        "Constitutive model for dynamic loading of concrete"
        J. of Structural Engineering, Vol.111, No.3, March 1985, pp.563-576.

101   Swamy, R.N.
        "Linear elastic fracture mechanics parameters of concrete"
        In: Fracture Mechanics of Concrete, ed. F.H.Wittmann, Elsevier Science
        Publishers B.V. Amsterdam, 1983.

102   Takeda, I. et al.
        "Mechanical behaviour of concrete under higher rate of loading than in
        static tests"
        Proc. Mechanical Behaviour of Materials, Kyoto 1974, Vol.II, pp.479-486.

103   Tasuji, M., Slate, F.O. and Nilson, A.H.
        "Stress-strain response and fracture of concrete in biaxial loading"
        ACI Journal, July 1978, pp.306-312.

104   Taylor, M.A. and Broms, B.B.
        "Shear bond strength between coarse aggregate and cement paste or mortar"
        ACI Journal, Proceedings V. 61, No.8, 1964, pp.939-958.

105   Torrent, R.J., et al.
        "A model for work-hardening plasticity and failure of concrete under
        multiaxial stresses"
        J. Cement and Concrete Research. Vol.17, 1987, pp.939-950.

106   Tsai, Y.M.
        "Exact stress distribution, crack shape and energy for a running penny-
        shaped crack in an infinite elastic solid"
        Int. J. of Fracture Mechanics, Vol 9, No.2, 1973.

107   Verhagen, Th.L.A.
        "Survey of the possibilities of the interactive digital data processing program
        PMLSIGNAL" (in Dutch)
        PML report, PML 1989-IN25, September 1989.

108   Walraven, J.C.
        "Aggregate interlock: a theoretical and experimental analysis"
        Doctoral thesis, Delft University Press, 1980.

109   Wittmann, F.H. and Zaitsev, Y.
        "Verformung und Bruchvorgang poröser Baustoffe bei kurzzeitiger
        Belastung und Dauerlast"
        Deutscher Ausschuss für Stahlbeton, Heft 232, 1974.

110   Wittmann, F.H. and Zaitsev, J.
        "Verformung und Bruchforgang poroser Baustoffe bei kurzzeitiger Belastung
        und Dauerlast"
        Deutscher Ausschuss fur Stahlbeton, eft 232, 1974.

111   Wittmann, F.H.
        "Structure of concrete with respect to crack formation"
        In: Fracture Mechanics of Concrete, ed. F.H.Wittmann,
        Elsevier Science Publishers B.V. Amsterdam, 1983.

112   Weerheijm, J.
        "Fracture model for concrete under dynamic tensile loading"
        PML 1984-15, Rijswijk, 1984 (in Dutch).

113   Weerheijm, J. and Karthaus, W.
        "The tensile strength of concrete under dynamic loading"
        Proc. The interaction of non-nuclear munitions with structures. Panama
        City Beach, Florida, April 1985, pp.211-216.

114   Weerheijm, J.
        " Schematized description of the fracture process in concrete under tensile
        and compressive loading" (in Dutch)
        PML Report PML 1987-16, Rijswijk 1987.

115   Weerheijm, J. and Reinhardt, H.W.
        "Concrete in impact tensile tests"
        Proc. First International Conference on Structures under Shocks and
        Impact, Cambridge, Massachusetts, July, 1989.

116 Weerheijm, J.
"Dynamic properties of concrete 1. The experimental programme"
PML 1988-61, TNO-Prins Maurits Laboratory, Rijswijk, December 1988
(in Dutch).

117 Weerheijm, J.
"Dynamic properties of concrete 2. Biaxial loading device"
PML 1989-59, TNO-Prins Maurits Laboratory, Rijswijk, May 1989.

118 Weerheijm, J.
"Properties of concrete under dynamic loading 3: Fracture model for brittle
materials"
PML report PML1990-65, Rijswijk, October 1990.

119 Weerheijm, J. and Postma, S.
"The scheme of the fictitious fracture plane"
PML-report PML1992-IN26, February, 1992

120 Weerheijm, J.
Properties of concrete under dynamic loading 4.
The uniaxial impact tests.
PML 1991-91, Rijswijk, The Netherlands, 1991.

120[b] Yon, J.H., Hawkins, N.M. and Kobayashi, A.S.
"Fracture process zone in dynamically loaded crack-line wedge-loaded,
double cantilever beam concrete specimen".
ACI Journal, Vol.88, No.5, September 1991, pp.470-479.

121 Zaitsev, Y.
"Crack propagation in a composite material"
In: Fracture Mechanics of Concrete, ed. F.H.Wittmann,
Elsevier Science Publishers B.V. Amsterdam, 1983.

122 Zaitsev, Y.
"Simulation of behaviour of light-weight concrete under load and its trial"
In: Fracture toughness and fracture energy of concrete, ed. F.H.Wittmann,
Elsevier Science Publishers B.V. Amsterdam, 1986.

123 Ziegeldorf, S.
"Fracture mechanics parameters of hardened cement paste, aggregates and
interfaces"
Institut für Baustofftechnologie, Universitaet Karlsruhe (TH), Karlsruhe,
West Germany, 1980.

124   Zielinski, A.J.
        "Fracture of concrete and mortar under uniaxial impact tensile loading"
        Doctoral thesis, Delft University of Technology, 1982.

125   Zielinski, A.J.
        "Concrete under biaxial loading: Static compression-impact tension"
        Stevin Report 5-85-1, Delft University of Technology, 1985.

126   Zielinski, A.J.
        "Concrete under biaxial compressive-impact tensile loading"
        In: Fracture toughness and fracture energy of concrete, ed. F.H.Wittmann,
        Elsevier Science Publishers B.V. Amsterdam, 1986.

127   Zukas, J.A. et al.
        "Impact Dynamics"
        John Wiley & Sons, New York, 1962.

Formulae to derive the geometry of the fictitious fracture plane   ANNEX

In this annex, the equations to determine the geometry of the fictitious fracture planes are presented in sequence of calculation.

<u>Tensile loading:</u> Input parameters are: ξ_c, D_{max}, p_a, $f_{t,b}$, $f_{t,a+m}$, E, n

$$D \quad = \quad \left(1 - \frac{P_c}{2}\right)^2 \cdot D_{max} \qquad\qquad (A3.1)$$

$$d \quad = \quad \left(\sqrt[3]{\frac{\pi}{3\sqrt{2}}} \cdot \frac{1}{\sqrt[3]{P_a \cdot P_c}} - 1\right)\left(1 - \frac{P_c}{2}\right)^2 \cdot D_{max} \qquad\qquad (A3.2)$$

$$\frac{A_{fr}}{A} \quad = \quad (1 - p_a) + \xi_c \cdot p_a + 2\, p_a \ln \frac{2}{1 + \xi_c} \qquad\qquad (A3.3)$$

$$b \quad = \quad a_b + \frac{1}{2}\sqrt{\frac{A_{fr}}{A}} \cdot (D + d) \qquad\qquad (A3.4)$$

$$a_b \quad = \quad \frac{\pi}{4} \cdot \frac{2\gamma_b \cdot E_m}{1 - v_m^2} \cdot \frac{1}{f_{t,b}^2} \cdot \frac{1}{f^2\left(\frac{a_b}{b}\right)} \qquad\qquad (A3.5)$$

$$A \quad = \quad \pi\,(b^2 - a_b^2) \cdot \frac{A}{A_{fr}} \qquad\qquad (A3.6)$$

$$a_{m+a} \quad = \quad \sqrt{\frac{2 p_a}{\pi}\, \frac{A}{} \cdot \ln \frac{2}{1 + \xi_c} + a\,\frac{2}{b}} \qquad\qquad (A3.7)$$

$$\gamma_{m+a} \quad = \quad \frac{4\, a_{m+a}\,(1 - v^2)}{2\,\pi E} \cdot f_{t,m+a}^2 \cdot f^2\left(\frac{a_{m+a}}{b}\right) \qquad\qquad (A3.8)$$

$$\gamma_m \quad = \quad \frac{-\gamma_a \cdot \xi_c \cdot p_a + \gamma_{m+a}\,[(1 - p_a) + \xi_c \cdot p_a]}{1 - p_a} \qquad\qquad (A3.9)$$

Two options are proposed to solve the equations and determine the geometry of the plane under tensile loading.

Option 1:
Assume the parameters ξ_c, γ_a and γ_b are known
The first five equations result in an implicit equation for the initial crack size, a_b.
This implicit equation was solved numerically.
The other parameters can be calculated just by substitution.

Option 2:
Assume the parameters γ_a, γ_m and γ_b are known.
In this case, a second iteration is necessary to determine the value ξ_c.

Both options were implemented in a numerical program.

Compressive loading:

The geometry of the fictitious fracture plane under compressive loading can be determined uniquely then the tensile scheme is known.
Additional input parameters are: $f_{c,b}$, $f_{c,m}$

The sequence of calculation is as follows:

$$\xi'_c = \frac{1}{2}\sqrt{3} \tag{A3.10}$$

$$\frac{A'_{fr}}{A} = (1.367 - 0.044\, p_a) \tag{A3.11}$$

$$b' = a_b + \frac{1}{2}\sqrt{\frac{A'_{fr}}{A}}\,(D+d) \tag{A3.12}$$

$$\delta_b = \frac{f_{t.b}}{f_{c.b}} \cdot \left\{ \frac{f^2\left(\frac{a_b}{b}\right)}{f^2\left(\frac{a_b}{b'}\right)} \right\} \tag{A3.13}$$

$$a'_m = \sqrt{\frac{0.139\, p_a \cdot A}{\pi} + a_b} \tag{A3.14}$$

$$\delta_m = \sqrt{\frac{\pi}{4} \cdot \frac{2\,\gamma_m}{1 - v_m^2} \cdot \frac{E_m}{f^2\left(\frac{a'_m}{b'}\right)} \cdot \frac{1}{a'_m}} \tag{A3.15}$$

Concluding remark:

The fictitious fracture planes under tension and compression can be determined when the following parameters are known:

E_m; ν_m; $f_{t,b}$; $f_{t,m} + a$; $f_{c,b}$; $f_{c,m}$

γ_a; γ_b; p_a; p_c; D_{max} and γ_m or ξ_c

Because the parameters γ_a, γ_b and γ_m or ξ_c are not well known they should be estimated with sense.

In Chapter 3, the procedure proposed was applied to the concrete qualities tested in the experimental programme.

CURRICULUM VITAE

Naam	Jakob Weerheijm
1 februari 1955	Geboren te Vlaardingen
juni 1974	Eindexamen Atheneum B van het Groen van Prinsterer Lyceum te Vlaardingen
juni 1981	Diploma Civiel Ingenieur van de Technische Universiteit Delft. Afstudeeronderwerp betrof het tijdsafhankelijk vervormingsgedrag van gedeeltelijk voorgespannen beton.
mei 1981	Werkzaam bij de researchgroep Explosieveiligheid van het Prins Maurits Laboratorium van TNO. Werkgebied werd aanvankelijk gevormd door de bodemdynamica en de respons van constructies onder explosie- en impact-belasting. Na een aantal jaren verschoof het accent richting het onderwerp van het beschreven promotie-onderzoek: de eigenschappen van beton onder dynamische belasting.
1986 - 1992	Periode waarin het onderzoek is uitgevoerd.
mei 1987	Hoofd van de Sectie Uitwerking Accidentele Explosies, die onderdeel uitmaakte van de Researchgroep Explosieveilgheid.
juni 1992	Hoofd van de Researchgroep Explosiepreventie en Bescherming.